TUNING AND ALIGNMENT OF ATF2

A thesis submitted to The University of Manchester for the degree of
Doctor of Philosophy
in the Faculty of Engineering and Physical Sciences

2011

ANTHONY SCARFE

School of Physics and Astronomy

Contents

Word count: 39157

The University of Manchester

ABSTRACT OF THESIS submitted by Anthony Scarfe
for the Degree of Doctor of Philosophy and entitled
Tuning and alignment of ATF2. 2011

The Accelerator Test Facility (ATF2) at KEK, Japan, aims to experimentally verify the local chromaticity correction scheme designed to achieve a vertical beam size of 37 nm. The facility is a scaled down version of the final focus design proposed for the future linear colliders. In order to achieve this goal, high precision tuning methods and orbit correction techniques are being developed. Experimental studies were planned and undertaken in order to discover and compensate for sources of emittance growth in the extraction region of ATF2. Global Single Value Decomposition (SVD)-based orbit correction algorithms have been developed and optimised for the ATF2 extraction line and final focus. A novel method known as the 'rotation matrix' method has been developed for the spot-size tuning of ATF2 in order to achieve a nanometre-scale beamsize. The tuning algorithms used at ATF2 will provide an important input for future linear colliders (including the International Linear Collider (ILC) and Compact Linear Collider (CLIC)).

Declaration

I declare that no portion of the work referred to in the thesis has been submitted in support of an application for another degree or qualification of this or any other university or other institute of learning.

Copyright Statement

I Started Out with Nothin and I Still Got Most of It Left.

Seasick Steve, 2008

Dedication

To my parents. Thank you for everything.

Acknowledgements

I would like to thank the very large number of people that helped me achieve this goal.

This thesis was typeset with LaTeX.

The Author

Some of Anthony Scarfe's earliest memories are of his enjoyment of learning about science and mathematics. Anthony has always had an interest in how things work and how to get things to work. At the beginning of his journey towards this thesis, Anthony was simply chasing mental stimulation, however the amount of mental stimulation he would recieve has surpassed his expectations. Anthony is very grateful for the knowledge he has gained so far.

Supporting Publications

Present status and first results of the final focus beam line at the KEK Accelerator Test Facility

P. Bambade & A. Scarfe et al., Phys Rev Special Topics 13(4), 2010.

Experimental studies and analysis of the vertical emittance growth in the ATF extraction line in 2007-2008

M. Alabau-Pons & A. Scarfe et al., Cockcroft-09-07, 2009.

Orbit Reconstruction, Correction, Stabilization and Monitoring in the ATF2 Extraction Line

Y. Renier & A. Scarfe et al., Cockcroft-09-04, 2009.

ATF2 Spot Size Tuning Using the Rotation Matrix Method

A. Scarfe et al., Cockcroft-09-03, 2009.

Orbit Correction Optimisations for the ATF2 Final Focus

A. Scarfe, Cockcroft-08-124, 2008.

ATF2 Commissioning

A. Seryi & A. Scarfe et al., Cockcroft-09-02, 2009.

Plans and Progress towards Tuning the ATF2 Final Focus System to Obtain a 35nm IP Waist

G. White & A. Scarfe et al., Cockcroft-09-05, 2009.

ATF2 Final Focus Orbit Correction and Tuning Optimisation

A. Scarfe et al., Proceedings of EPAC08, 2008.

4D Emittance Measurements Using Multiple Wire and Waist Scan Methods in the ATF Extraction Line

C. Rimbault & A. Scarfe et al., Proceedings of EPAC08, 2008.

ATF2 ULTRA-LOW IP BETAS PROPOSAL

R. Tom*á*s & A. Scarfe et al., Proceedings of PAC09, 2009.

The BDSLD task: Summary and deliverables

D. Angal-Kalinin & A. Scarfe et al., EUROTeV-Report-2008-078, 2008.

Exploring ultra-low β* values in ATF2 R&D Programme proposal

D. Angal-Kalinin & A. Scarfe et al., CARE/ELAN Document-2008-002, 2008.

STUDY OF ABNORMAL VERTICAL EMITTANCE GROWTH IN ATF EXTRACTION LINE

M. Alabau-Pons & A. Scarfe et al., Proceedings of EPAC08, 2008.

ATF2 SUMMARY AND STATUS

G. White & A. Scarfe et al., Beam Dynamics Newsletter No. 54, 2011.

1

Introduction

1.1 Chapter Overview

This chapter introduces the basics of accelerator design and the physics behind them. A history of accelerators is presented along with introductions to the Accelerator Test Facility (AFT/ATF2) and the planned International Linear Collider (ILC), which feature prominently in the rest of this report.

1.2 An Introduction to Accelerators

1.2.1 Basic Accelerator Design

A particle accelerator is a device which uses electromagnetic fields to alter the momentum of a charged particle. One of the most basic particle accelerator designs is a cathode ray tube (CRT) and is the main component of early television and monitor designs. All accelerator designs must have a source of charged particles. In the case of an electron accelerator this can be achieved through the use of an electron gun. Once a 'bunch' of charged particles has been formed they are passed through a series of carefully controlled electromagnetic fields. The charged particles gain energy due to the effect of the Lorentz force generated between the source of the electromagnetic

field and the charged particles. This results in an increase of the momentum of each charged particle. This is also how the trajectory of the bunches of charged particles is controlled. By placing a carefully selected sequence of carefully controlled electromagnets and radio frequency (RF) cavities, it is possible to produce a machine that can theoretically direct a stream of charged particles along any preconceived path to any point in space with any desired final momentum.

There are two major factors that control the design of high energy particle accelerators. The first choice is the type of particles used, which can be either hadrons or leptons. Hadrons are composite particles, which means that the momentum of the hadron is divided between its constituent particles, as a result the collision of two hadrons is an unknown number of collisions between unknown pairs of elementary particles which each have an unknown momentum. A lepton is an elementary particle and will transfer all of its momentum into the collision, as a result a lepton collider will allow for more accurate knowledge of the conditions during the particle collisions. Hence a lepton collider is required for more accurate particle physics knowledge to be gathered.

The second choice is the design of the beam path, which can be either circular or linear. A circular machine allows the particles to undergo multiple passes along the length of the machine. It must also be noted that a large number of particles may not collide, and so may be reused in a circular machine. The drawback to a circular machine is that a charged particle will emit electromagnetic radiation, hence lose momentum, when its path is altered by an electromagnetic field. This effect is inversely proportional to the fourth power of the rest mass of the particle, which means that a 0.511 MeV rest mass electron lepton will lose its momentum considerably faster than a 938 MeV rest mass proton hadron when their paths are curved. To push the centre of mass energy boundaries of electron-based colliders a linear design must be implemented.

1.2.2 Current and Future Accelerators

The three main high energy accelerator projects as of the start of 2010 are the Large Hadron Collider (LHC), the International Linear Collider (ILC) and the Compact Linear Collider (CLIC) (See Table 1.1). The expected commissioning dates of the accelerators as of 2006 can be seen on the adapted Livingstone plot (Fig. 1.1) that was presented at ICAP'06 [1]. The expected commissioning dates for ILC and CLIC presented in the plot have become unrealistic due to delays in the commissioning of LHC and delays in the research projects needed for ILC and CLIC.

Table 1.1: The intended parameters of the LHC, ILC and CLIC when operating at peak energy levels.

Machine Parameter	**LHC**	**ILC**	**CLIC**
Particle Type	Proton/Proton	Electron/Positron	Electron/Positron
Machine Type	Synchrotron	Linac	Linac
Beam Energy (TeV)	7	0.25	1.5
Bunches per Beam	2808	2625	220
Particles per Bunch	1.15×10^{11}	2×10^{10}	2.56×10^{9}
Horizontal IP Beam Size (nm)	16×10^{3}	640	60
Vertical IP Beam Size (nm)	16×10^{3}	5.7	0.7
Repetition Rate (kHz)	11	5×10^{-3}	0.05
Luminosity ($1/(cm^2 s)$)	10^{34}	2×10^{34}	3×10^{34}
Bunch Separation (ns)	25	6.2	0.5
Bunch Length (μs)	1×10^{-3}	300	0.156
Normalised Horizontal Emittance (μm.rad)	2.5	10	660
Normalised Vertical Emittance (μm.rad)	3.75	0.04	20

LHC is a circular hadron collider at CERN and has a maximum centre of mass energy of 14 TeV. The experiments performed at LHC are expected to require several years worth of data in order to produce adequate particle physics results. ILC and CLIC are both linear electron-positron colliders that are yet to have finalised accelerator designs, however both will require luminosities that have not been achieved before in similarly high energy machines. As of 2009 ILC has a completed reference design

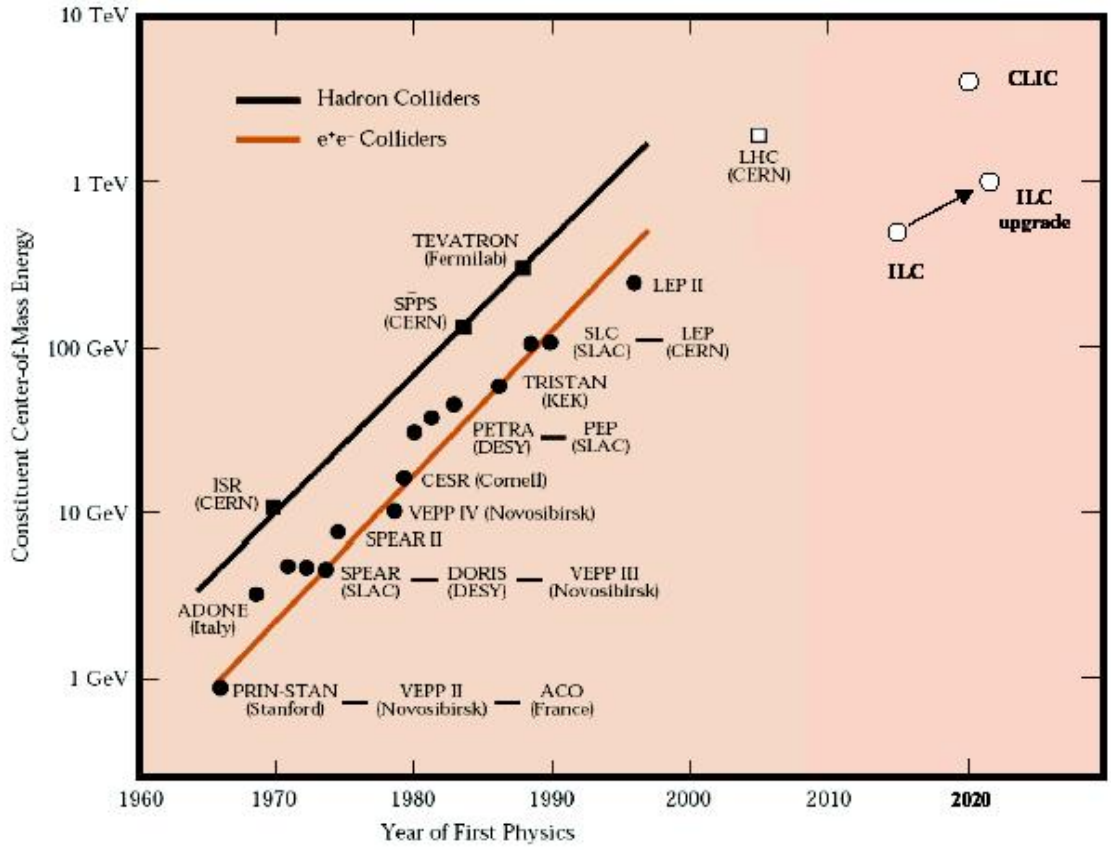

Figure 1.1: An adaptation of the Livingstone plot which shows the centre of mass energy of the most important hadron and electron-positron colliders and the dates at which the colliders were commissioned. This plot dates from 2006 and the expected commissioning dates of LHC, ILC and CLIC are not realistic.

report (RDR) [2] and is expected to have a technical design report (TDR) by 2012. It will start at a centre of mass energy range of 250-500 GeV and will be upgraded to 1 TeV. At the time of writing CLIC is expected to have a concept design report (CDR) by the end of 2011 and a TDR by 2016. It will start at a centre of mass energy of 500 GeV and be upgraded to 3 TeV. Both linear colliders are expected to have a build time of roughly 7 years and no formal decision on whether either linear collider will be built has been made. The results from LHC are required in order to give an indication of what the centre of mass energy of the next linear collider must be in order to improve upon the current level of particle physics understanding. The current major aims for these colliders are the verification and understanding of the Higgs particle.

One of the most important parameters of a collider is the luminosity of the beam. This is a measure of how likely it is that a collision will happen, hence this should be made as high as possible. The luminosity is a multiplication of the density of particles in the beam and the rate at which the bunches of the beam pass the interation point (repartition rate). The repartition rate is defined as $1/t$, where t is the time between bunches. The beam density is the number of particles in the bunch (N) divided by the beam size at the IP (σ). The beam size is related to the emittance of the beam at the IP (ε) and the beta-function of the beam at the IP (β) in such a way as $\sigma = \sqrt{\varepsilon\beta}$. If the luminosity is defined as L then

$$L = N/t\sqrt{\varepsilon\beta} \tag{1.1}$$

N and t are properties of the machine and are limited by hardware constraints. This means that an ultra-low emittance at the IP will lead to a very high luminosity and will maximise the efficiency of the machine.

ILC

The main aim of the work presented in this report is to develop methods that will aid in obtaining and maintaining the ultra-low emittance beams required by ILC. The emittance of the beam is related to the width of the beam, which is inversely proportional to the luminosity, which is an indicator of the probability of a particle interaction. As a result a lower emittance beam will result in a larger number of particle interactions and will increase the chances of detecting uncommon and previously unseen events.

The design of ILC [2] (Fig. 1.2) relies upon a long straight linear accelerator section (linac) and beam delivery system (BDS). If emittance growth was to occur in these

long straight sections (the linac and BDS) the effects would propagate along the beam-line unless the emittance growth effects were corrected. As a result the design of the linac and especially the BDS require a number of emittance reduction and preservation elements and strategies.

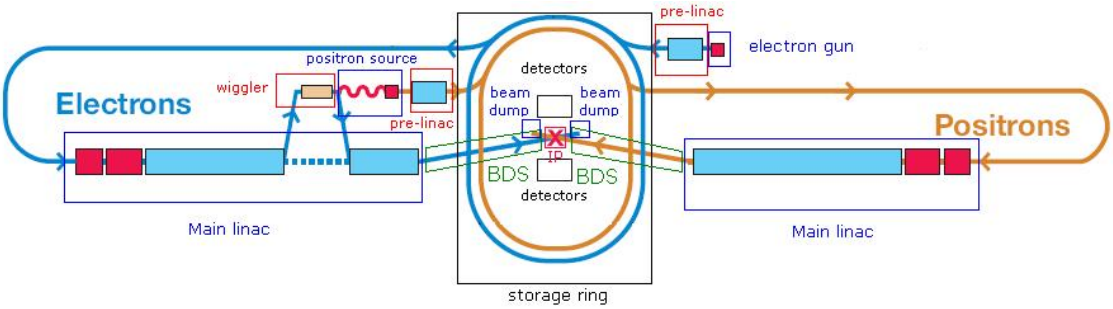

Figure 1.2: The current design of ILC.

The electrons are extracted at relatively low energies of roughly 140 keV from the electron source, which is a photocathode DC gun design. The electrons are then bunched together and their energy is collimated so as to form near uniform electron bunches at 76 MeV. The beam is then passed through a pre-accelerator, which accelerates the beam up to 5 GeV. The challenge to be overcome in the development of the electron source is the ability to obtain a 1 ms long bunch train. This will require a laser system like no other currently in use in an accelerator.

The electrons are then passed into a 6.7 km long radiation damping ring. The positron beam will also have a damping ring that follows this design. Each damping ring must reduce the horizontal and vertical emittance of the beam from the initial value to the value required for the successful achievement of the interaction point (IP) luminosity goal. This is a decrease of 5 orders of magnitude in the vertical emittance for the positron beam and the damping must be completed in the 200 ms gap between machine pulses. The damping ring must also inject and extract the bunches without disrupting any other bunches and reduce the levels of incoming beam jitter so as to

provide a highly stable beam for use downstream. The last task for the damping ring to complete is to provide a delay in the flow of bunches from the source to downstream areas so that feed-forward systems can be used to correct for pulse-to-pulse variations in the beam parameters. There are three major challenges to be overcome in the development of the damping rings. The first challenge is to control the electron cloud effect (the buildup of electrons inside the machine) in the positron damping ring so as to avoid beam instability, tune spread and emittance growth. This problem is well understood and can be controlled by the proper surface treatment of the vacuum chamber to suppress secondary emission of electrons and the use of solenoids and clearing electrodes to suppress the buildup of the cloud. The second challenge is the control of the fast ion instability inside the electron damping ring. This effect can be controlled by limiting the pressure inside the electron damping ring to 1 nTorr and by having short gaps in the ring fill pattern. The third challenge is the development of a very fast rise and fall time kicker for single bunch injection and extraction. The shortest gap between bunches is about 3 ns which means that the combined rise and fall time of the kicker can be no more than twice this amount.

After the electron beam is extracted from the damping ring it is passed along the 15 km long 'ring to main linac' transport line. The positron beam also has a 'ring to main linac'. The ring to main linac has been designed to perform several key functions. The 5 GeV beam must be transported from the ring to the start of the main linac including a 180° turn. The halo of stray particles around the beam must be removed through the use of a collimation system. The bunch length must be compressed by a factor of 30-45 using a 2-stage bunch compressor to provide the short bunches needed at the IP. The bunch compressor will also increase the energy of the beam from 5 GeV to 13-15 GeV in order to limit the fractional energy spread associated with bunch compression. The main challenges in the ring to main linac are to limit the levels of emittance, dispersion and coupling growth due to static misalignments and the suppression of phase and amplitude jitter in the bunch compressor RF which can lead to timing errors at the

IP and a loss in luminosity. The emittance, dispersion and coupling growth effects have been shown to be adequately correctable in simulations while the bunch compressor RF issues can be limited through the use of feedback loops.

The electron beam is then passed into the main linac which will accelerate the beam to 250 GeV. The electron main linac also includes an undulator section which is used as the positron source, which the positron variant of the main linac does not have. The electron and positron main linacs have an average accelerating gradient of 31.5 MV/m and a combined length of 23 km. The accelerating units are each composed of 3 superconductive RF cryomodules containing 26 nine-cell cavities. The middle cryomodule has a superconducting quadrupole magnet at the centre along with a cavity BPM and superconducting horizontal and vertical corrector magnets. The cryomodules will operate at a temperature of 2 K and will each be 12.652 m long. The quadrupoles will maintain an average beta function of about 80 m in their FODO lattice structure. The positron linac has 278 RF units while the electron linac has 282 RF units. A radio-frequency (RF) unit is a cavity in which the beam passes perpendicular to an electric frquency souce and hencce recieves an increase in energy. The main linacs must accelerate the beams without causing emittance growth, which requires careful control of the beam orbit and of the higher order terms in the accelerating cavities. The beam energy spread must also be kept to within about 0.1% at the IP and significant levels of beam jitter must be prevented. The main challenges faced by the main linac are the achievement of the 31.5 MV/m accelerating gradient, which is beyond those typically achievable today, the control of emittance (and subsequent dispersion and coupling) growth due to static misalignments, which can be fixed with the use of beam based alignment and higher order mode damping, and the final challenge is the control of the beam energy spread, which is controlled by the low-level RF system monitors in the cavities which are used to flatten the energy gain along the bunch train and maintain the beam-to-RF phase constant.

Finally the electron beam is passed in to the beam delivery system (BDS) which transports the beam from the main linac to the IP while preserving the emittance of the beam and also altering the beam parameters to match the parameters desired at the IP. The positron beam has an identical BDS and both beams cross each other's path once at an angle of 14 mrad. The use of a 14 mrad crossing angle requires that a crab cavity be used to rotate the beam so that an effectively 'head on' collision can be achieved thereby producing the most efficient collisions. Each BDS can be split into 4 parts. The initial section is tasked with the removal of any beam halos and mis-steered beams that are still present after the main linac, the measurement of any major beam parameters and the alteration of the beam parameters to fit those required at the IP. The second section is called the final focus and is tasked with preparing the beam for collision. The third section is the interaction region which is where the beams are brought into collision at the IP and where the detectors are situated. The final section is the extraction region which removes the remnants of the beam from the interaction region and transports it to the beam dump. There are 5 major challenges for the BDS. The motion of the magnets must have a tolerance of tens of nanometers so fast beam-based feedback systems are mandatory. Uncorrelated relative phase jitter between the crab cavities must be limited to tens of femtoseconds. Emittance growth must be controlled using beam-based alignment and tuning techniques. Background levels at the IP must be controlled through the use of careful tuning and optimisation of the collimation systems. The disrupted beams must be cleanly extracted and sent to the beam dumps.

The positron source begins inside the electron main linac. Once the electron beam has reached 150 GeV it is diverted along an offset beamline, which contains a 150 m long helical undulator, before it is returned to the main linac. As the electron beam passes through the undulator it produces about 10 MeV photons which produces sets of electron-positron pairs when they strike a titanium alloy target. The resultant particles are then captured and accelerated so as to separate the positrons from the electrons and any remaining photons. The resultant positron beam is at 125 MeV and must be

accelerated up to the 5 GeV required on injection to the damping ring. There are three major challenges to be overcome in the construction of the positron source. The undulator requires specifications that push the limitations of current undulator design. The titanium alloy target must be able to withstand the damage caused by ongoing exposure to the high energy photon beam needed to produce the electron-positron pairs. The RF system that is tasked with the capture of the positrons also requires high specifications.

The work presented in this report attempts to provide adequate techniques for the beam-based alignment and other general tuning and alignment techniques for use in the ring to main linac and BDS of ILC.

ATF

The Accelerator Test Facility (ATF) [3] at KEK, Japan was designed as a damping ring for normal conducting linear colliders and now is used as a small low energy test version of the damping ring for ILC and CLIC, including the injection region and extraction line. The ATF2 upgrade modified the extraction line section of ATF and included a small test version of the ILC final focus section (Fig. 1.3).

ATF uses an RF gun, pre-injector and s-band linac to achieve a beam energy of about 1.5 GeV. The beam is then injected into the 138 m circumference damping ring and is damped down to the desired emittance in 100-450 ms. The beam is extracted using a fast pulse kicker magnet that pulses at 120 ns. The ring also contains 96 beam position monitors (BPMs), which in this case are button BPMs, and a couple of RF cavities that replace the energy lost due to synchrotron radiation. The beam is then sent along the extraction line which contains a number of magnet elements, a number of devices designed to accurately measure the parameters of the beam and a number of horizontal and vertical steering magnets. This is the end of the ATF section and a slightly altered extraction line leads into the ATF2 final focus section. This is where

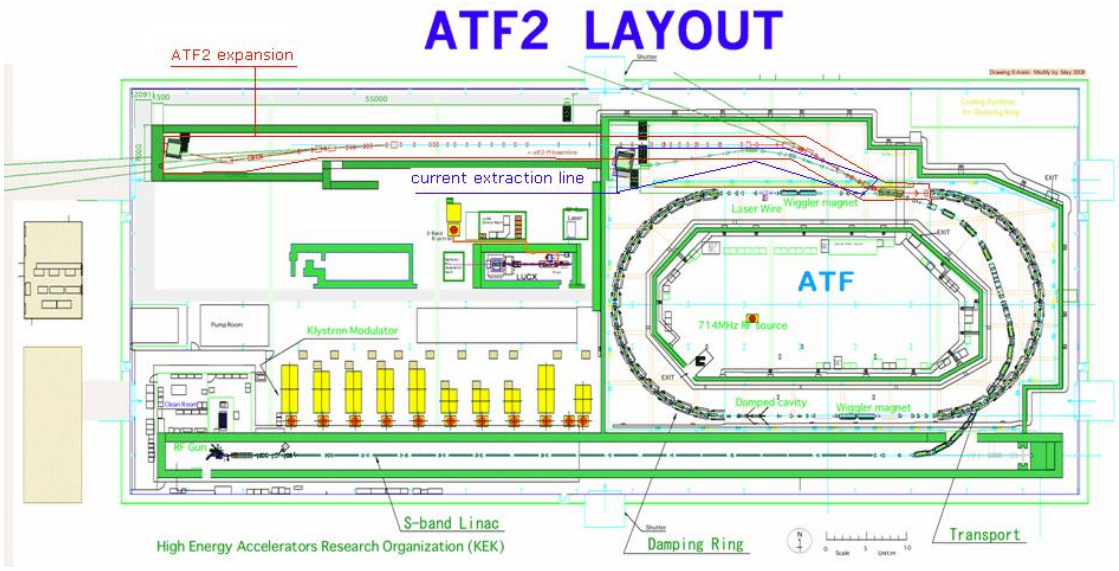

Figure 1.3: The layout of ATF2 with the previous ATF extraction line included. This diagram was made prior to the ATF2 upgrade.

the vertical beamsize at the IP is reduced down to the 37 nm goal.

Each bunch contains 10^{10} electrons for single bunch operation mode and 0.7×10^{10} electrons in multi-bunch operation mode, which has 20 bunches per bunch train. The repetition rate of the machine is 0.7-6.4 Hz. The emittance after extraction from the damping ring is 10^{-9} rad·m horizontally and 10^{-11} rad·m vertically.

ATF and ATF2 have been used to test equipment and techniques that are vital for obtaining and maintaining the ultra-low emittance beams needed for the success of ILC. Both ATF and ATF2 have been the central focus of the work presented in later sections of this report, however the techniques developed for use on ATF and ATF2 should be applicable on ILC.

ATF2

ATF2 is a modified and updated version of ATF (Fig. 1.4 and Fig. 1.5, more details can be found at [21]).

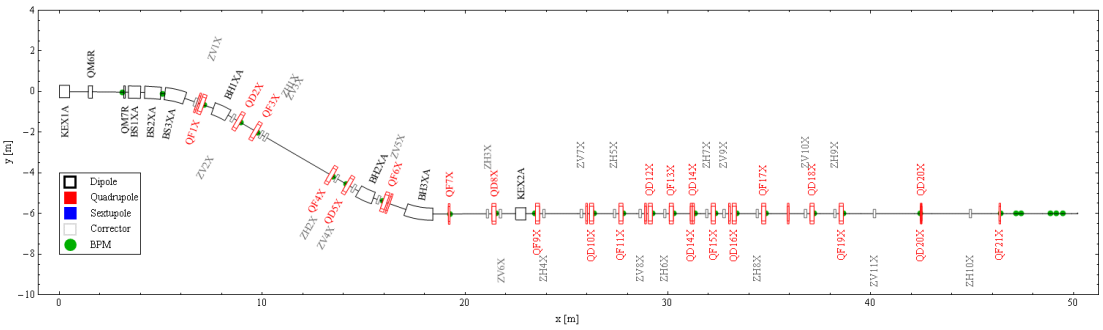

Figure 1.4: ATF2 v3.8 extraction line, generated using the DIMADInput Mathematica package, please note that the BPM and magnet numbers are in decending order and that the beam direction is from left to right.

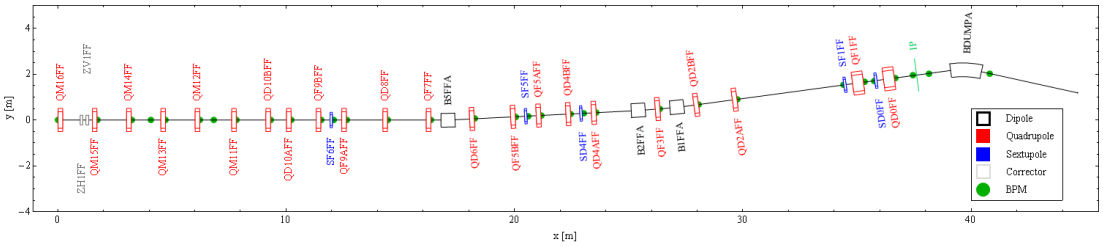

Figure 1.5: ATF2 v3.8 final focus, generated using the DIMADInput Mathematica package, please note that the BPM and magnet numbers are in decending order and that the beam direction is from left to right.

The expected ATF2 errors (Table. 1.2) were used for the simulations in later chapters.

1.3 Beam Dynamics

The physics governing the behaviour of a particle in an accelerator is referred to as beam dynamics and is based on classical electromagnetism and relativistic Newtonian

Table 1.2: Expected ATF2 Errors.

Error Type	Value
Magnet Alignment (μm)	200
Roll Tolerances (μrad)	300
Initial BPM-Magnet Alignment (μm)	30
Magnetic Field Tolerances (Systematic) (dB/B)	1×10^{-4}
Magnetic Field Tolerances (Random) (dB/B)	1×10^{-4}
Shintake monitor Resolution (nm)	2
Magnet Vibration (nm)	10
Pulse-Pulse Corrector Magnet Strength Errors	1×10^{-4}
BPM Resolution (nm)	100
Mover Resolution (x and y) (nm)	50
Power Supply Resolution (bits)	11

mechanics [4].

The particles in an accelerator are commonly accelerated to close to the speed of light, hence the energy of a particle in an accelerator must be written in the relativistically invariant form

$$E = \sqrt{m_0^2\, c^4 + p^2\, c^2} \tag{1.2}$$

where E is the energy of the particle, m_0 is the rest mass of the particle, p is the momentum of the particle and c is the speed of light in a vacuum. Traditionally if $\beta = v/c$, where v is the particle velocity, and $\gamma = (1-\beta^2)^{-1/2}$ the relativistic momentum of the particle can be written as

$$p = m\, v = \gamma\, m_0\, v \tag{1.3}$$

where m is the energy-dependent mass of the particle. Since the only free parameter in equation 1.2 is p and Newton's second law of motion only allows for the momentum to be changed by the action of a force $\mathbf{F}$ on the particle, the energy of the particle can only be changed by applying a force to the particle. To obtain the energies required at high energy accelerators, a sufficiently strong force must be exerted on the particle for

a significantly strong period of time. The only fundamental force capable of achieving this goal is the electromagnetic force. When a particle of velocity υ passes through a region containing a magnetic field $\mathbf{B}$ and an electric field $\mathbf{E}$ it experiences the effects of the Lorentz force

$$\mathbf{F} = e(\upsilon \times \mathbf{B} + \mathbf{E}) \tag{1.4}$$

where e is the elementary charge. As the particle moves from position $\mathbf{r_1}$ to $\mathbf{r_2}$ it undergoes an energy change of

$$\Delta E = \int_{r_1}^{r_2} \mathbf{F} \cdot d\mathbf{r} = e \int_{r_1}^{r_2} (\upsilon \times \mathbf{B} + \mathbf{E}) \cdot d\mathbf{r} \tag{1.5}$$

During the motion the path element $d\mathbf{r}$ is always parallel to the velocity vector υ, hence $\upsilon \times \mathbf{B}$ is perpendicular to $d\mathbf{r}$ and always equal to zero. This means that the magnetic fields do not change the energy of the particle. The increase in energy of the particle is achieved only through the use of electric fields and the gain in energy is given by

$$\Delta E = e \int_{r_1}^{r_2} \mathbf{E} \cdot d\mathbf{r} = eU \tag{1.6}$$

where U is the voltage crossed by the particle.

The outermost particle position at each point along the beamline is known as the beta function (β) at that point. There are separate horizontal and vertical beta functions. It is possible to use 'Hill's equation [4]' (equation 1.7) in this situation due to the fact that the equation of motion of the particle has periodic focusing properties.

$$x(s) = \sqrt{\varepsilon_x}\sqrt{\beta_x(s)}\cos\left(\psi_x(s) + \phi_x\right) \tag{1.7}$$

ε_x and ϕ_x are integration constants determined by the initial conditions while $\psi_x(s)$ is the 'phase advance' between s_0 and s_1. It is given by

$$\psi_x(s) = \int_{s_0}^{s_1} \frac{\mathrm{d}s}{\beta_x(s)} \tag{1.8}$$

ε_x is known as the emittance and is given by

$$\varepsilon_x = \gamma(s)x(s)^2 + 2\alpha(s)x(s)p_x(s) + \beta(s)p_x(s)^2 \tag{1.9}$$

Where p_x is the horizontal momentum of the particle. γ is one of the Twiss parameters of the beam and is given by $\gamma = \frac{1+\alpha^2}{\beta}$. α is also a Twiss parameter of the beam and is given by $\alpha = -\frac{1}{2}\frac{d\beta}{ds}$. The emittance remains constant while the energy is constant and is, to within a factor π, the area of the 'phase space ellipse' formed by plotting all possible combinations of the particle's transverse position and momentum (Fig. 1.6). For situations when multiple particles are being considered the ellipse is formed from the maximum values of the positions and momenta of the particles.

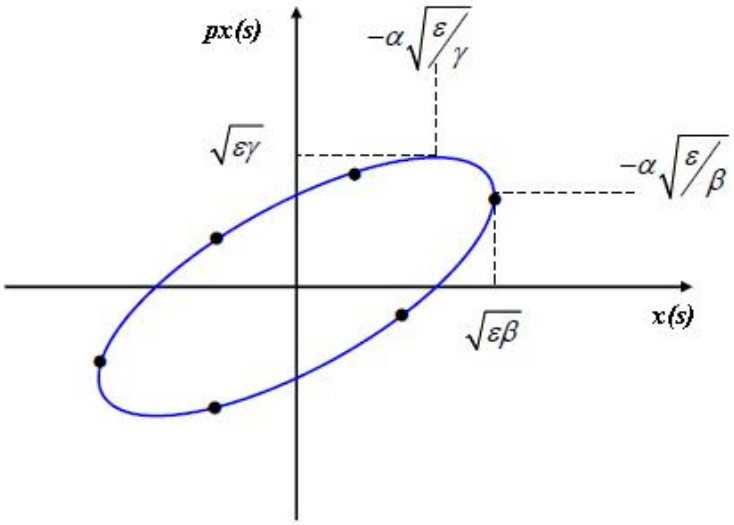

Figure 1.6: A diagram of the phase space ellipse of a particle.

The beta, alpha and gamma functions of the phase space ellipse are known as the 'Twiss parameters'. As the particle moves along its orbit, the shape and position of the phase space ellipse changes according to the beta function. This means that by altering the beta function the parameters of the ellipse being measured can be changed. This allows for a complete sampling of all the parameters involved in the ellipse if the

beta function, hence the phase advance when equation 1.8 is considered, is taken into account.

Although the magnetic fields do not change the energy of the particle they do change the path of the particle. If a Cartesian coordinate system is used in such a way as to define the intended path of motion of the beam as s, the horizontal direction that is perpendicular to the beam path as x and the vertical direction as y the ideal particle has a non-zero velocity in the s direction and zero velocity in the other two directions. This means that the magnetic field only has transverse components with respect to the particle. The Taylor expansion of the vertical magnetic field leads to

$$B_y(x) = x^0\ B_{y0} + x^1\ dB_y/dx + x^2\ 1/2!\ d^2B_y/dx^2 + ... \tag{1.10}$$

For a particle moving in the horizontal plane through a magnetic field there is a balance between the Lorentz force $F_x = -e\upsilon_s B_y$ and the centrifugal force $F_y = m\upsilon_s^2/R$, where R is the radius of curvature of the trajectory. Since $p = m\upsilon_s$ the forces are balanced so that

$$\frac{1}{R(x,y,s)} = \frac{e}{p}B_y(x,y,s) \tag{1.11}$$

If this is combined with equation 1.10 a set of multipole terms are derived. These multipole terms determine how a particle's trajectory is affected by the varying degrees of the magnetic field. The number of poles in the magnet that the particle passes through determines the magnitude of each multipole term. For example in a dipole magnet all of the multipole terms are typically negligible for the ideal particle, as such the multipole term is roughly $\frac{1}{R(x,y,s)} = \frac{e}{p}B_{y0}$ where as for a quadrupole magnet the quadrupole multipole $K_1 = \frac{e}{p}\frac{dB_y}{dx}$ must also be considered as an important factor. The trajectory altering effects of a dipole magnet are invariant of the offset from the ideal particle position while the trajectory altering effects of a quadrupole magnet are larger for particles that are further away from the ideal particle position. This means that dipole magnets are used to bend the beam while quadrupoles are used to focus the

beam, however a quadrupole magnet cannot focus in both the horizontal and vertical directions at the same time. If a quadrupole is focusing the beam horizontally it must be defocusing the beam vertically. To compensate for this inability to focus the beam in both transverse planes at the same time the quadrupole magnets are placed in a sequence which has a horizontally focusing (vertically defocusing) quadrupole, followed by a gap to allow for the focusing to take effect, and then a vertically focusing (horizontally defocusing) quadrupole which is followed by a gap to allow for the focusing to take effect. This is called a F0D0 cell and results in any off-centre particles performing an oscillation around the centre of the beam.

The magnetic fields generated by the quadrupole and dipole multipole terms are referred to as linear magnetic fields because the effect of the field on a particle is linearly related to the position of the particle with respect to the centre of the magnet. The magnetic fields generated by the higher order magnetic fields are non-linear fields because the strength of the magnetic field is not linearly related to the distance from the centre of the field. For example, a sextupole field is related to the square of the distance to the centre. Since the higher non-linear multipole fields do still exist in dipole and quadrupole magnets, but at significantly lower levels near the centre, the strength of these fields experienced by a particle increases the further the particle is from the centre. This is related also to how much higher the multipole term is from the intended multipole term, e.g. a quadrupole magnet has a much higher sextupole term than a dipole magnet where as the octupole term is still significantly negligible. As a result if a beam passes sufficiently off-centre through a quadrupole magnet it will experience a non-negligible sextupole field, which is increasingly stronger for the more off-centre particles. This leads to emittance growth, which can be calculated using the following formula [5]:

$$\varepsilon_{y-proj}^2 = \varepsilon_{y-in}^2 + \varepsilon_{x-in}\,\varepsilon_{y-in}\,\beta_x\,\beta_y\,K_2 L \times\; L\,(\Delta_y^2 + \varepsilon_{y-in}\,\beta_y) \tag{1.12}$$

where ε are the horizontal (x) and vertical (y) emittance values before (in) and after ($proj$) the quadrupole, β are the beta function values at the quadrupole, K_2L is the sextupole coefficient of the quadrupole, L is the length of the quadrupole and Δ_y is the vertical offset of the extracted beam within the quadrupole.

The effects of a magnet on the position and momentum of a particle can be expressed in the form of a transfer matrix. The same is true for an accelerating structure and all other accelerator components, including empty vacuum tubes, which can be described as a drift region that does not alter the momentum of the particle. If the longitudinal direction (s), the horizontal transverse direction (x) and the vertical transverse direction (y) are treated as separate (uncoupled), the horizontal transfer matrices ($\mathbf{M}_x$) of various different components are shown below:

Accelerating cavity:

$$\mathbf{M_x} = \begin{pmatrix} 1 & \Delta s \\ 0 & 1 \end{pmatrix} \tag{1.13}$$

Dipole magnet:

$$\mathbf{M_x} = \begin{pmatrix} 1 & \Delta s \\ 0 & 1 \end{pmatrix} \tag{1.14}$$

Horizontally focusing quadrupole magnet:

$$\mathbf{M_x} = \begin{pmatrix} \cos\sqrt{|K|}\Delta s & \frac{1}{\sqrt{|K|}}\sin\sqrt{|K|}\Delta s \\ -\sqrt{|K|}\sin\sqrt{|K|}\Delta s & \cos\sqrt{|K|}\Delta s \end{pmatrix} \tag{1.15}$$

Horizontally defocusing quadrupole magnet:

$$\mathbf{M_x} = \begin{pmatrix} \cosh\sqrt{|K|}\Delta s & \frac{1}{\sqrt{|K|}}\sinh\sqrt{|K|}\Delta s \\ \sqrt{|K|}\sinh\sqrt{|K|}\Delta s & \cosh\sqrt{|K|}\Delta s \end{pmatrix} \tag{1.16}$$

Drift:

$$\mathbf{M_x} = \begin{pmatrix} 1 & \Delta s \\ 0 & 1 \end{pmatrix} \tag{1.17}$$

where

$$\begin{pmatrix} x \\ p_x \end{pmatrix}_{s_1} = \mathbf{M_x} \times \begin{pmatrix} x \\ p_x \end{pmatrix}_{s_0} \tag{1.18}$$

The focal length (f) of the magnets and is related to the value of k of the magnet by $f = k \cdot l_q$. Since f is normally much longer than the length of the magnets it is to treat the magnets as thin lenses. This leads to different transfer matrices for the quadrupole magnets:

Horizontally focusing quadrupole magnet:

$$\mathbf{M_x} = \begin{pmatrix} 1 & 0 \\ \frac{1}{f} & 1 \end{pmatrix} \tag{1.19}$$

Horizontally defocusing quadrupole magnet:

$$\mathbf{M_x} = \begin{pmatrix} 1 & 0 \\ \frac{-1}{f} & 1 \end{pmatrix} \tag{1.20}$$

The combination of all the transfer matrices between one location and another is known as a response matrix. As long as the Twiss parameters are known at one location and the response matrix between that location and another location are known, the Twiss parameters can be calculated at the other point. If

$$M_{s_{0\to1}} = \begin{pmatrix} m_{11} & m_{12} \\ m_{21} & m_{22} \end{pmatrix} \tag{1.21}$$

then

$$\begin{pmatrix} \beta \\ \alpha \\ \gamma \end{pmatrix}_{s_1} = \begin{pmatrix} m_{11}^2 & -2m_{11}m_{12} & m_{12}^2 \\ -m_{11}m_{21} & m_{12}m_{21} + m_{11}m_{22} & -m_{12}m_{22} \\ m_{21}^2 & -2m_{21}m_{22} & m_{22}^2 \end{pmatrix} \cdot \begin{pmatrix} \beta \\ \alpha \\ \gamma \end{pmatrix}_{s_0} \tag{1.22}$$

This can be done in reverse in order to calculate the initial Twiss parameters needed to result in a given set of Twiss parameters or to calculate the response matrix needed to turn an initial set of Twiss parameters into a given set of Twiss parameters.

Given that the beamsize (σ) is given by $\sigma = \sqrt{\varepsilon\beta}$ it is possible to use measurements of the beamsize at multiple positions along the beamline and knowledge of the transfer matrices between the positions to calculate the Twiss parameters and the emittance. One way of doing this is to use wire-scanners, which 'scans' the width of the beam-pipe with a wire and detects where interactions between the beam and the wire happen in the beam-pipe. When the electron beam collides with the wire there is a release of photons which travel along the beamline to a 'gamma counter'. The number of photons detected at the detector is proportional to the number of electrons which have impacted the wire. This gives a reading of the width of the beam at that point in that direction. If a Gaussian is then fitted to the results, the beamsize may be measured.

If the phase space of a beam is assumed to be elliptical, the vertical emittance ε_y is given by [6]:

$$\varepsilon_y = \beta_y < y'^2 > +2\alpha_y < yy' > +\gamma_y < y^2 > \tag{1.23}$$

Where β_y, α_y and γ_y are the vertical Twiss parameters and y and y' are the vertical position and angle of the particles of the beam respectively. This equation also applies if altered for use in the horizontal plane.

Given the assumption that the emittance is constant, using $\beta\gamma - \alpha^2 = 1$ and com-

bining equation 1.23 and equation 1.22, we arrive at a situation where we can calculate $< y^2 >$, $< yy' >$ and $< y'^2 >$ at a wire-scanner WS1 if we have the vertical beamsizes from at least three wire-scanners and the response matrices between them. This gives us the following equation:

$$\begin{pmatrix} < y^2 > \\ < yy' > \\ < y'^2 > \end{pmatrix} = \begin{pmatrix} R_{33}^{2\,WS1} & 2R_{33}R_{34}^{\;\;WS1} & R_{34}^{2\,WS1} \\ R_{33}^{2\,WS1\rightarrow WS2} & 2R_{33}R_{34}^{\;\;WS1\rightarrow WS2} & R_{34}^{2\,WS1\rightarrow WS2} \\ R_{33}^{2\,WS1\rightarrow WS3} & 2R_{33}R_{34}^{\;\;WS1\rightarrow WS3} & R_{34}^{2\,WS1\rightarrow WS3} \end{pmatrix}^{-1} \bullet \begin{pmatrix} \sigma_y^{2\,WS1} \\ \sigma_y^{2\,WS2} \\ \sigma_y^{2\,WS3} \end{pmatrix} \tag{1.24}$$

where σ denotes the beamsize, WS1, WS2 & WS3 are the wire-scanners used, which denote where the measurements were made and between which two points the response matrix terms come from. There is a catch with this method, in order for equation 1.24 to be true, there needs to be a phase advance of roughly π/N between each wire-scanner (where N is the number of wire-scanners used) otherwise the phase space ellipse has not been fully sampled, leading to a poor phase space ellipse representation.

Another important parameter of the beam is the dispersion of the beam, which is a measurement of the trajectories of the particles in the beam that experience a deviation from the nominal momentum ($\Delta p/p \neq 0$). This momentum deviation is only significant if the trajectory of the particle is being changed. If a special trajectory $D(s)$ is defined as the trajectory of a particle with a momentum deviation of $\Delta p/p = 1$ then $D(s)$ is called the dispersion function. In a dipole magnet with a bending radius of R

$$D''(s) + \frac{1}{R^2}D(s) = \frac{1}{R} \tag{1.25}$$

This is an inhomogeneous differential equation and the homogeneous form of the equation is the path of a particle through a bending magnet. The solution (D_p) to the inhomogeneous equation is a constant and as such

$$\frac{D_p}{R^2} = \frac{1}{R} \rightarrow D_p = R \tag{1.26}$$

therefore

$$D(s) = D_0 \cos\frac{s}{R} + D'_0 \sin\frac{s}{R} + \left(1 - \cos\frac{s}{R}\right) D'(s) = -\frac{D_0}{R}\sin\frac{s}{R} + D'_0 \cos\frac{s}{R} + \sin\frac{s}{R} \quad (1.27)$$

Now equation 1.18 becomes

$$\begin{pmatrix} x \\ p_x \\ \Delta p/p \end{pmatrix}_{s_1} = \mathbf{M_x} \times \begin{pmatrix} x \\ p_x \\ \Delta p/p \end{pmatrix}_{s_0} \quad (1.28)$$

and the transfer matrices become 3×3 matrices.

The situation becomes more complex if the longitudinal, horizontal and vertical planes are not independent (coupled), for example when a horizontally focusing quadrupole is rotated about the path of motion. In this situation the quadrupole is focusing in the plane that is θ° away from the horizontal plane, where θ° is the angle of rotation from its original alignment, and is defocusing in the plane that is $(\theta + 90)^\circ$ away from the horizontal plane. This will mean that the horizontal and vertical positions, momenta and dispersion functions of the particle upon entering the quadrupole will affect the horizontal and vertical positions, momenta and dispersion functions of the particle upon exiting the quadrupole. This means that either the horizontal and vertical planes must be redefined at the start and end of the quadrupole so as to correspond to the new alignment, which requires that the horizontal and vertical positions, momenta and dispersion functions need to be calculated for the new alignment, or a 6x6 transfer matrix must be used.

2

Emittance Growth Studies at ATF

2.1 Chapter Overview

The Accelerator Test Facility (ATF) in KEK, Japan was upgraded to ATF2 in late 2008. ATF was an ultra-low emittance damping ring and extraction region with the goal of proving that the ultra-low emittance beam needed for ATF2 could be created and extracted into the planned final focus section of ATF2. The ATF has suffered from emittance growth in the extraction region with the normalised vertical emittance being a factor of three larger in the extraction line than in the damping ring [7]. The source of the emittance growth was narrowed down to the area between the extraction kicker magnet and the extraction septa magnets (QM6R and QM7R). To find the specific reason for the the emittance growth at ATF and to find a solution, an international team of physicists was formed to study the magnets in the extraction region. The studies undertaken involved simulation studies and studies at ATF, whereby measurements of the emittance growth were made while changes to the path of the beam through the extraction region were made. The details of the investigations are presented along with the chosen solution to the problem.

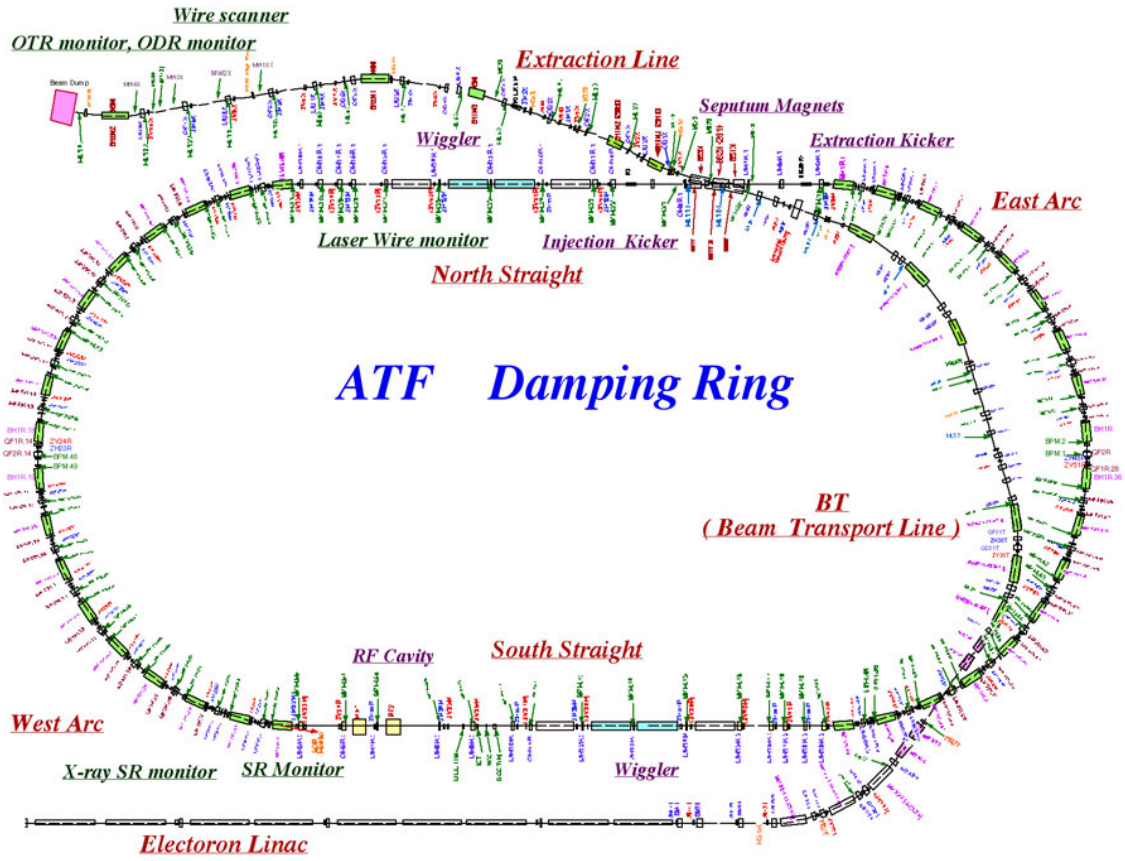

Figure 2.1: The layout of ATF.

2.2 Emittance Growth Problems at ATF

The Accelerator Test Facility (ATF, Fig. 2.1) in KEK, Japan was designed as a test-bed for the development of equipment and techniques required to generate an ultra-low emittance beam. Ultra-low emittance beams are a key requirement for the development of future high-energy linear electron-positron colliders. ATF has been designed to generate a 1.28 GeV electron beam, which is 'fed' into a 138 m damping ring (DR) where the resultant normalised vertical emittance ($\gamma \cdot \varepsilon_y$) is of the order of 10 nm·rad. The beam is extracted from the damping ring into an extraction line (EXT) which houses a range of beam diagnostic tools and leads to a beam dump. The design parameters are also referred to as the nominal parameters. ATF contains a range of magnets and monitoring equipment including an x-ray synchrotron radiation beamsize moni-

tor (XSR) in the damping ring and a set of 5 wire-scanner beam size monitors in the extraction line. A more detailed introduction to ATF can be found at the official ATF introduction webpage [3].

The lowest recorded normalised vertical emittance in the ATF damping ring is 15 nm·rad, however the normalised vertical emittance in the extraction line has been shown to be a factor of about three bigger than the emittance in the damping ring (48 nm·rad, [7]). There is also a strong dependence between the intensity of the beam and the vertical emittance in the extraction line (Fig. 2.2).

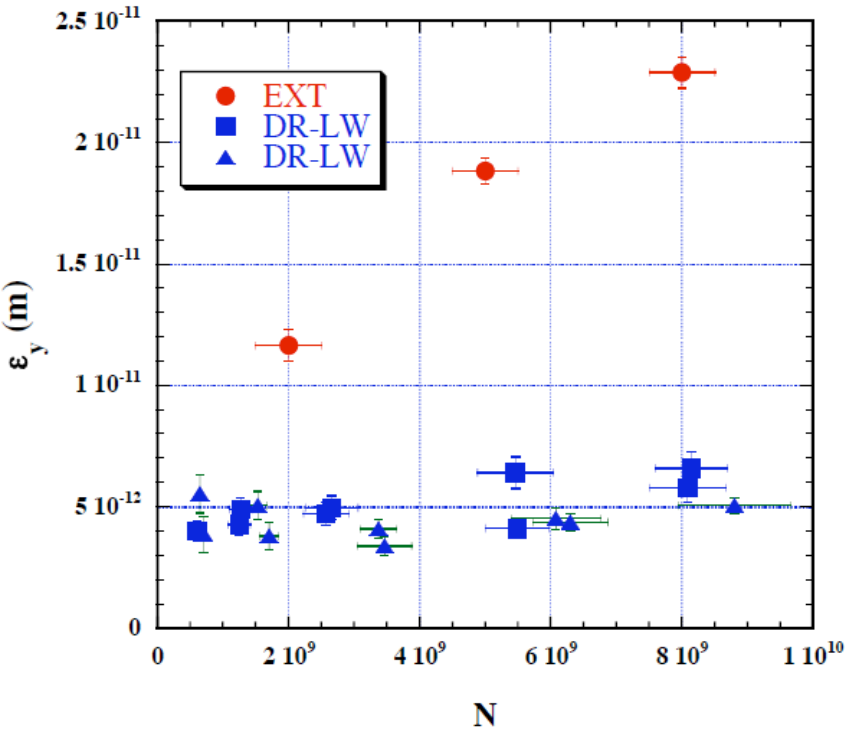

Figure 2.2: Vertical emittance vs. bunch intensity N, measured in the extraction line using wire scanners (EXT) and measured in the damping ring using the laserwire monitor (DR-LW). [7]

ATF2 is an upgrade to ATF that replaced the extraction line section with a redesigned extraction line and a final focus section. The main goal of ATF2 is to achieve

focusing of the beam at the IP down to a vertical beamsize of 37 nm. This will require a normalised vertical emittance of 30 nm·rad (2 times ATF damping ring emittance, 2/3 the ATF extraction line emittance). The ATF2 upgrade began in late 2008, however the emittance growth in the ATF EXT had to be dealt with before this date.

The following is a quote from the ATF2 proposal vol. 1 [7] which details the main reason for the beam studies at ATF:

> The observed intensity dependence of the vertical emittance is also much stronger in the extraction line than in the damping ring. This dependence is also larger than the intensity dependence of the longitudinal and horizontal emittances. This strong intensity dependence cannot be explained by linear coupling between the vertical and either of the other two axes. We suspect that unknown nonlinear fields in the extraction kicker and the septum magnets cause higher-order x-y and/or energy-y coupling. The normalised vertical emittance (at $N = 5\times10^9$) is about 48 nm, which is larger than in the damping ring (about 15 nm) by a factor of three, while the nominal ATF2 goal emittance is 30 nm. If the vertical emittance cannot be reduced to the nominal value, it would make the vertical beam spot size larger than nominal size by about 30%, for an intensity of 5×10^9. For 2×10^{10} the blow up would be even larger.

Wakefields in the extraction region and the non-linear fields in the two damping ring quadrupoles in the extraction region were also considered to be possible candidates for the emittance growth. In 2007 an international collaboration was formed to investigate one of the possible sources for the emittance growth. The possible source chosen was the non-linear fields in the damping ring quadrupoles that are situated between the extraction kicker magnet and the extraction septa magnets (QM6R and QM7R).

2.3 Multipole Studies

The process of extracting a beam from a damping ring is not instantaneous. The beam is gradually steered out of the ring. At ATF, a kicker is used to horizontally displace the extracted bunch or bunches. The 'kicked' bunch then travels off-centre through two quadrupoles, QM6R and QMR7, which are vertically and horizontally focusing respectively (Fig. 2.3 and Fig. 2.4). A sufficiently off-centre quadrupole exhibits a bending effect on the beam with the bending direction being the same as the focusing direction. This means that the 'kicked' bunch is steered more off-centre by QM6R and steered back towards the centre by QM7R. The stored beam is nominally focused by QM6R and QM7R and does not experience any bending field. The net result of the kicker and off-centre steering of the 'kicked' bunch is that it passes through the extraction side of the septum magnets which bend the bunch away from the damping ring into the extraction line. As a result of the extraction, the extracted beam experiences the off-centre fields of QM6R, QM7R and the septum magnets.

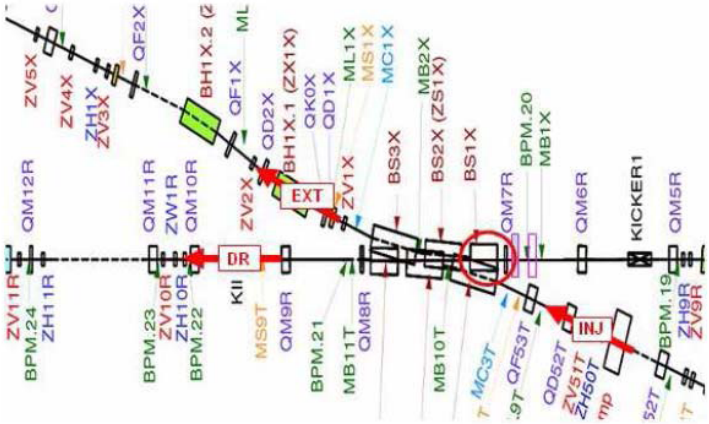

Figure 2.3: A closer look at the ATF injection/extraction region.

Quadrupole and dipole fields are referred to as linear magnetic fields because the effect of the field on a particle is linearly related to the position of the particle with

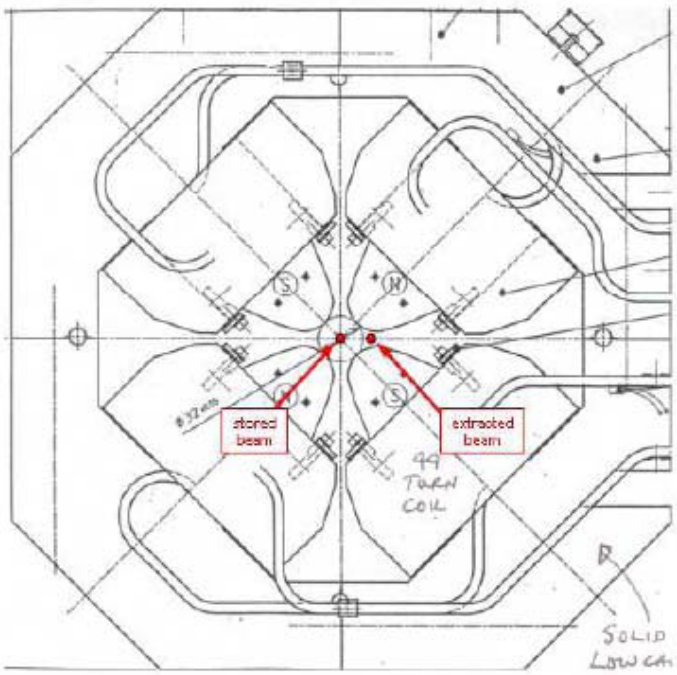

Figure 2.4: A design sketch of QM7R with the nominal positions of the stored and extracted beams labelled [8].

respect to the centre of the magnet. A sextupole field is a non-linear field because the strength of the magnetic field is related to the square of the distance from the centre of the field. A quadrupole magnet does not just generate a quadrupole field, it generates a range of multipole fields. The existence of multipoles can be shown through the Taylor expansion of the magnetic field (B) [9]:

$$B_y(x) = B_{y0}\, x^0 + x^1\, dB_y/dx + x^2\, 1/2!\, d^2B_y/dx^2 + ... \tag{2.1}$$

The Quadrupoles and septum magnets were modelled using a finite element code and the multipole coefficients were measured [10]. When the beam is extracted through QM7R it is of the order of 2.25 cm off-centre in the horizontal direction, which leads to the following horizontal magnetic field [11]:

$$B_y = 0.461227 + 17.5409\, x - 975.611\, x^2 - 164990\, x^3 - 1.8345x10^7\, x^4 + ... \tag{2.2}$$

The resultant multipole coefficients (K_nL) of QM7R for an extracted beam were calculated (Table 2.1).

Table 2.1: A list of the multipole coefficients of QM7R for an extracted beam

n	K_nL	**MAD notation**
1	0.00839	K0L
2	0.3192	K1L
3	-35.507	K2L
4	-1.80e4	K3L
5	-8.01e6	K4L
6	2.68e9	K5L

where K_nL is in units of m^{-n} and is calculated using the following formula:

$$K_nL = L/B_0\rho_0 \cdot \delta^n B_y/\delta x^n \tag{2.3}$$

where L is the magnet length and $B_0\rho_0$ is the magnetic rigidity.

This demonstrates that QM7R has a non-negligible sextupole component for the extracted beam, which is strongly dependent on the horizontal and vertical position of the extracted beam. The emittance growth due to the sextupole field can be calculated using the following formula [5]:

$$\varepsilon^2_{y-proj} = \varepsilon^2_{y-in} + \varepsilon_{x-in}\,\varepsilon_{y-in}\,\beta_x\,\beta_y\,K_2\,L^2\,(\Delta^2_y + \varepsilon_{y-in}\,\beta_y) \tag{2.4}$$

where ε_y is the vertical (y) emittance values before (in) and after (proj) QM7R. ε_{x-in} is the horizontal (x) emittance value before QM7R, β are the beta function values at QM7R, K_2L is the sextupole coefficient of QM7R, L is the length of QM7R (120 mm) and Δ_y is the vertical offset of the extracted beam within QM7R. The emittance growth from the multipole fields can also be estimated by using a particle tracking code to track a beam through a simulated QM7R magnet with and without the multipole components (Fig. 2.5) [12]. Both show a dependency between the emittance growth and the

vertical position of the beam in QM7R, the strength of this dependency is related to the sextupole coefficient of QM7R and offers a method for empirically calculating the sextupole coefficient of QM7R, as well as the relationship between the vertical emittance growth of the extracted beam and its path through QM7R. The incremental change in the extracted beam's vertical offset through QM7R was chosen as the main method for proving the theory that QM7R was the major reason for the emittance growth in the ATF extraction line.

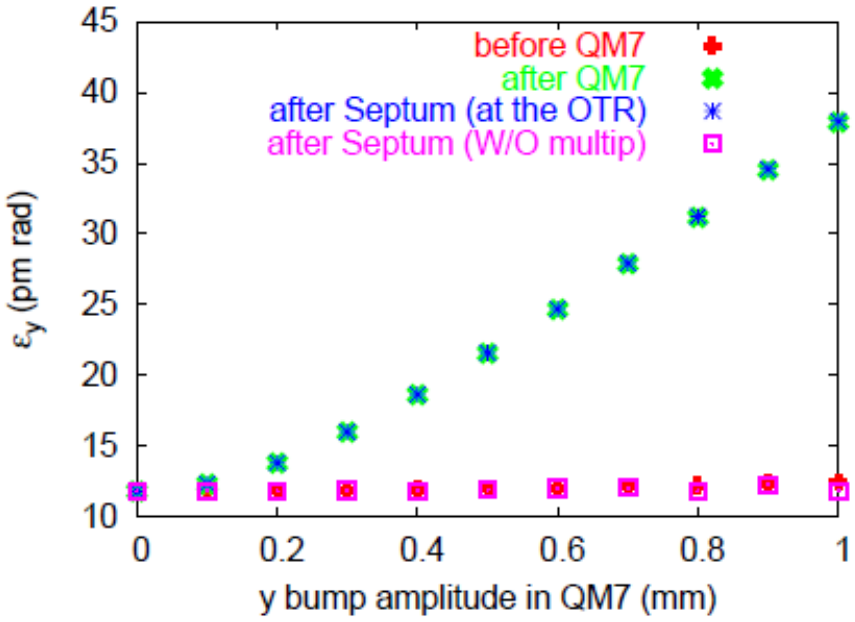

Figure 2.5: Vertical emittance vs. vertical off-set (bump amplitude) in QM7R at different locations of the EXT line, from tracking simulations with and without the multipole coefficients shown in Table 2.1.

2.4 Experimental Methods

2.4.1 Bump Creation

Changing the position of the extracted beam through QM7R is the best way of proving that the non-linear fields in QM7R are a major factor in the vertical emittance growth.

It can also be seen that a change in the vertical path of the beam generates a larger increase in the vertical emittance (Fig. 2.6).

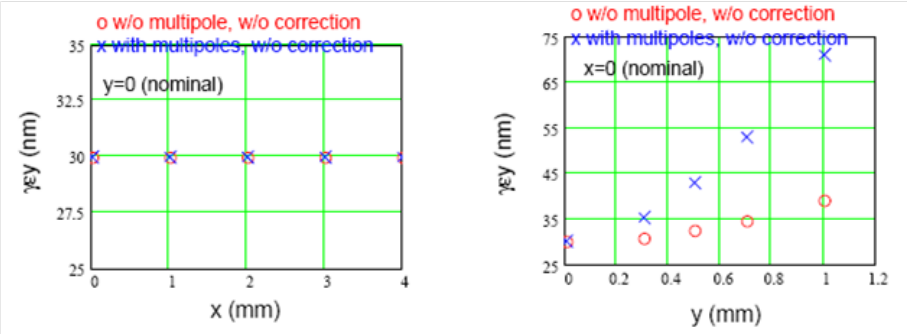

Figure 2.6: A comparison of the effects of a horizontal and vertical bump through QM7R on the vertical emittance of the ATF extraction line.

The change in the vertical path of the beam through QM7R calls for the creation of a vertical 'bump' (Fig. 2.7).

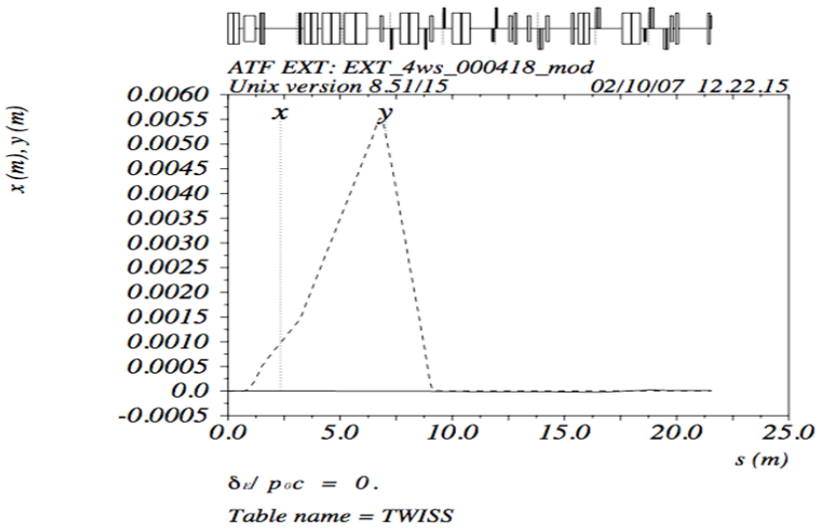

Figure 2.7: A plot of a closed 4 magnet bump through QM7R using the MAD tracking code.

This bump needs to distort the beam path through the other magnets as little as pos-

sible. It must also be closed in the damping ring, however from experimental tests it has been found to be acceptable if the bump is not closed in the extraction line because the extraction line orbit must always be corrected after the creation of the bump. These bumps were generated using the MAD tracking code. To increase the accuracy of the bumps, a MAD input deck was generated using the settings of the 'real world' ATF control system, which includes the current magnet strengths. This used 4 vertical correctors (ZV8R, ZV9R, ZV10R and ZV11R) to create a closed bump of a desired value at QM7R. After a short time it became possible for a 3 corrector bump to be created when the vertical corrector ZV100R was added to the damping ring. This corrector was held in place with duct tape, so may have been a possible source of error during these studies. During a 3 corrector bump, correctors ZV9R, ZV100R and ZV10R were used.

A problem that arose during many of our investigations at ATF was the limitations on the correctors, namely the 5 amp limit on ZV9R, which usually operates close to 4 amps when no bump is present. This meant that it was necessary to generate a closed bump using ZV6R, ZV8R and ZV9R that would have no effect on the position at QM7R, but would reduce the strength of ZV9R before any other bumps could be generated. Due to the power limitations of the correctors it was decided to keep the bump at QM7R to between -1.0 mm and 1.0 mm.

2.4.2 Wire-Scanner Measurements

The diagnostic section of the ATF extraction line contains 5 wire-scanners (MW0X, MW1X, MW2X, MW3X and MW4X). These wire-scanners are used to measure the beamsize at multiple positions along the beamline by 'scanning' the beam profile with a wire and detecting where interactions between the beam and wire happen in the beam-pipe. Each wire-scanner contains a number of tungsten wires including hori-

zontally (to measure y size) and vertically (to measure x size) oriented wires, a 10 degree wire and a wire perpendicular to the direction of motion of the wire-scanner (u), as well as a 10 μm and a 50 μm gold-plated tungsten wires (Fig. 2.8). The horizontally orientated wire measures the vertical beamsize and vice-versa. The motion of the wire-scanner is at a 45° angle, MW2X is positioned at a perpendicular angle to all other wire-scanners (Fig. 2.9).

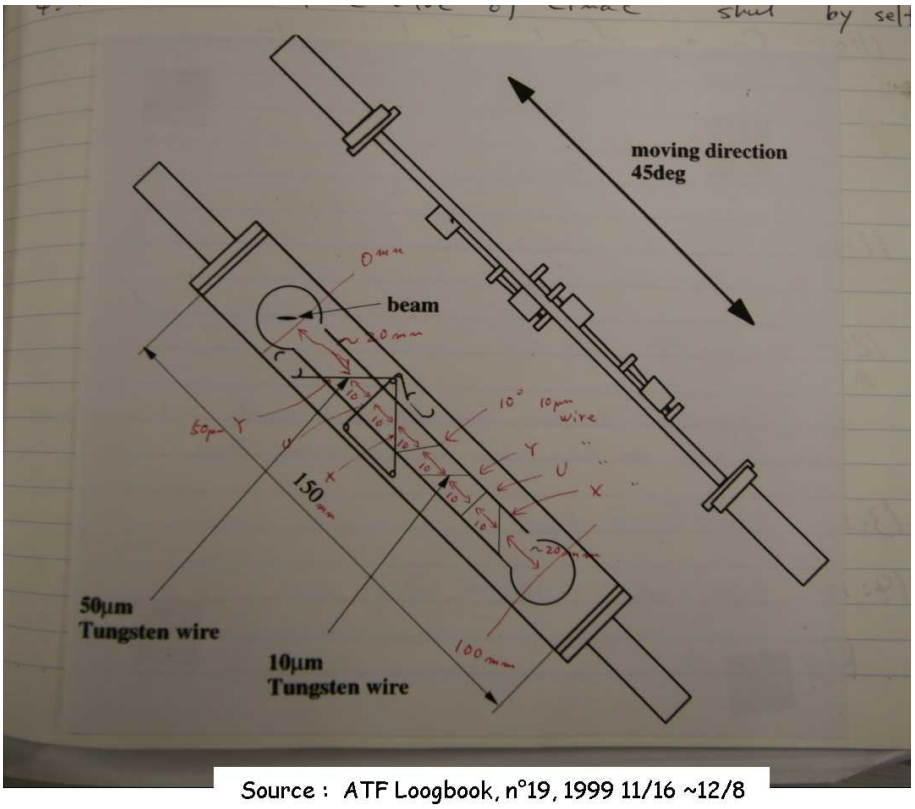

Figure 2.8: An annotated sketch of a wire-scanner at ATF with all the wires, the beam and the mover system shown.

The wire-scanner control software positions the desired wire into the path of the beam. When the electron beam collides with the wire there is a release of photons which travel along the beamline to a 'gamma counter'. The number of photons detected is proportional to the number of electrons which have impacted the wire. The wire will wait a uniform amount of time while tallying the number of photons reaching

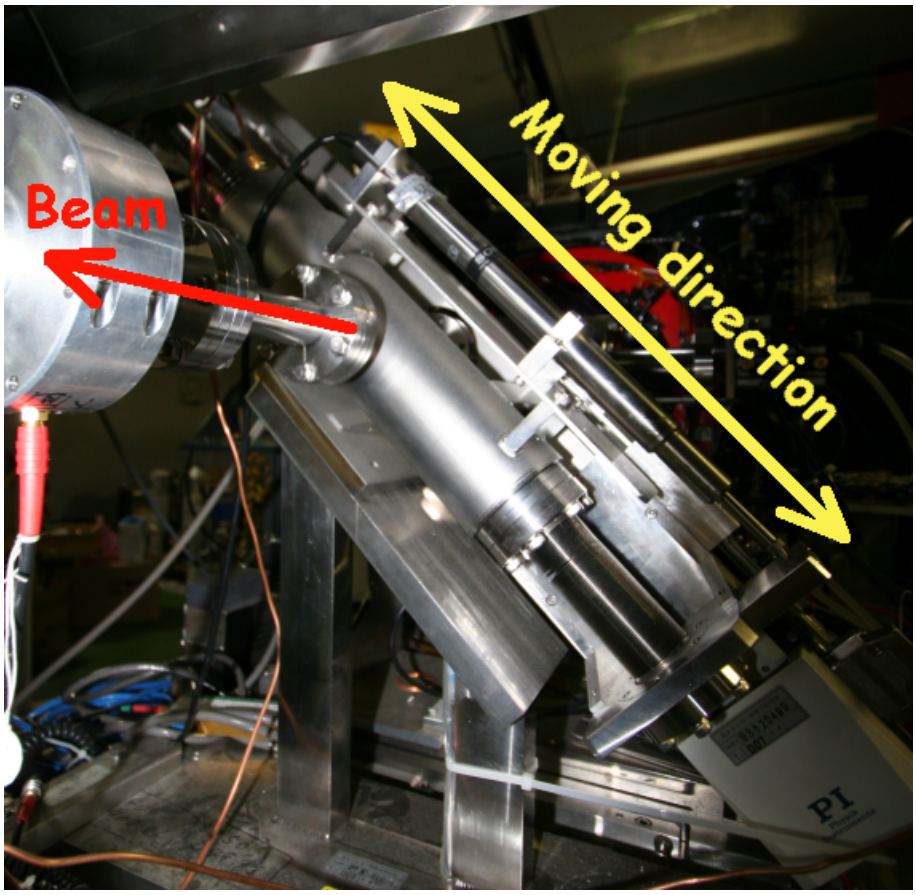

Figure 2.9: A photograph of a wire-scanner at ATF with the beam-pipe clearly visible. The directions of motion for the wire-scanner and beam are shown.

the detector before moving a uniform selectable distance and repeating the measurements. The end result is a 'mapping' of the beam (Fig. 2.10). If a Gaussian is then fitted to the results, the beamsize may be measured (Fig. 2.11).

The errors in the wire-scanner beamsize measurements result from the uncertainty in the wire position and gamma count, the thickness of the wire (which generates a 'binning' effect on the results) and beam position jitter effects between and during each wire-scanner movement.

If the phase space of a beam is assumed to be elliptical, the emittance ε is given

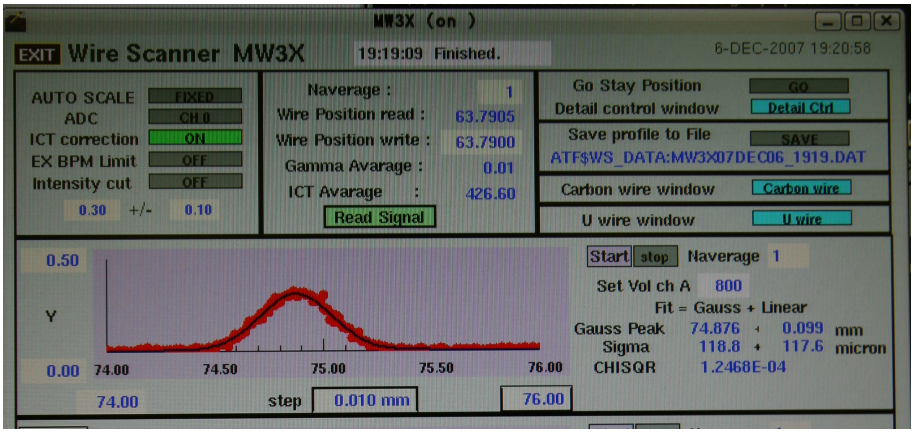

Figure 2.10: A photograph the ATF wire-scanner control software after a full wire-scan has been completed. A Gaussian has been fitted and the beamsize has been calculated.

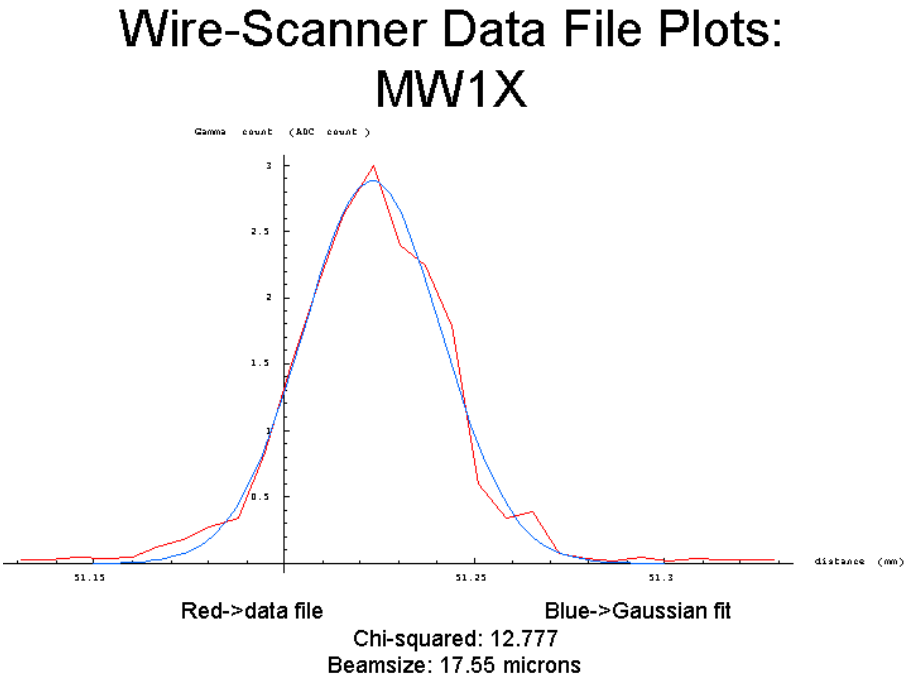

Figure 2.11: A plot of the raw gamma counter readings versus the vertical position of the ‘y’ wire. A Gaussian has been fitted and the beamsize has been calculated.

by [6]:

$$\varepsilon_y = \beta_y < y'^2 > +2\alpha_y < yy' > +\gamma_y < y^2 > \tag{2.5}$$

where β_y, α_y and γ_y are the vertical Twiss parameters and y and y' are the vertical position and angle of the particles of the beam respectively. If one knows the response matrix (**R**) between two points along the beamline and knows the Twiss parameters at one of the points it is possible to calculate the Twiss at the other point using:

$$\begin{pmatrix} \beta_1 \\ \alpha_1 \\ \gamma_1 \end{pmatrix} = \begin{pmatrix} R_{33}^2 & -2R_{33}R_{34} & R_{34}^2 \\ -R_{33}R_{43} & R_{33}R_{44} + R_{34}R_{43} & -R_{43}R_{34} \\ R_{34}^2 & -2R_{43}R_{44} & R_{44}^2 \end{pmatrix} \bullet \begin{pmatrix} \beta_0 \\ \alpha_0 \\ \gamma_0 \end{pmatrix} \tag{2.6}$$

Given the assumption that the emittance is constant, using $\beta\gamma - \alpha^2 = 1$ and combining equations 2.5 and 2.6, we arrive at a situation where we can calculate $< y^2 >$, $< yy' >$ and $< y'^2 >$ at wire-scanner MW0X if we have the vertical beamsizes from at least three wire-scanners and the response matrices between them. This gives us the following equation:

$$\begin{pmatrix} < y^2 > \\ < yy' > \\ < y'^2 > \end{pmatrix} = \begin{pmatrix} R_{33}^{2\,MW0X} & 2R_{33}R_{34}^{\;\;MW0X} & R_{34}^{2\,MW0X} \\ R_{33}^{2\,0X\to1X} & 2R_{33}R_{34}^{\;\;0X\to1X} & R_{34}^{2\,0X\to1X} \\ R_{33}^{2\,0X\to2X} & 2R_{33}R_{34}^{\;\;0X\to2X} & R_{34}^{2\,0X\to2X} \end{pmatrix}^{-1} \bullet \begin{pmatrix} \sigma_y^{2\,0X} \\ \sigma_y^{2\,1X} \\ \sigma_y^{2\,2X} \end{pmatrix} \tag{2.7}$$

where σ denotes the beamsize, 0X, 1X and 2X are shorthand for the wire-scanner names, which denote where the measurements were made and between which two points the response matrix terms come from. There is a catch with this method: in order for equation 2.7 to be true there needs to be a phase advance of roughly π/N between each wire-scanner (where N is the number of wire-scanners used) otherwise the phase space ellipse has not been fully sampled, leading to a poor phase space ellipse representation. This is solved by making sure that the gap between the wire-scanners is as close to the position required for a π/N phase advance as is technically possible.

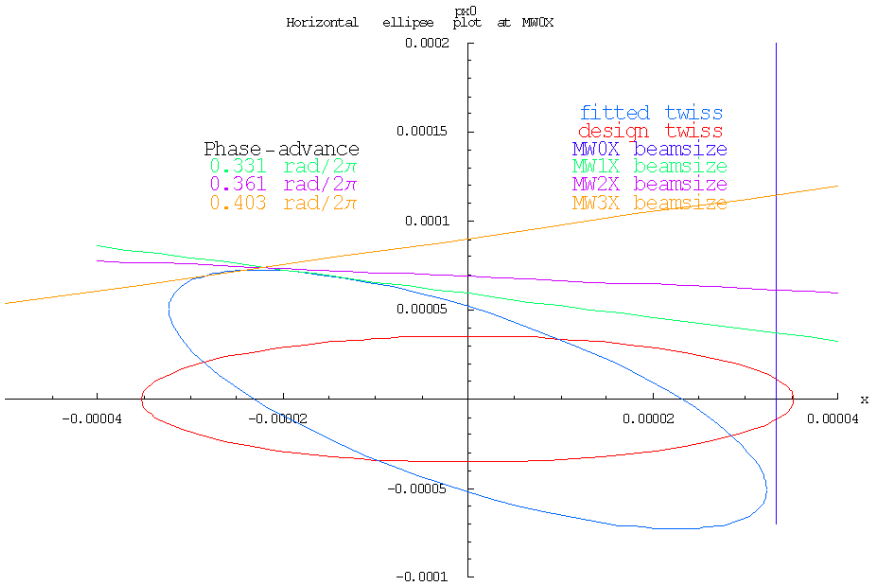

Figure 2.12: A reconstruction of the horizontal phase space at MW0X using real measurement data taken from 4 wire-scanners at ATF and using response matrices generated from simulations using a MAD lattice generated from ATF magnet settings and measurements. The poor phase advance between wire-scanner leads to poor sampling of the phase space ellipse.

Fig. 2.12 was generated as follows [6]. The design phase space ellipse is generated by fitting the design Twiss parameters at MW0X into equation 2.5 and drawing the resultant ellipse in $(x,\ px_0)$ coordinates (the red ellipse in Fig 2.12), where px_0 is the design momentum of the particles of the beam and is defined by $px_0 = \alpha_0 x + \beta_0 x'$. The Twiss parameters fitted to MW0X based on real measurements are then used in the same manner as the design Twiss parameters to plot the fitted phase space at MW0X using the same coordinate system (the blue ellipse in Fig. 2.12). Finally the $(x,\ x')$ range for each wire-scanner is calculated using the measured beamsize and:

$$\begin{pmatrix} x \\ x' \end{pmatrix}_{MW0X} = R^{-1} \bullet \begin{pmatrix} \sigma_w \\ x'_w \end{pmatrix} \tag{2.8}$$

where σ_w is the beamsize at the wire-scanner and x'_w is the undetermined angle variable at the wire, which is related to the phase advance between MW0X and the wire-scanner. The resultant line of permissible $(x,\ px_0)$ values (each of the lines in Fig. 2.12)

values for each one of the wire-scanners are then plotted along with the design and fitted ellipses.

2.4.3 OTR Measurements

During the course of the experiments at ATF, a new beamsize monitor, the Optical Transition Radiation monitor (OTR) was installed in the extraction line. The OTR monitor is situated just after the last extraction septum magnet (Fig. 2.13).

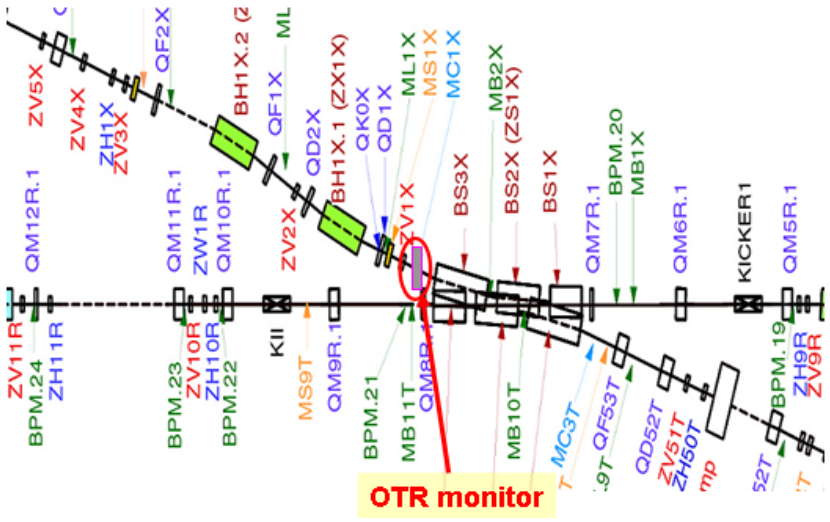

Figure 2.13: The ATF extraction region with the OTR monitor position highlighted.

The OTR monitor is used to measure the transverse beamsize. A screen is inserted into the beampipe which acts as a target for the electron beam. A locally positioned camera gives a live feed of the electromagnetic radiation produced from the electron beam - screen collision. The camera feed is displayed on the ATF control computer and the picture is analysed in order to measure the beamsize (Fig. 2.14).

The OTR is an instantaneous method for measuring the beamsize. The horizontal and vertical beamsizes can be measured simultaneously, along with an estimation of the beam coupling (based on the angle of tilt). The beamsizes can be used in the

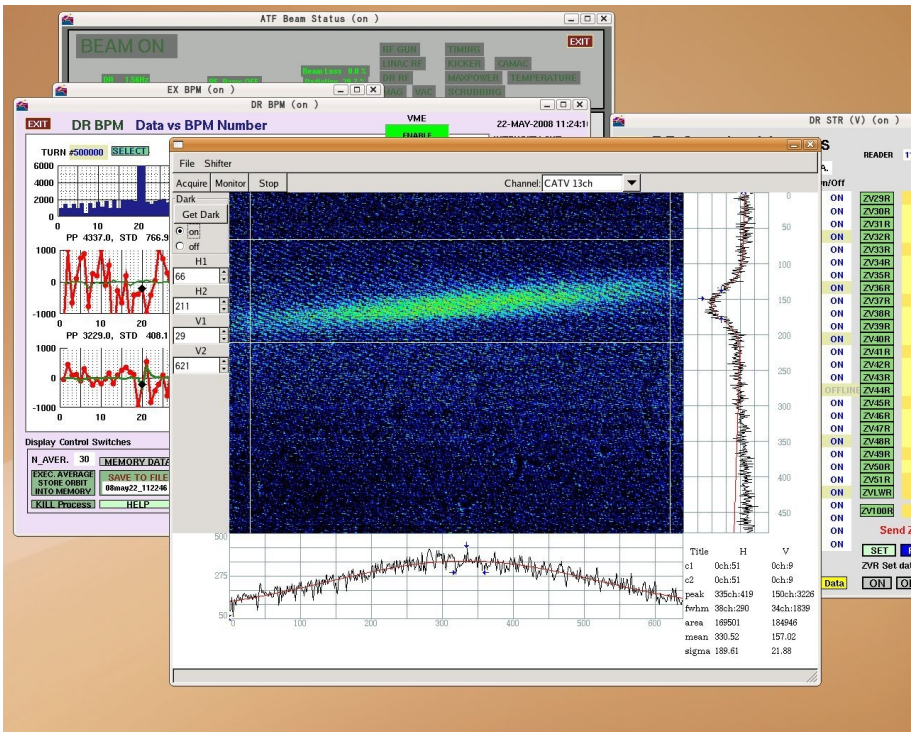

Figure 2.14: A photograph of the OTR monitor output display. The beam can clearly be seen and the beamsize can be measured.

same way as the wire-scanner measurements for emittance measurements. Effects from inter-bunch jitter on the beamsize measurements are reduced due to the instantaneous nature of the OTR measurements, however due to camera saturation and resolution limitations, estimations of the particle density of the beam tend to be less accurate than measurements performed using wire-scanners. The relative proximity between the OTR and QM7R should result in a clearer relation between the beam position within QM7R and the emittance at the measurement point. The minimal number of magnets between QM7R and the OTR should result in a more accurate fitting of the Twiss parameters at the measurement point, which should result in a more accurate conversion between the beamsize at the OTR and the emittance at the OTR, as long as the dispersion at the OTR can be accurately fitted.

2.4.4 Other Measurements

From equation 2.7 it can be seen that the multiple beamsize measurements need not be performed at multiple locations, it is only required that the response matrices between the point of reconstruction and the points of measurement differ by an effective phase difference of π/N, where N is the number of measurements made. If there are a set of quadrupoles between the point of reconstruction and the measuring device, one could change the strengths of the quadrupoles to alter the response matrix enough between each measurement in order to give the desired phase difference. This method is known as 'quad-scanning'. This method can be used to measure the emittance or Twiss parameters for the extraction line while only using one wire-scanner. This negates the necessity for a π/N phase advance between the wire-scanners, which was found to be a difficult situation to guarantee on the real machine. This is also the method used for emittance and Twiss parameter calculations in the damping ring, where the XSR is used in a similar way to the OTR in order to generate instantaneous beamsize measurements.

Another important experimental method that can be performed on ATF is dispersion measurements. Varying the frequency of the RF cavities in the damping ring will alter the momentum of the beam: [14]

$$dp/p = -1/\alpha_c \, df/f \tag{2.9}$$

where p is the momentum of the beam, f is the frequency of the damping ring RF and α_c is the momentum compaction of the bending field:

$$\alpha_c = < D > /R \tag{2.10}$$

where D is the dispersion and R is the physical orbit radius. By recording the orbit for several different frequencies, it is possible to fit the damping ring dispersion using

equations 2.9 and 2.10.

2.5 Experimental Work at ATF

2.5.1 Simulation

It is impossible to directly measure the emittance of a machine. Every method available for use on ATF requires knowledge of the response matrices between the elements of the accelerator. This is impossible to measure on the real machine and must be calculated from a simulation of the accelerator. A more realistic model of the accelerator can be formed by setting the simulated magnets to have the same strengths as the real magnets. This is achieved by recording the magnets' currents from the machine and converting them into strengths using a list of conversion factors that were made based on magnet tests. These tests assume that the beam-magnet misalignment will not significantly change the magnet conversion factor because it is normally too time consuming to evaluate the magnet conversion factors for all expected beam paths. This assumption has been shown to be false in QM7R (Table 2.1), so the simulation is unlikely to have a complete set of realistic multipole coefficients and will not give fully accurate response matrices.

The simulation will also need accurate initial Twiss and beam parameters, dispersion measurements, coupling measurements, BPM and magnet misalignments and corrector settings. The measured dispersion and Twiss parameter values are usually not at the initial position of the simulation and need to be tracked to this point using the simulated machine. The corrector settings, coupling values and element misalignments are sometimes assumed to be insignificant or cancel each other out and are occasionally left out of the simulation. This assumption is treated as true by the ATF's simulation code called 'SAD'. This is also true of the MAD simulations used during the emittance growth investigations. If this assumption is not true and the SAD or MAD simulated

machines differ too much from the real machine then there will be a significant difference between the real and calculated Twiss parameters at the area of reconstruction which could cause errors in the reconstructed beam parameters.

The MAD simulations have also been used to fully simulate the emittance growth effects of QM7R. Beams of between 5000 and 10000 particles were tracked to the first wire-scanner. The vertical positions of all the particles were then collected into 'bins' of the wire thickness (10 microns). The number of particles in the first bin was recorded and a new beam was tracked with an appropriate amount of beam jitter. The same procedure was done with the bins moved by a chosen wire step (2 microns). This was repeated until the whole range of the beam was covered, the process was repeated for each other wire-scanner in turn. A Gaussian was fitted to the particle distribution at each wire-scanner and the beamsizes were recorded (Fig. 2.15). This data can then be used to estimate the emittance that would be calculated using multi-wire measurements and can be compared to the emittance of the MAD beam at MW0X.

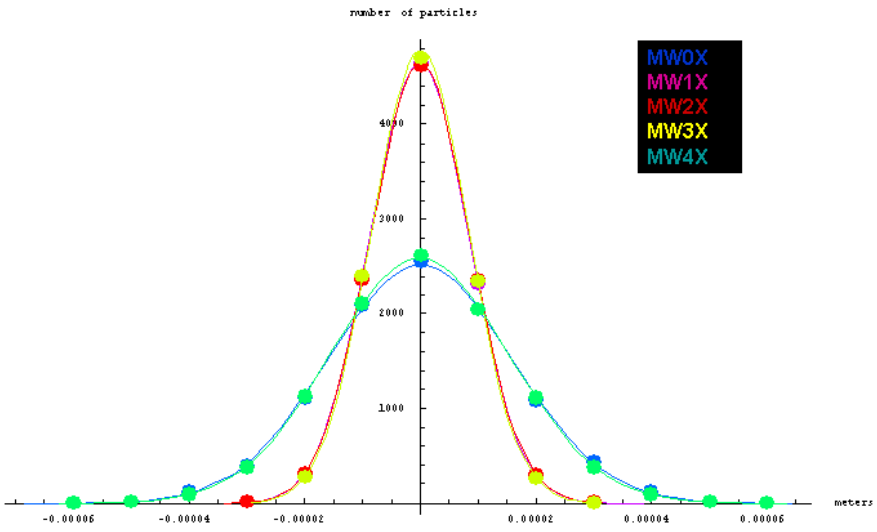

Figure 2.15: MAD simulated wire-scanner measurement results.

MAD was also used to plot the Twiss parameters and phase advances along the extraction line and to calculate the bump settings using the 'instantaneous' MAD 'decks'

that were generated from the current settings of ATF.

Two different methods for emittance reconstruction were attempted by the group. Julien Brossard from LAL ran a 10,000 seed Monte Carlo simulation using MAD, where the beamsizes at each wire-scanner were taken as randomly chosen values from within the error range of the beamsize measurements. The method used for this report used a Nelder-Mead simplex minimiser to find the Twiss and emittance values at MW0X that, when tracked through MAD, would give the combined minimum difference between the simulated and measured beamsizes at each wire-scanner. The error range for my results were formed by taking the maximum and minimum beamsizes for all wire-scanners that were within the error range of the beamsize measurements.

2.5.2 Experimentation

Three separate experimental periods were available to the group for use on ATF. These were November 2007, March 2008 and May 2008. Beam time was limited, however the group managed to secure roughly 190 hours of beam time. Due to the unreliability and instability of critical ATF systems, a significant proportion of the group's beam time was unproductive due to the beam being unusable or unavailable. A significant proportion of the lost beam time was used to steer the beam, correct the dispersion and correct the coupling in the damping ring and extraction line. An uncorrected orbit would make the creation of a bump much harder and would lead to an uncertainty as to which magnets were generating the emittance growth effects. If the dispersion was left too high, the uncertainty in the emittance reconstruction would increase because of the beamsize growth effects caused by the dispersion. These would reduce the relative impact that the emittance growth from the non-linear fields had on the overall beamsize (Fig. 2.16). If the coupling was left uncorrected, there would be vertical emittance growth from the effects of the coupling between the horizontal and vertical planes, which would increase the uncertainties in the emittance reconstructions. The studies

were also hampered because two of the wire-scanners became unusable. MW4X was unavailable due to the installation of a new quadrupole between MW3X and MW4X, which caused an inconsistency between the optics in the simulations and the optics on the real machine.

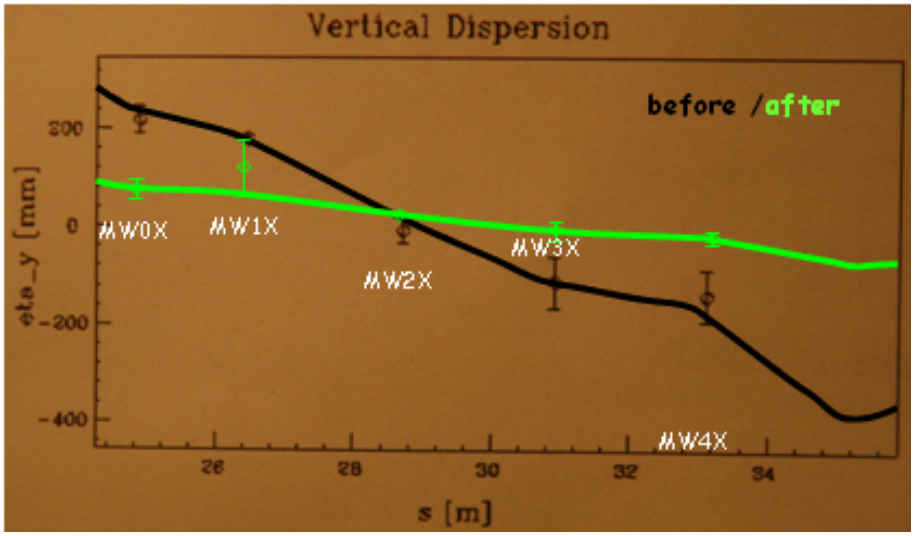

Figure 2.16: Vertical dispersion measurements for the ATF diagnostics section before and after dispersion correction. The target of sub-10 mm dispersion along the diagnostics section could not be reached on this occasion.

It also became evident that the SAD fitted emittance measurements made at ATF suffered from the same problems that the group was experiencing with the wire-scanner simulations. The simulated decks are approximations that ignore coupling and coupling correction, orbit perturbations and orbit corrections and uncertainties in the beam-size measurements, which have been shown to be significant (Fig. 2.17). As such the SAD fitted emittance values were occasionally unrealistic (Fig. 2.18).

The experimental procedures evolved over the course of the studies when sources of error were found. The original procedure was:

- correct the damping ring orbit;

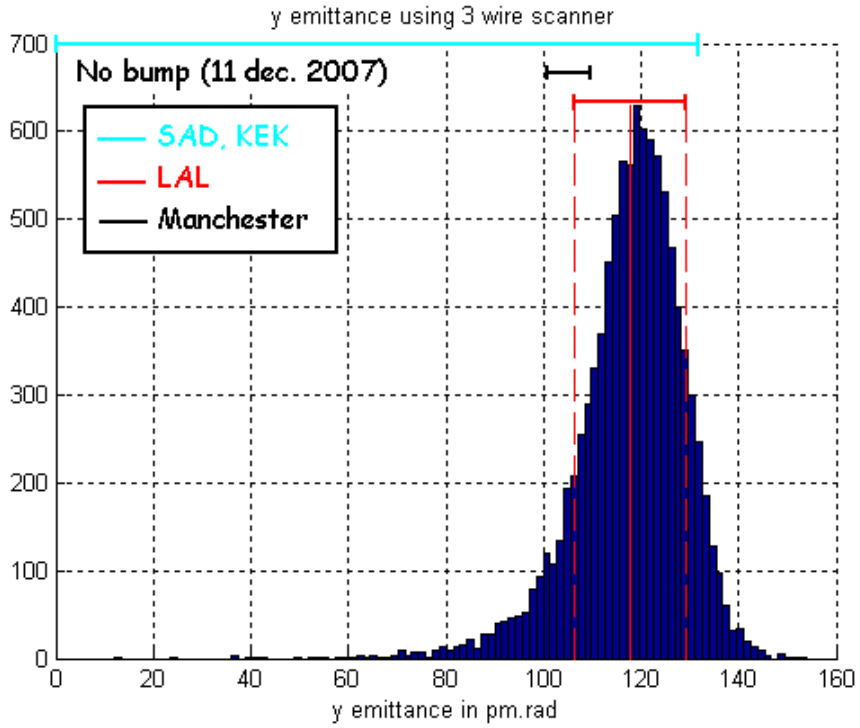

Figure 2.17: A comparison of the emittance ranges from each of the emittance reconstruction methods. These results were taken on 11th December 2007 when no bump was present.

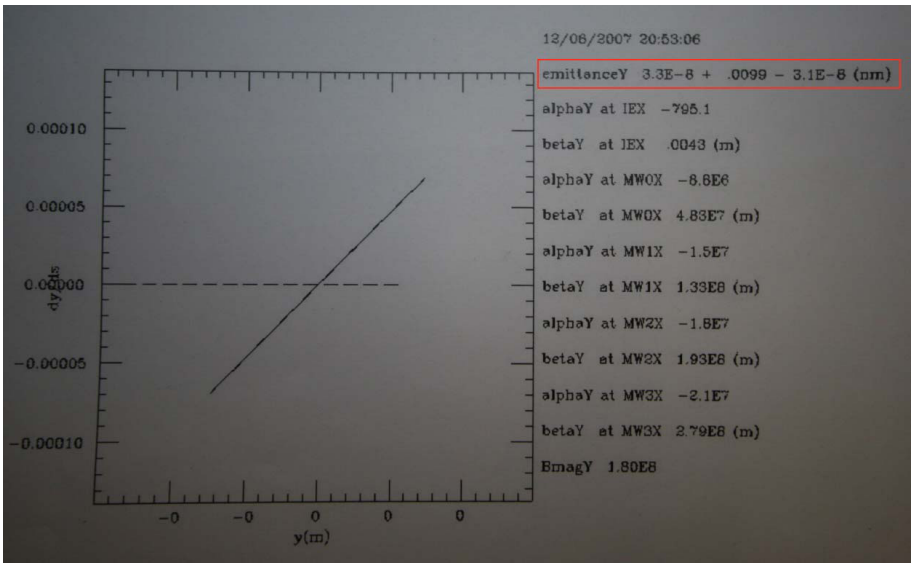

Figure 2.18: SAD multi-wire reconstructed emittance from measurements taken 6th December 2007 when no bump was present.

- apply bump (if any);
- correct damping ring dispersion without using the bump correctors;
- correct the damping ring coupling;
- correct the extraction line orbit;
- correct the extraction line dispersion;
- measure the beamsize three times at each wire-scanner;
- repeat all but first step for each bump value.

This was too time consuming, so the following action was taken:

- the time taken for correction procedures was limited to 2 hours, this generally increased the dispersion at the wire-scanners during the beamsize measurements;
- only take one measurement at each wire-scanner;
- do not follow correction procedures for the damping ring for each bump value.

The overall effect of all these changes was an increase of the uncertainty of the emittance reconstruction. It was then discovered that the phase advance between the wire-scanners were very poor (Fig. 2.19), so a new set of initial optics were generated that should give the ideal phase advances.

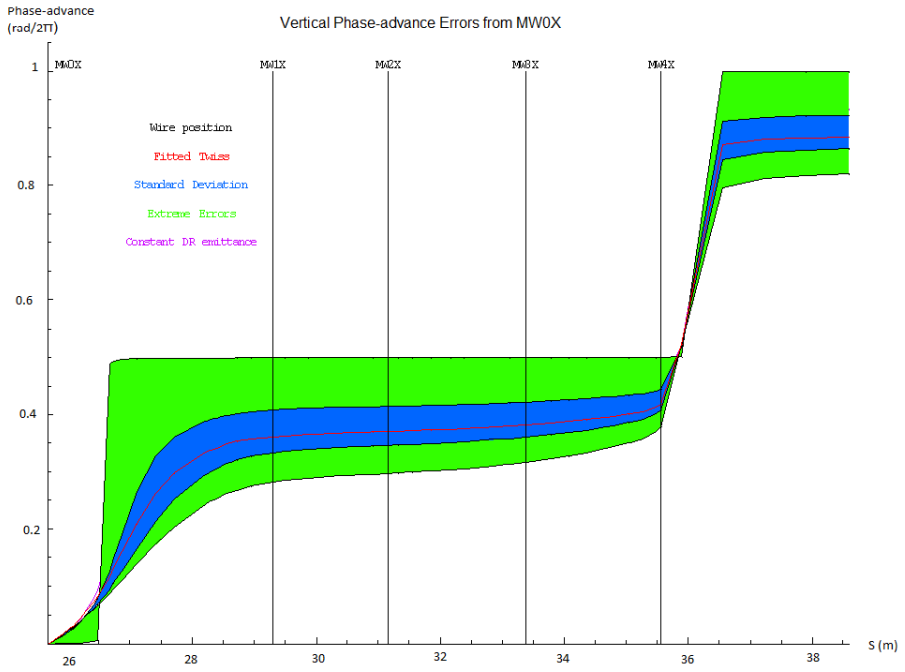

Figure 2.19: Phase advance between the wire-scanners taken from an instantaneous MAD deck that was generated from the ATF settings on 12th March 2008. The errors were generated by calculating the phase advance spread that resulted from the range of the beamsize measurement errors.

The new optics improved the phase advance between the wire-scanners, however the phase advance between the wire-scanners could not be accurately determined and was never ideal. This was considered a fatal problem for multi-wire measurements and the decision was made to use the OTR for the beamsize measurements. The OTR solved the two biggest problems that were associated with multi-wire measurements. The OTR gave instantaneous results and negated the need for extraction line correction procedures, this significantly reduced the time required for each measurement. The OTR was also not affected by the phase advance problems, as a result it was con-

cluded that the OTR was a better method for emittance measurements at ATF. The choice of the emittance computation method used is very important when attempting to accurately measure the emittance at ATF; this may be due to the assumptions made by each method and the phase advance on the real machine and in the simulations.

2.5.3 Results

The first full comparative test between each method of multi-wire emittance reconstruction was performed using the emittance growth results from 11th December 2007. The vertical beamsizes at 3 wire-scanners (MW0X, MW1X and MW3X) were recorded for no bump and for -0.9 mm vertical bump (Table 2.2). The emittance at MW0X was calculated from each beamsize source using my method (Table 2.3). The emittance values calculated from the ATF computed beamsizes using my method were compared to those calculated by Julien Brossard and the ATF SAD method (Fig. 2.17 and Fig. 2.20).

Table 2.2: A comparison of the vertical beamsizes at 3 wire-scanners when various data sources are used. The results for no bump and -0.9 mm bump are shown. The ATF values are the ATF computed beamsizes at each wire-scanner. The raw data values are the standard deviations of the Gaussian fits to the pre-manipulated wire-scanner data. The MAD values are the MAD computed beamsizes at each wire-scanner when a beam is tracked through the instantaneous MAD lattice.

Bump (mm)	**Wire-scanner**	**ATF (μm)**	**MAD (ATF value)**	**Raw data(ATF value)**
0.0	MW0X	52.2	1.02	1.10
0.0	MW1X	15.4	1.53	1.03
0.0	MW3X	90.8	1.71	1.46
-0.9	MW0X	35.0	1.51	1.14
-0.9	MW1X	19.1	1.21	0.98
-0.9	MW3X	79.4	1.94	1.42

The 19th December 2007 shifts involved measuring the beamsize at the XSR and OTR for a range of positive vertical bumps. The relative difference between the XSR and OTR beamsizes indicates a possible strong relationship between the bump value

Table 2.3: A comparison of the vertical emittance values computed using various beamsize data sources.

Data source	0.0mm bump (pm)	-0.9mm bump (pm)
SAD	52 + 84.1 - 51.8	47.4 + 58.6 - 9.3
MAD phase space	42.64	42.66
MAD wire-scanner simulation	56.16	43.61
ATF computed beamsizes	107.64 ± 7.28	40.29 ± 69.68
Beamsizes from raw data files	78.52	86.27

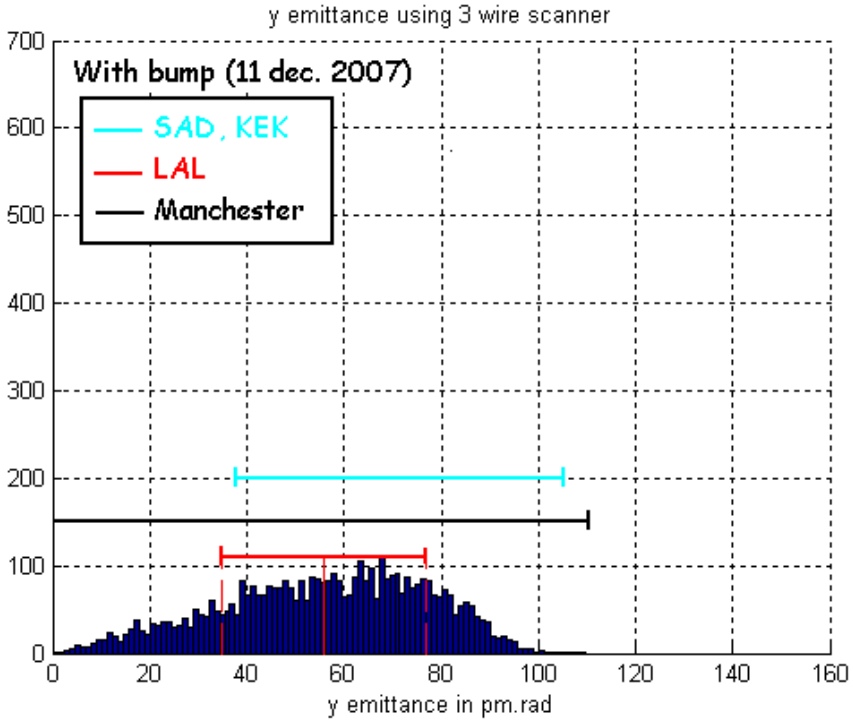

Figure 2.20: A comparison of the emittance ranges from each of the emittance reconstruction methods. These results were taken on 11th December 2007 when a -0.9 mm vertical bump was present.

and the emittance (Fig. 2.21). The relatively low expected dispersion levels at the OTR mean that the beamsize at the OTR should be dominated by the emittance-based beamsize (called the 'beta beamsize' due to its dependency on the Twiss parameters).

The 4th March 2008 shift attempted to reproduce that of 19th December 2007. The same range of bumps were each applied three non-consecutive times. For each bump

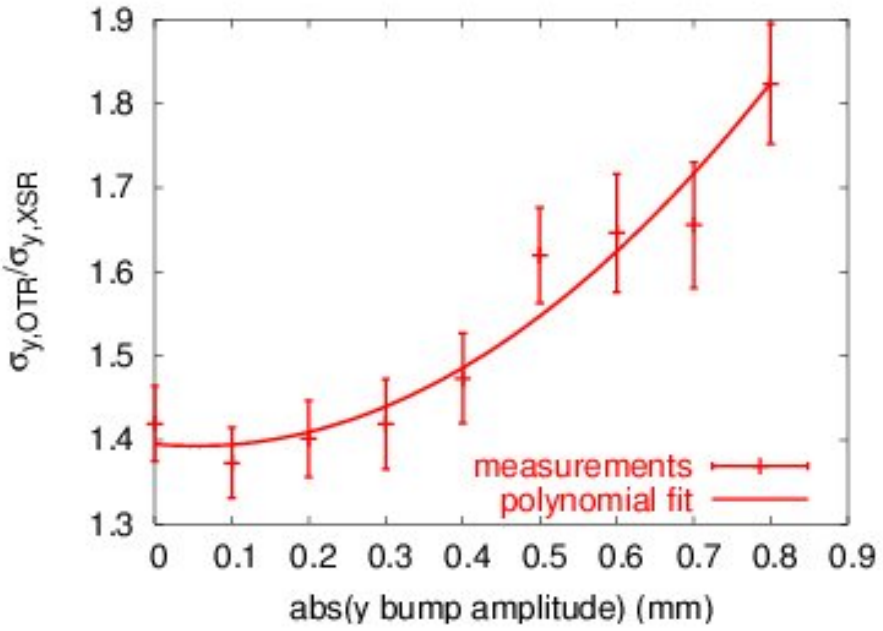

Figure 2.21: A plot of the OTR beamsize normalised with respect to the XSR beamsize for a range of positive vertical bump values. A sextupole field should give a polynomial relation (of order 2) between the bump size and the emittance.

the XSR and OTR vertical beamsizes were measured continuously for a roughly equal amount of time and the average beamsizes were plotted. The results do not suggest a relationship (Fig. 2.22).

During the 12th March 2008 shift another attempt at multi-wire measurements was made. No bumps were attempted during this shift but 4 wire-scanners were used for beamsize measurements. The vertical emittance calculated at MW0X by Julien Brossard and I was 72.63 pm·rad and 81 ± 26 pm·rad respectively. The error ranges of the vertical beamsize at each wire-scanner were used to propagate the beamsize along the ATF diagnostic section and to measure the phase advance through the same region (Fig. 2.23 and Fig. 2.19). The phase space at MW0X was plotted in such a way as to show where the phase space is being sampled for the emittance reconstruction (Fig. 2.24). The conclusion from these results was that the phase advance was inadequate for multi-wire measurements.

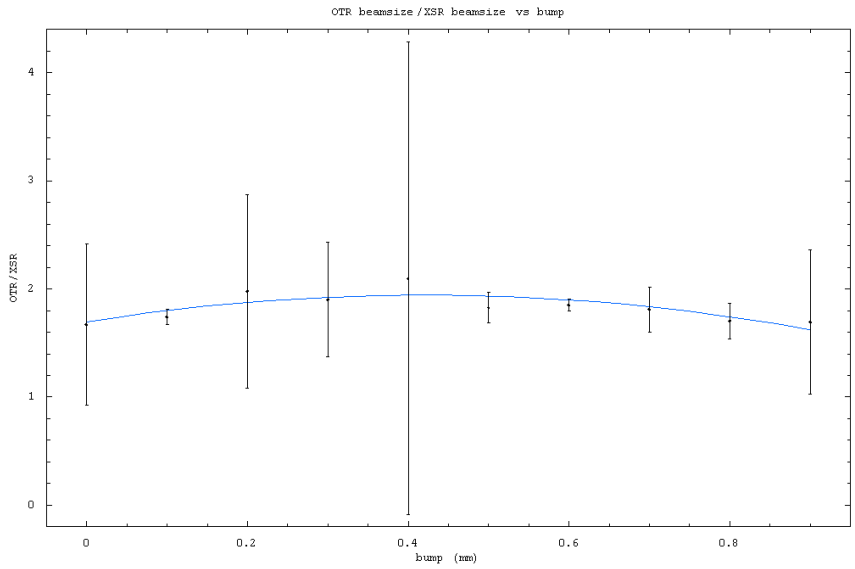

Figure 2.22: A plot of the time-averaged OTR beamsize normalised with respect to the time-averaged XSR beamsize for a range of positive vertical bump values. A sextupole field should give a polynomial relation (of order 2) between the bump size and the emittance. The polynomial fit should continually increase with distance if the QM7R non-linear field emittance growth theory is to be proven.

A Monte Carlo approach was taken in order to check the spread of the Twiss and emittance values that would match the 12th March 2008 beamsize measurements (Fig. 2.25). It was noticed that a sizable tail appeared on the beta function values. A 'cut-off' was applied to the beta function of 6 m, it was noticed that this removed the lower end of the emittance values (Fig. 2.26).

The 14th May 2008 shift involved measuring the XSR (Fig. 2.27) and OTR (Fig. 2.28) beamsizes for multiple bump values. The results show no strong correlation between the bump and relative beamsize growth.

The 22nd May 2008 shift involved measuring the XSR and OTR vertical beamsizes for the full range of possible bumps including negative bumps. There was no definitive evidence of any beamsize growth at the OTR (Fig. 2.29).

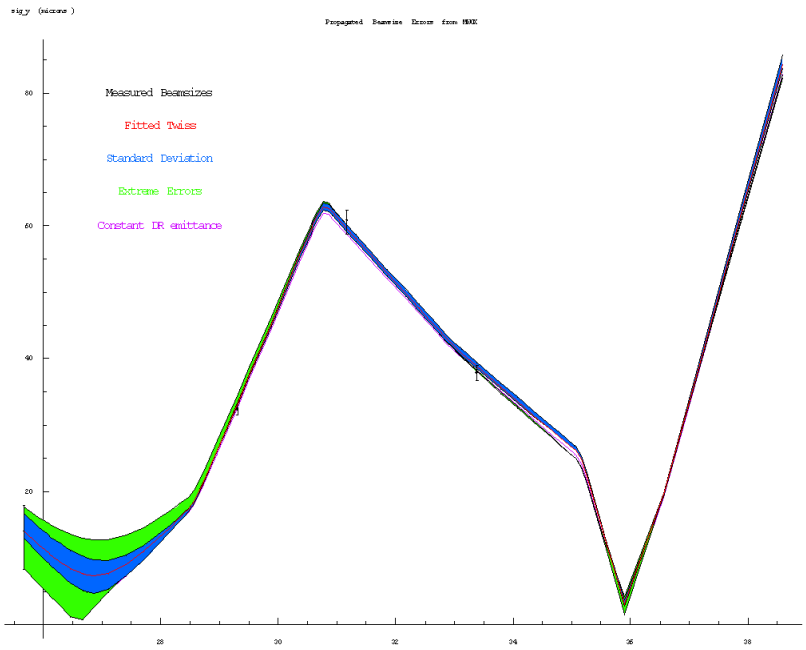

Figure 2.23: A plot showing the beamsize propagated along the ATF diagnostics section. The measurements were taken on 12th March 2008, the errors come from using the full error range of the beamsize measurements in the propagation of the beamsize.

The most complete set of results taken were from the 28th May 2008 shift. The beam positions at QM7R and the OTR were recorded, the tune was monitored, the beam current was recorded, the Twiss at the XSR and the extraction kicker were recorded, the beamsizes at the XSR and OTR were recorded and dispersion measurements were made. Bumps of -1.0 mm, -0.5 mm, 0.0 mm, 0.5 mm and 1.0 mm were applied. The emittance at the XSR and OTR were calculated and compared (Fig. 2.30). Polynomial were fitted for the maximum and minimum expected QM7R K_2L values using equation 2.4 (Fig. 2.31). There is a definite dependency between the bump in QM7R and the beta beamsize at the OTR, however it is less than the expected effects of the QM7R sextupole fields.

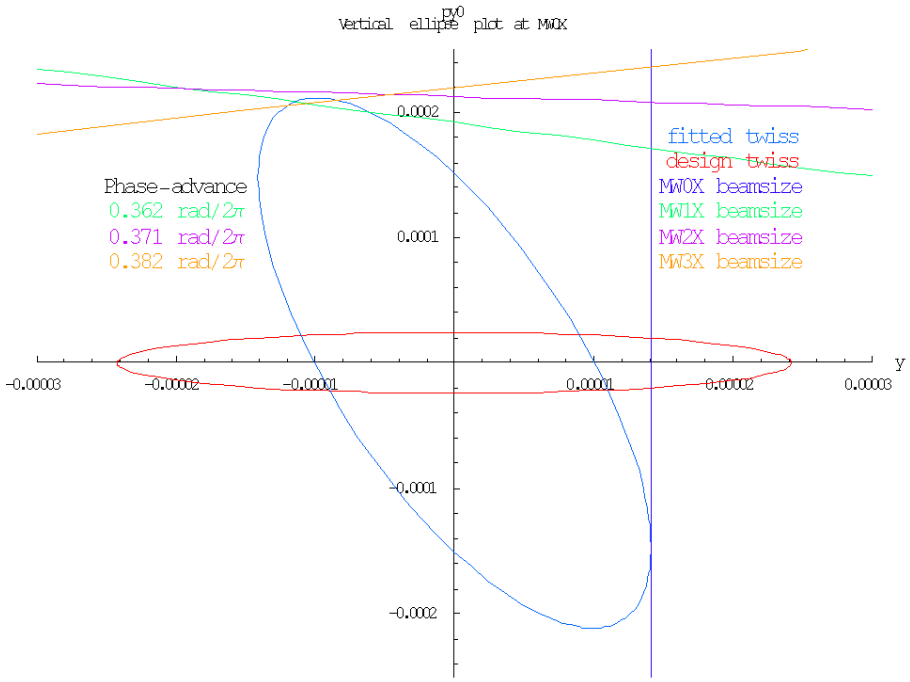

Figure 2.24: A reconstruction of the vertical phase space at MW0X, using real measurement data taken from 4 wire-scanners at ATF on 12th March 2008 and using response matrices generated from simulations using a MAD lattice generated from ATF magnet settings and measurements. The poor phase advance between wire-scanner leads to poor sampling of the phase space ellipse.

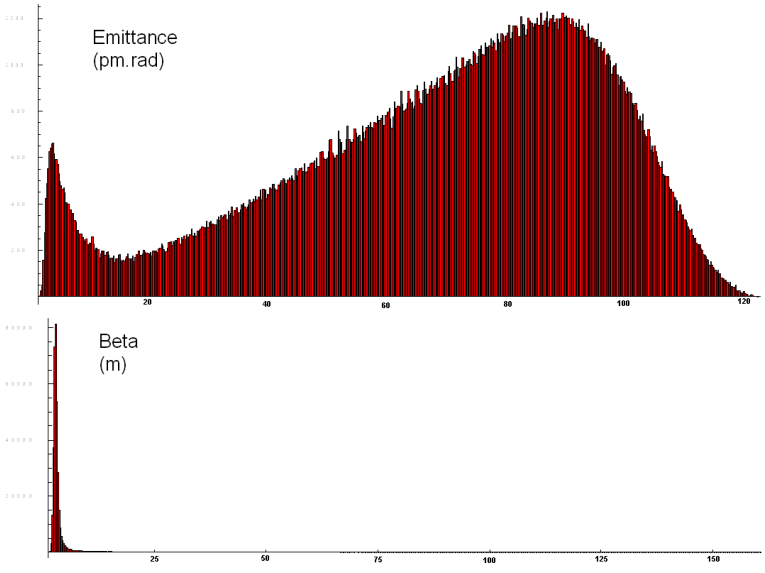

Figure 2.25: Histograms of the fitted vertical emittance and beta functions that are within the range of the errors in the beamsize measurements for the 12th March 2008 measurements.

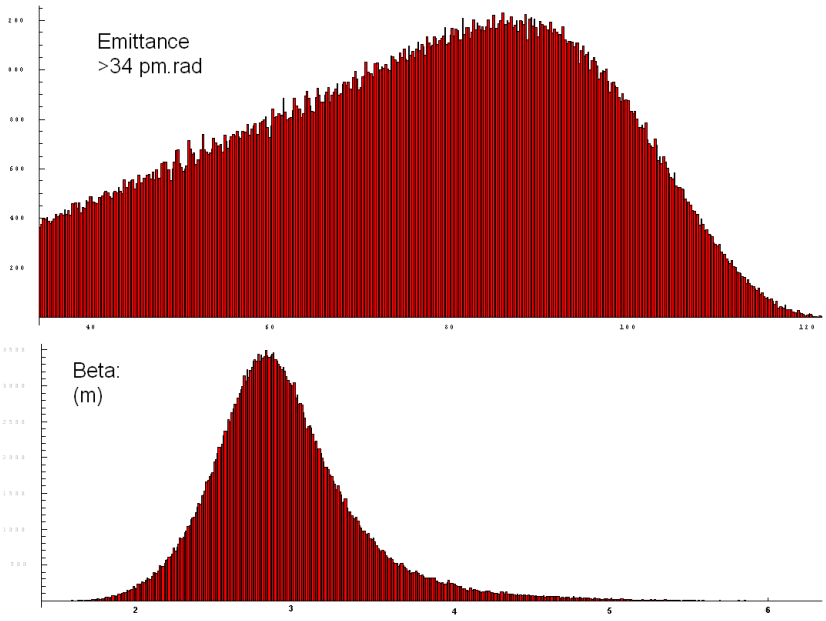

Figure 2.26: Histograms of the fitted vertical emittance and beta functions that are within the range of the errors in the beamsize measurements for the 12th March 2008 measurements. All solutions with a beta function above 6 m were ignored.

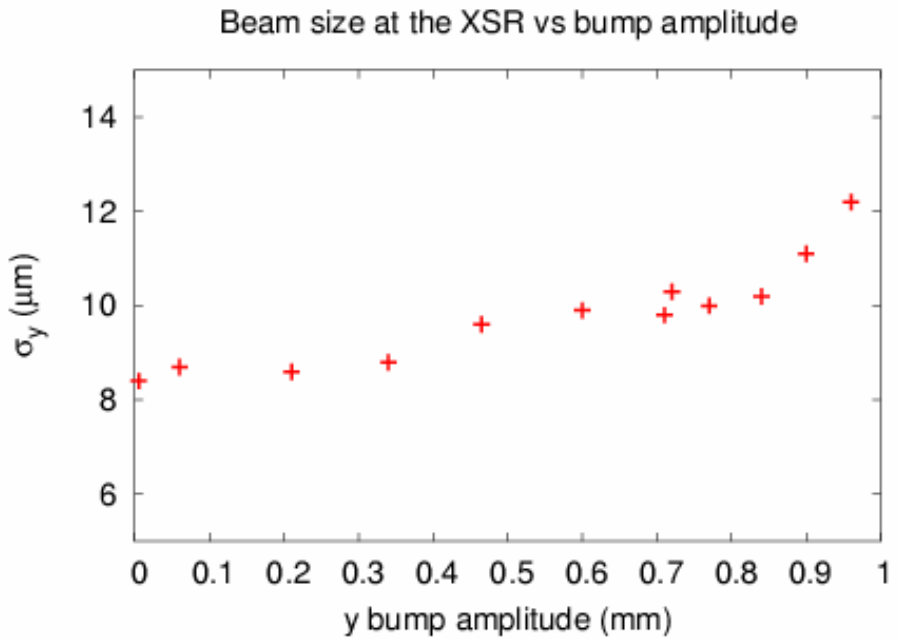

Figure 2.27: XSR vertical beamsize versus bump on 14th May 2008.

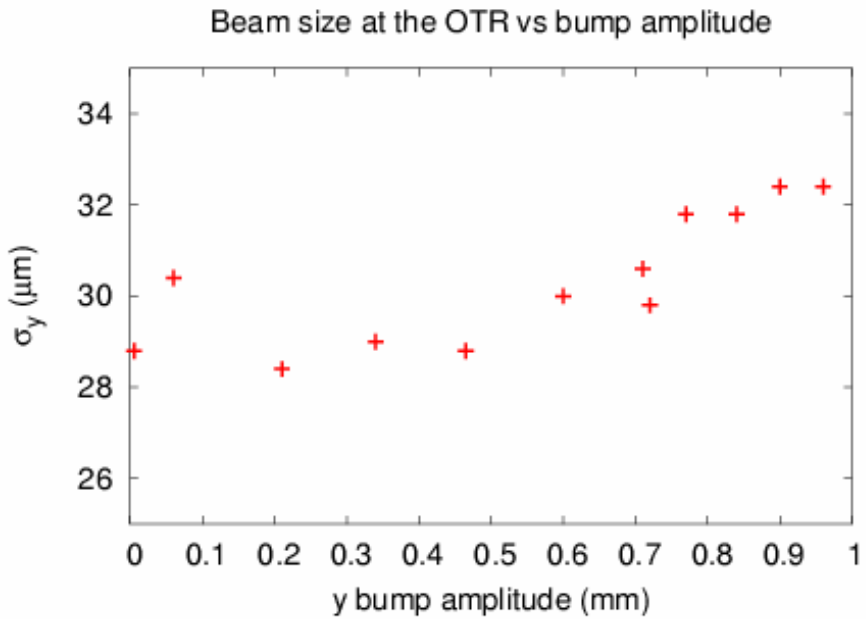

Figure 2.28: OTR vertical beamsize versus bump on 14th May 2008.

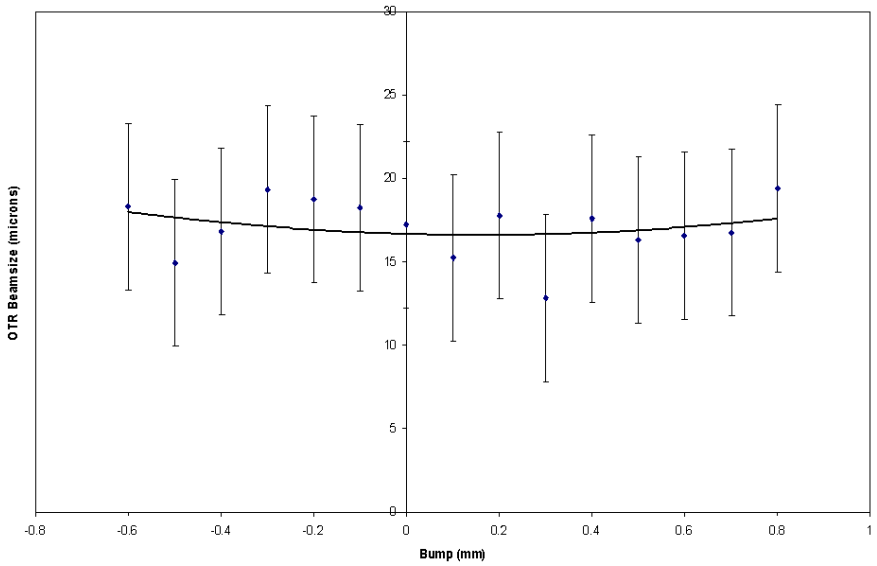

Figure 2.29: OTR vertical beamsize versus bump on 22th May 2008.

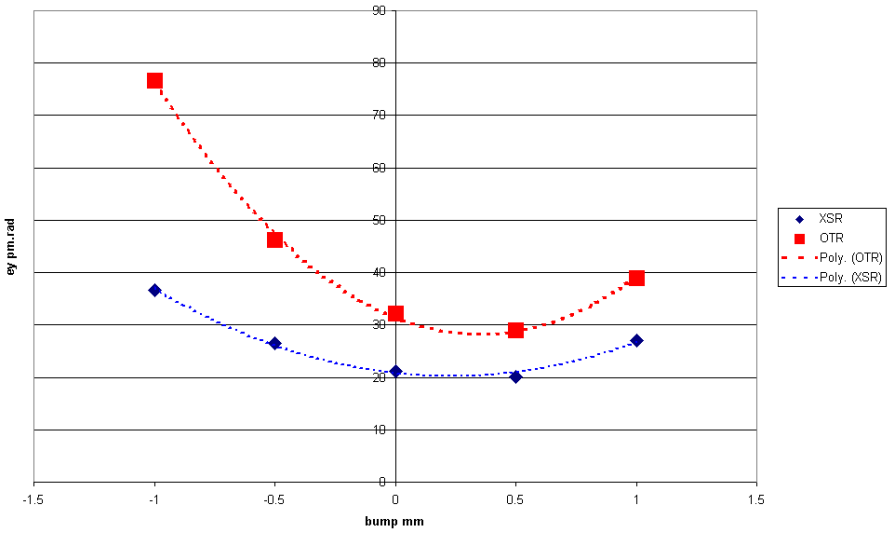

Figure 2.30: A comparison of the XSR and OTR vertical emittance versus bump on 28th May 2008.

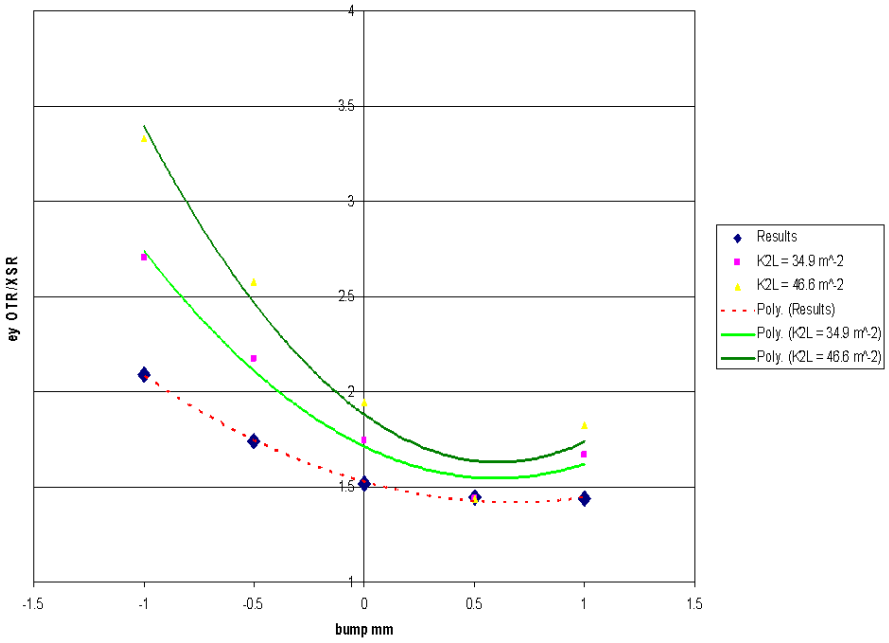

Figure 2.31: OTR vertical beamsize versus bump on 28th May 2008.

2.6 Conclusions

The multipoles experienced by the beam through QM7R as it is extracted were shown to be the primary candidate for the emittance growth but could not fully explain the results seen at ATF. Further extended simulation work using the multipoles of QM7R and the extraction septum magnets has managed to find a good agreement between the simulations and the measurements taken at ATF (Fig. 2.32 and Fig. 2.33). These results were calculated using equation 2.4 and the K_2L values of the extraction septums that have previously been calculated [10]. Either the expected horizontal beam off-set in QM7R is incorrect, or the extraction septums are helping to reduce the effects from the QM7R sextupole field. This is because the septum K_2L values are opposite to the K_2L of QM7R.

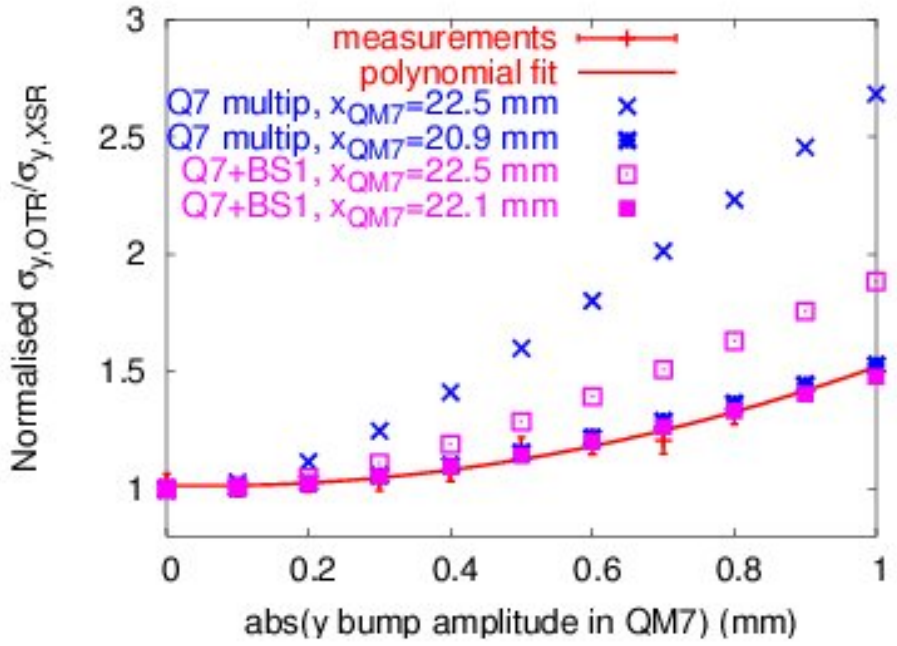

Figure 2.32: A comparison of the beamsize growth versus bump for the 19th December 2007 data and simulations using different magnet multipoles.

A solution to the emittance growth is to use a bigger bore quadrupole as a replacement for QM7R. A bigger bore magnet will cause the extraction beam to pass closer

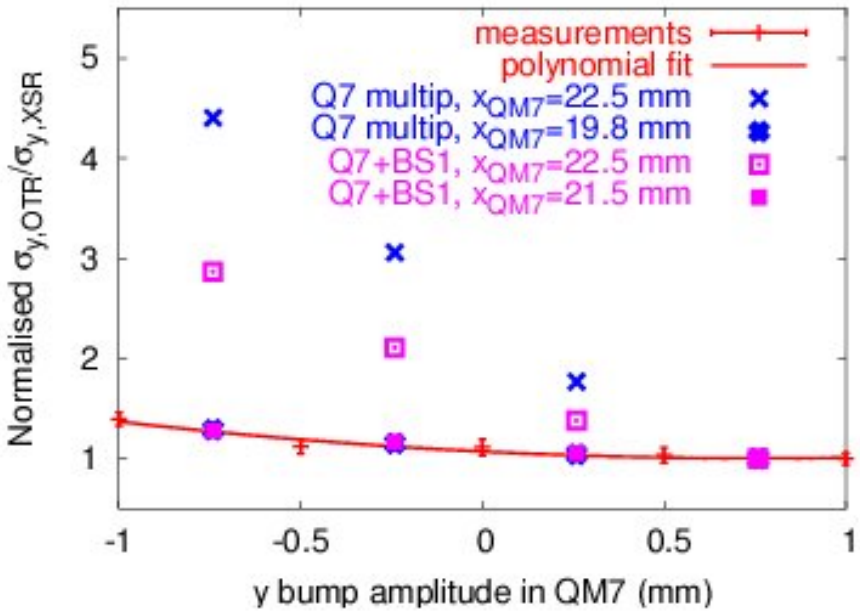

Figure 2.33: A comparison of the beamsize growth versus bump for the 28th May 2008 data and simulations using different magnet multipoles.

to the linear section of the magnet and experience lower levels of the magnet's multipoles. The magnet found for the replacement is called 'TOKIN 3581' and has a bore radius of 21 mm, which compares to the 22 mm beam position of the extracted beam and the 16 mm bore radius of the current QM7R. The K_2L values for the current QM7R magnet and the TOKIN 3581 magnet are 47 m^{-2} and 1 m^{-2} (Fig. 2.34). TOKIN 3581 has now replaced QM7R.

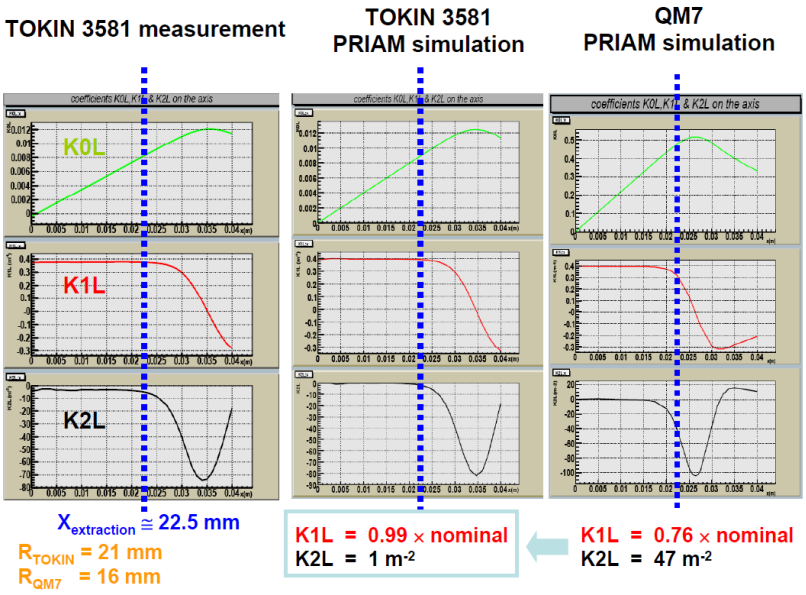

Figure 2.34: A comparison of the multipole mapping of QM7R and TOKIN 3581 using the simulation code PRIAM 2D [15].

3

Orbit Correction Optimisation for ATF2

3.1 Chapter Overview

For every accelerator an ideal reference orbit is defined and all the beam components are defined with respect to this orbit. Any deviation from this orbit may affect the characteristics of the beam and the goal of the accelerator. In a realistic accelerator, errors in the placement of accelerator components and orbit errors of the beam that is entering the accelerator can cause the beam orbit to not fit with the ideal orbit. One of the most important tools needed in the operation of an accelerator is a rugged orbit correction procedure. In this chapter several methods of orbit correction are investigated and optimised for use on ATF2. The best method is then compared to competing methods developed by other teams and an orbit correction program is created for ATF2.

In Section 2 of this chapter the theory of orbit correction is presented along with the different methods available for use on an accelerator while focusing primarily on ATF2.

In Section 3 details of the ATF2 extraction line and final focus and the orbit correction techniques available for ATF2 will be presented along with details of the development of the techniques and how they compare to each other in simulated test conditions.

In Section 4 details of the orbit correction algorithms developed by another research team are presented along with simulated and real-life comparative tests results between the orbit correction algorithms developed in Section 3 and those of the other research team. Simulated and real-life results showing that the stripline BPM intensity dependence had a significant effect on the extraction line orbit correction algorithms are also shown.

3.2 Introduction

3.2.1 Section Overview

In Part 2 of this section a general introduction to the concept of orbit correction is presented.

In Part 3 the mathematics of orbit correction is presented showing a simplified scenario.

In Part 4 the details of the most important types of orbit correction for this publication are presented with the mathematics that are most relevant for the rest of this chapter.

3.2.2 An Introduction to Orbit Correction

A problem that every accelerator suffers from is component misalignment. Component misalignment refers to situations where a magnet or a monitoring device is physically

out of its design position relative to the neighbouring components and the ideal orbit of the beam. A major source of component misalignment happens during the installation of the components. Typically a survey of the component positions is performed after any major installation work and realignments are performed where possible, however this will not eliminate all of the component misalignments. At ATF2 the typical range of post-survey magnet misalignments is of the order of a few tens of microns (Fig. 3.1 & Fig. 3.2). The ground on which the components are situated also suffers from continual vibrations called 'ground motion' that gradually leads to significant component misalignments which have to be periodically corrected for. The components also tend to have a discrepancy between their design orientation and their physical orientation. The most important orientation errors arise from situations where the component is rotationally misaligned around the path of the beam, this is known as a 'roll error' which results in sources of coupling. One further source of error is the result of differences between the design magnet strength and the magnet strength experienced by the beam. Direct correction of these errors is usually impractical, so these sources of error must be compensated for by making controlled changes to the orientation and/or strength of some of the magnets within the accelerator. One of the main techniques for compensating for component errors within an accelerator is known as 'orbit correction'. This process only compensates for component errors that result in alterations to the path of the beam.

The concept behind orbit correction is to alter the path of the beam in such a way as to reduce the undesirable effects of passing through a magnet off-centre. As a result the typical goal of orbit correction is to align the path of the beam with the centre of all the magnets. Such a goal is often impractical to achieve due to hardware constraints or the current conditions of the accelerator, which means that the orbit correction technique will result in a 'best fit' situation that leaves errors which must be corrected with other techniques.

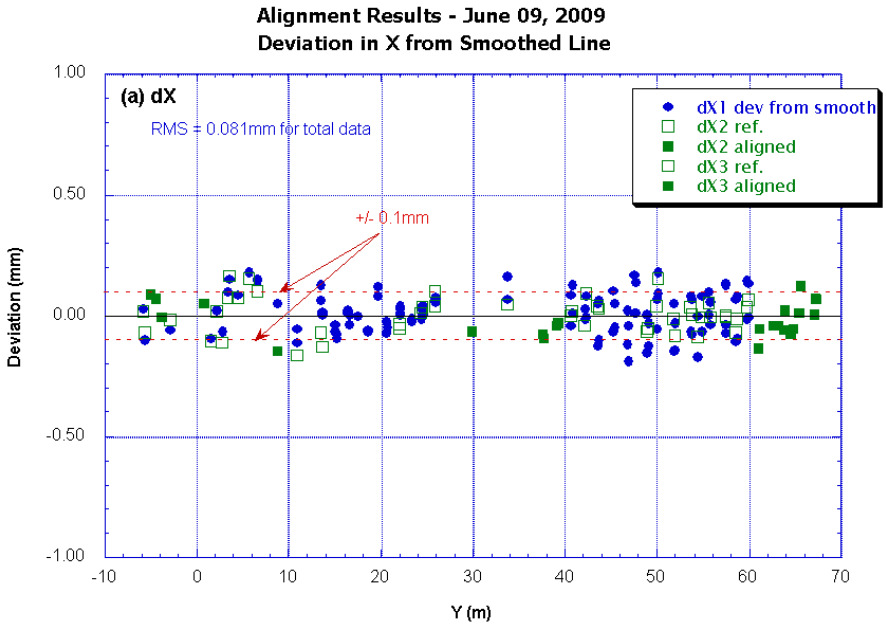

Figure 3.1: Horizontal ATF2 magnet centre offsets as of June 2009 [16].

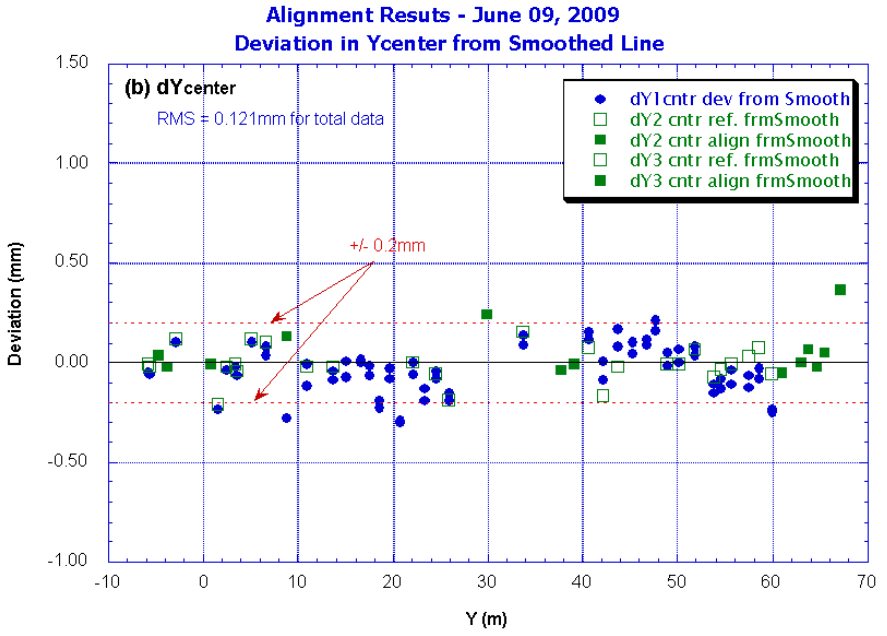

Figure 3.2: Vertical ATF2 magnet centre offsets as of June 2009 [16].

The position of the beam at a given point is measured by a beam position monitor (BPM). Hardware constraints typically result in the number and location of the BPMs differing from those of the magnets. This reduces how effectively the orbit correction technique can align the beam path with the magnet centres due to an inability to know the exact location of the beam with respect to the centre of the magnet. As a result the offset between a magnet and the next set of BPMs is measured in a process known as beam based alignment (BBA).

A horizontally focusing quadrupole will bend the path of the electrons within the beam towards the centre of the quadrupole in the horizontal plane. The further off-centre a particle is with respect to the quadrupole centre, the more the path is bent. If the centre of the beam passes through the centre of the quadrupole, there will be no change in the path of the beam. If the beam is greatly off-centre, the beam path will be drastically deflected toward the magnet centre. By creating local orbit bumps across a quadrupole (see previous chapter) and measuring the resultant change in orbit at nearby BPMs, it's possible to discover the offset between the quadrupole and BPM centres. If the quadrupole centre matches the centre of a given BPM and there are no other magnets between the quadrupole and the BPM, the beam will be focused towards the centre of the BPM. If the same quadrupole is offset horizontally by a distance, x, the centre of the beam at the BPM will be shifted by a distance of x, hence the quadrupole centre will be at the point of least orbit difference. This is how beam based alignment is performed at ATF2.

3.2.3 Simple Orbit Correction

Orbit correction traditionally involves the use of 'corrector' dipole magnets to 'kick' the path of the beam towards the desired positions on the BPMs, which is typically the BPM positions that are related to the quadrupole centres. This process has many similarities to the process for developing orbit bumps that has been discussed in the

previous chapter. In theoretical or computational situations the strength of a corrector is usually given in terms of the angle of deviation of the beam path from the nominal beam path as a result of the corrector's magnetic dipole field. In practice, the strength of a real corrector is measured in terms of the current supplied to the magnet. The effective kick of the corrector is linearly related to the current supplied to the corrector within the usual operating limits. It is desirable to have the orbit correction in each transverse plane be independent of the other. As a result most correctors are known as either horizontal correctors or vertical correctors.

The simplest example of orbit correction is a situation in which there is a horizontal corrector at position s_0, which produces a kick angle of θ, and a BPM at position s_1, which is a distance l after the corrector. The area between the corrector and BPM is devoid of other accelerator components except for a drift region (the beam pipe). The incoming beam is horizontally offset from the centre of the beam pipe by a distance x_0 and has no initial horizontal angle of motion, x_0'. The centre of the BPM is perfectly aligned with the centre of the beam pipe. Using trigonometry it can be shown that to make a change in the horizontal beam position of Δx, where $\Delta x = x_1 - x_0$, x_1 is the desired beam position at the BPM and l is the distance between the corrector and the BPM, a kick angle of

$$\theta = \arctan \frac{\Delta x}{l} \tag{3.1}$$

is needed.

If the value of x_0' is non-zero, the required kick from the corrector is $\Delta\theta$, where $\Delta\theta = \theta - x_0'$. In this situation the initial horizontal beam position at the BPM, x_a, is given by

$$x_a = l \cdot \tan x_0' + x_0 \tag{3.2}$$

So the desired change in the beam position at the BPM becomes $\Delta x = x_1 - x_a$ and

by rearranging equation 3.2 to solve for x_0, equation 3.1 is changed to (see Fig. 3.3)

$$\theta = \arctan \frac{\Delta x + l \cdot \tan x'_0}{l} \tag{3.3}$$

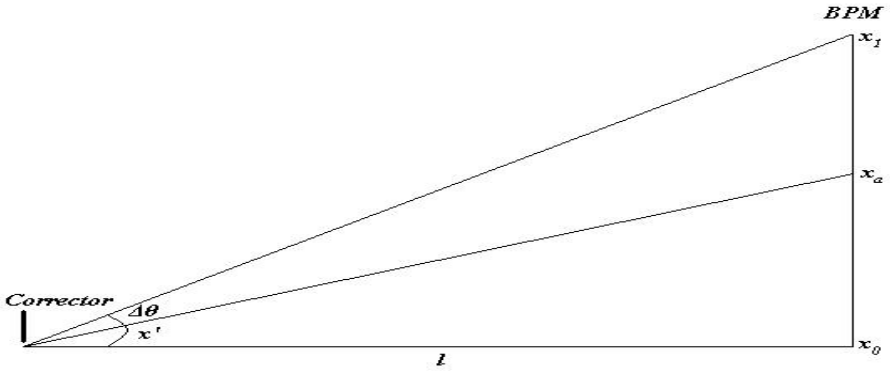

Figure 3.3: A plot demonstrating the relationship between the kick angle generated by a corrector and the resultant change in position at a downstream BPM.

It is unlikely that the area between the corrector and the BPM will be devoid of other magnets, so the effects of all the magnets between the corrector and BPM must be taken into account. This is reduced to a transfer matrix, **M**, that is treated as linear in most cases. If this is not true then coupling effects will cause interference between the horizontal and vertical orbit correction solutions.

The horizontal transfer matrix between two points (s_0 & $s_(1)$) is defined as

$$\mathbf{M_{0\rightarrow 1}} = \begin{pmatrix} R_{11} & R_{12} \\ R_{21} & R_{22} \end{pmatrix} \tag{3.4}$$

These transfer matrices are often referred to as R matrices. The position of the beam at the BPM, x_a, and angle of motion of the beam through the BPM, x'_a, before a correction is applied is given by

$$\begin{pmatrix} x_a \\ x'_a \end{pmatrix} = \begin{pmatrix} R_{11} & R_{12} \\ R_{21} & R_{22} \end{pmatrix} \cdot \begin{pmatrix} x_0 \\ x'_0 \end{pmatrix} \tag{3.5}$$

and the position, x_1, and angle of motion, x'_1, of the beam at the BPM before a correction is applied is given by

$$\begin{pmatrix} x_1 \\ x'_1 \end{pmatrix} = \begin{pmatrix} R_{11} & R_{12} \\ R_{21} & R_{22} \end{pmatrix} \cdot \begin{pmatrix} x_0 \\ x'_0 + \Delta\theta \end{pmatrix} \tag{3.6}$$

where $\Delta\theta$ is the kick generated by the corrector. In orbit correction the target angle at the BPM is typically not defined and is a free parameter due to the positions at the BPMs being the figures of merit that are to be corrected. As a result, by combining equations 3.5 and 3.6 and by considering only the positions at the BPM before and after correction, we find that

$$x_1 = x_a + R_{12} \cdot \Delta\theta \tag{3.7}$$

so if the term R_{12} is known, the required kick from the corrector can be calculated to give a correction of Δx at the BPM.

It should be noted that the horizontal and vertical planes may only be treated separately during orbit correction procedures as long as there are no significant sources of coupling between the horizontal and vertical planes and none of the applied corrections cause significant coupling between the two planes. If this is not true, it is necessary to take into account the vertical BPM readings and the R_{14} and R_{23} terms in equations such as equation 3.7.

3.2.4 Types of Orbit Correction

1-to-1

A typical accelerator has a number of correctors and a number of BPMs. All of the correctors are usually available for use in the orbit correction procedure. The simplest method for setting the strengths of all the correctors is to take each corrector in turn and

use it to correct the beam position at the nearest downstream BPM. This is known as '1-to-1' orbit correction because one corrector is used to correct one BPM. The method for setting the strength of each corrector is identical to the simple orbit correction examples discussed above. A more complicated variant is more commonly used in which one corrector is used to correct the beam position at multiple downstream BPMs. This variant results in one set of simultaneous equations similar to equation 3.7 per BPM. The set of simultaneous equations may not have a unique solution, as a result a best fit for the corrector strength is needed in order to minimise the total difference from the desired beam positions at each BPM. It may be desirable to weight the BPM readings so as to place more emphasis on the correction of the beam position at some of the BPMs.

Dispersion Free Steering

A common problem for accelerators is the beam dispersion. Dispersion is the name given to the phenomenon of altered particle orbits due to the particles possessing off-design momenta. The effects of dispersion are exacerbated by magnet errors and uncontrolled levels of dispersion lead to an increase in the beam size. Dispersion correction is similar to orbit correction, however instead of attempting to reduce the difference between the current orbit and the design orbit, dispersion correction attempts to alter the beam orbit in such a way as to minimise the levels of dispersion. Often dispersion is corrected after the orbit correction procedure has been applied, however both techniques tend to use the same correctors. As a result it is possible to try to correct the orbit and the dispersion at the same time. Such a procedure is called dispersion free steering. In dispersion free steering a set of equations similar to those found in orbit correction techniques are generated that predict the change in the dispersion at a given point due to a change in the strength of a corrector. This requires a good understanding of the transfer matrices between the corrector and the areas of dispersion that are to be corrected. The dispersion-change equations can be added to the list of

simultaneous equations given by the orbit correction procedures discussed above. The corrector strength is then set to a best fit so that the dispersion and orbit at given points downstream of the corrector are minimised with respect to their desired values.

Global

It is possible to set the strengths of all the correctors simultaneously by forming a set of simultaneous equations for every corrector-BPM combination. This is similar to the 1-to-1 situation in which each corrector was used to correct the beam position at multiple BPMs however in this situation all correctors are used to correct the beam position at all of the BPMs at the same time. The simultaneous equations are typically handled as a set of matrix multiplications. A response matrix, **R**, is formed, which contains all the relevant transfer matrix terms. For the global method equation 3.7 can be written as

$$\mathbf{\Delta x} = \mathbf{R} \cdot \mathbf{\Delta}\theta \tag{3.8}$$

where $\mathbf{\Delta x}$ is a matrix containing the resultant changes in the beam position at all BPMs and $\mathbf{\Delta}\theta$ is a matrix containing the changes made to the strengths of all the correctors. By rearranging equation 3.8, which requires the matrix inversion of the response matrix, it is possible to calculate a list of all of the corrector changes that are required to produce a given change to the path of the beam through all the BPMs. There are two methods for determining the response matrix terms. The transfer matrices between each corrector-BPM pair can be determined from the real machine or a simulated model of the machine. The $\mathbf{R_{12}}$ terms can then be collected together to form the response matrix. Alternatively the response matrix can be determined by applying a uniform strength change to all the correctors in turn and measuring the resultant change in the beam position at each BPM. This can also be done either on the real machine or a model of the real machine. The values given in $\mathbf{\Delta}\theta$ will be in units of the strength change applied to generate the response matrix.

If the number of correctors (N) is not equal to the number of BPMs (M) the response matrix becomes a M by N matrix and is non-square. Such a matrix has no definite inverse matrix. As a result is it necessary to use a pseudo-inversion technique on the response matrix, such as singular value decomposition (SVD) [17, 18]. SVD is widely used for global orbit correction techniques [19].

Given M BPMs and N correctors, SVD formalism defines the response matrix $\mathbf{R}$ as

$$\mathbf{R} = \mathbf{U} \cdot \mathbf{W} \cdot \mathbf{V}^{\mathbf{T}} \tag{3.9}$$

where $\mathbf{U}$ is an M by M unitary matrix, $\mathbf{V}$ is an N by N unitary matrix and $\mathbf{W}$ is an M by N matrix with non-negative values along the rectangular diagonal and zero values elsewhere.

From equations 3.8 and 3.9 and the unitary nature of $\mathbf{U}$ and $\mathbf{V}$ we have

$$\mathbf{\Delta x^t} = \mathbf{W} \cdot \mathbf{\Delta \theta^t} \tag{3.10}$$

where $\mathbf{\Delta x^t} = \mathbf{U^T} \cdot \mathbf{\Delta x}$, $\mathbf{\Delta \theta^t} = \mathbf{V^T} \cdot \mathbf{\Delta \theta}$ and $\mathbf{\Delta x^t}$ and $\mathbf{\Delta \theta^t}$ and the vectors in transformed BPM (t-BPM) space and transformed corrector (t-corrector) space, respectively. The matrix $\mathbf{W}$ is given by

$$\mathbf{W}_{ij} = w_{\min(ij)} \delta_{ij} \tag{3.11}$$

where the diagonal elements $w_n (\geq 0, 1 \leq n \leq \min(M, N))$ are the eigenvalues of the $\mathbf{W}$ matrix and represent the coupling efficiency between the t-BPMs and t-correctors.

If $\mathbf{\Delta x}$ is defined as the difference between the design orbit and the recorded orbit then $\mathbf{\Delta \theta}$ is the set of corrector strength changes required to achieve the design orbit; as

a result equation 3.8 can be rearranged to become

$$\mathbf{\Delta}\theta = \mathbf{R}_{inv} \cdot \mathbf{\Delta x} \tag{3.12}$$

where

$$\mathbf{R}_{inv} = \mathbf{V} \cdot \mathbf{W}_{inv} \cdot \mathbf{U}^{\mathbf{T}} \tag{3.13}$$

$\mathbf{W}_{inv}$ is a diagonal matrix of dimensions N by M and is given by

$$\mathbf{W}_{inv,ij} = q_{min(ij)}\delta_{ij} \tag{3.14}$$

where

$$q_n = \begin{cases} 0, & w_n \leq \varepsilon w_1 \\ 1/w_n, & otherwise \end{cases} \qquad (1 \leq n \leq min(M,N))$$

w_n is ordered by size in descending order, where by w_1 is the maximum value of w and $w_{min(M,N)}$ is the lowest value. ε is the singularity rejection parameter in the range [0,1]. This parameter is primarily determined by the requirements of the orbit correction technique. $q_n = 0$ corresponds to decoupled channels, which do not contribute to orbit correction.

When $\varepsilon = 0$ all eigenvalues are kept, theoretically this results in the most accurate orbit correction. When $\varepsilon = 1$, $\mathbf{R}_{inv}$ is a null matrix and there is no orbit correction. ε_m is the largest possible value of ε in order to retain all non-zero eigenvalues. Using ε_m or $\varepsilon = 0$ should result in the same $\mathbf{R}_{inv}$, however all values of ε greater than ε_m should result in different $\mathbf{R}_{inv}$.

The number of retained eigenvalues (n_{eigen}), where $0 \leq n_{eigen} \leq min(M,N)$, is related to ε by

$$\varepsilon = w_a/w_1 \qquad (where \quad a = n_{eigen}) \tag{3.15}$$

The outcome of this relation is that the number of retained eigenvalues is a se-

lectable parameter and will affect the orbit correction efficiency.

One final outcome of SVD formalism is an efficiency rating for each BPM and each corrector change, this is because certain instances of w_n have a limiting effect on the value of ε_m (Fig. 3.4). In physical terms this can be explained as a BPM position having a minimal reaction to most correctors or a corrector having minimal effect on most BPM readings. The efficiency indices of the BPMs and correctors are EB(i) and EC(i), respectively and are defined as

$$EB(i) = \sum_n w_n U_{in}^2 \qquad (1 \leq i \leq M) \tag{3.16}$$

$$EC(i) = \sum_n w_n V_{in}^2 \qquad (1 \leq i \leq N) \tag{3.17}$$

By removing low efficiency BPMs and correctors it is possible to maximise the value of ε_m and improve the quality of the orbit correction. As a result it is important to optimise the efficiency of any algorithm that uses the global orbit correction method by optimising the BPMs and correctors used as well as the number of eigenvalues retained.

3.3 ATF2 Orbit Correction Optimisation

3.3.1 Section Overview

In Part 2 of this section the details of how orbit correction is performed and optimised on the ATF2 final focus is presented. The method and results for the optimisation of the final focus orbit correction algorithms is also shown and tested in simulations.

In Part 3 the details of how orbit correction is performed and optimised on the ATF2 extraction line is presented. The method and results for the optimisation of the final focus orbit correction algorithms is also shown and tested in simulations.

In Part 4 the details of all 4 of the sets of orbit correction algorithms developed for

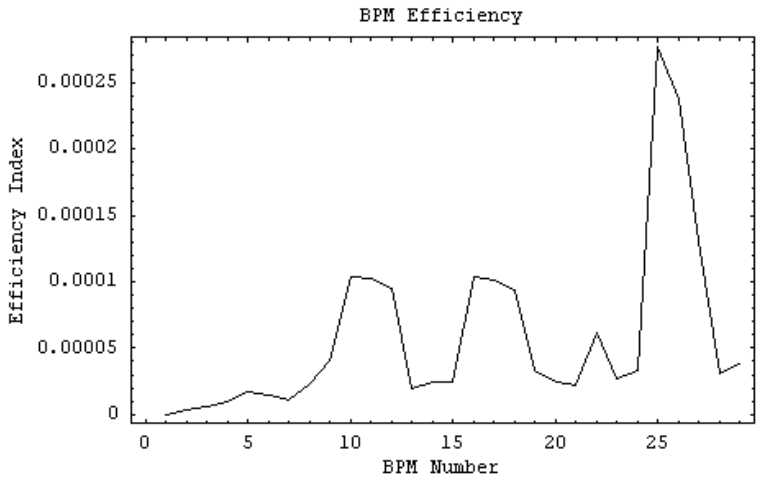

Figure 3.4: An evaluation of the orbit correcting efficiency of the ATF2 final focus BPMs resulting from the SVD formalism. Arbitrary units are used. The horizontal axis starts with value 1 being the first BPM in the extraction line and increasing for each BPM along the length of the beam line.

this publication are presented.

In Part 5 the comparison of the orbit correction algorithms discussed are presented.

3.3.2 Final Focus Section

The ATF2 extraction line uses the traditional method of correcting the orbit via the use of corrector magnets, however the ATF2 final focus section uses a non-traditional method of orbit correction. The final focus system does not use corrector magnets for orbit correction, instead all of the 22 quadrupoles are on magnet movers. These movers can alter the horizontal and vertical position of the magnet attached to the mover, as well as changing the amount of roll that the magnet has which gives each quadrupole 3 degrees of freedom. When a beam passes off-centre through a quadrupole a dipole field is experienced by the beam, which creates a corrector-like kick. The scale of this kick is related to how far off-centre the beam passes. If L is the length of the quadrupole, k_1 is the strength of the quadrupole field component of the quadrupole and Δx is the beam offset from the centre of the quadrupole, the kick angle θ experienced by the beam is

given by

$$\theta = k_1 L \Delta x \tag{3.18}$$

As a result a quadrupole may be used in the same manner as a corrector by changing the the position of the quadrupole. Since each quadrupole in the final focus can be moved in the horizontal and vertical plane, each quadrupole can be used for both horizontal and vertical orbit corrections. The basic principles are still the same in both the corrector-based and mover-based orbit correction methods and the effects of an offset quadrupole can theoretically be replicated by placing a corrector at the exit of the quadrupole and setting the strength to give the same kick that would be produced by the quadrupole offset. The mover-based method was chosen because it does not require the use of corrector magnets and should produce finer granularity kicks than correctors can. This is due to the minimum magnet mover step size producing a smaller kick differential than can be produced by the minimum current change in the correctors. Correctors rely on a digital-to-analogue (DAC) converter to convert the computer-chosen digital current values in to the 'real world' analogue current settings used on the magnet power supplies. The minimum current step of the correctors is given by $(I_{max} - I_{min})/(2^{\text{bits}} - 1)$, where I is the current and bits is the bit resolution of the DAC. The DACs used in the ATF2 extraction line correctors have a bit resolution of 11 bits. The current step equation results in an inverse relationship between the accuracy and range of the correctors. The use of magnet movers should allow for greater orbit correction precision because the magnets are moved using motors which have an inherent step size limitation that is unrelated to the range limitation of the motors. The ability to roll the quadrupole magnets should also allow for alterations to the levels of coupling along the beamline. As part of the work performed in this report the magnet mover-based method of orbit correction was optimised and compared for use on the ATF2 final focus using simulations performed by the DIMAD particle tracking program [33].

Orbit Correction Optimisation

The choices that govern the efficiency of the orbit correction set-up are:

- the number of magnet movers (N) that will be used;
- the number of BPM readings (M) that will be used;
- the number of eigenvalues (n_{eigen}) that will be retained.

The three choices listed above are referred to as the 'knobs' of the orbit correction method and are the values that are to be optimised. Although there are limits on the available options for the knobs, many of the options available are inherently worse than the other available options and would only result in increasing the CPU time needed to achieve optimisation. As a result many options can be ignored. For the BPM and number of magnet movers knobs only the most inefficient BPMs and magnet movers should be considered for exclusion. The limitations on how many BPMs and magnet movers should be considered for exclusion will be governed by CPU-time limitations, hence a greater amount of CPU-time may lead to a more optimum orbit correction set-up, however this may not always be the case. For the eigenvalues knob it has already been stated in the SVD formalism that a higher number of eigenvalues should theoretically lead to a better orbit correction set-up, hence only the highest values of n_{eigen} should be considered, however if the limitation applied on the knob is too constricting then a more optimum orbit correction set-up may be missed.

A systematic approach to the options chosen for each knob was taken for the optimisation of the final focus orbit correction method so that all possibly good orbit correction set-ups could be investigated. To do this it was necessary to create an arbitrarily tiered system for the knobs, which allowed for a lower tiered knob to cycle through its possible options each time a higher tiered knob was set to a different option.

A measure of the efficiency of an orbit correction set-up was chosen. This figure of merit was chosen in such a way as to take into account the amount of orbit perturbation reduction achieved by an orbit correction set-up. It was chosen that the orbit perturbation in each direction of motion would be calculated as the root-mean-square of all the BPM readings in the corresponding direction of motion. It was also agreed that the vertical (Y) orbit correction would be given higher weighting than the horizontal (X) orbit correction when calculating the figure of merit, as the beam at ATF2 is of the order of 100 times smaller in Y than it is in X. The optimum orbit correction set-up results in the biggest fractional decrease in the orbit perturbation. As a result the figure of merit (FoM) is defined as $X_{f,rms}/X_{0,rms} + 2Y_{f,rms}/Y_{0,rms}$ where X_f and Y_f are the corrected orbits and X_0 and Y_0 are the original orbits. The vertical orbit has been given a factor of two weighting in order to emphasise the need for a flat orbit in the vertical plane, so as to reduce the amount of vertical beamsize growth generated by non-linear fields. This is because the target horizontal beamsize is a factor of about 100 times greater than the target vertical beamsize but both the horizontal and vertical orbit must be corrected. If the weighting factor is set to 1 then there is no emphasis on the vertical plane, while higher weighting factors will lead to lower levels of horizontal orbit correction.

The optimum orbit correction set-up should also work well under many different starting conditions, hence it is necessary to average the figure of merit for each orbit correction set-up over a sequence of errors. The errors were seeded so that the same errors could be applied to each orbit correction set-up. The number of seeds used was governed by the amount of CPU-time available but more seeds will reduce the amount of statistical error in the figure of merit. The relevant ATF2 errors used in the simulations were the officially expected errors for ATF2 [20]. All the errors were given a Gaussian distribution and a seeded random value for each error was calculated from the distribution. Some of the errors were static errors and were reseeded once a full bunch train had been tracked. Some of the errors were dynamic errors and were reseeded

for every bunch. Static errors are those that remain constant between bunches, such as component misalignments and power supply offsets. Dynamic errors are sources of error that change in magnitude over time scales that are consistent with the time scales between particle bunches or bunch trains, such as the component misalignment caused by the motion of the ground or other sources of vibration and fluctuations in the current supplied to the components. In the optimisation simulations, 5 bunch trains were tracked for each set-up with 5 bunches per train. In total 25 different sets of errors were tracked for each orbit correction set-up.

The ATF2 v3.8 lattice (See Fig. 1.4 and Fig. 1.5) was generated before a full set of magnet movers could be acquired, however a full set was eventually acquired and in anticipation of the acquirement of these extra 3 magnet movers a modified lattice was used in the simulations shown below that assumed all of the final focus quadrupoles were on magnet movers. The efficiency of the quadrupoles for use in the magnet mover-based orbit correction of the ATF2 final focus are shown in Figure 3.5.

The response matrices will have a diagonal structure but the first BPM will be unresponsive to all of the magnet movers due to all of the quadrupoles being downstream of the first BPM. It must also be noted that the 6th quadrupole, called QM11FF, has no effect on any of the BPMs due to QM11FF being set to have zero current supplied to it in the design optics of the final focus. As a result all optimisation settings tried assumed that quadrupole 6 (QM11FF) was not used.

In order to achieve the highest figure of merit during the orbit correction procedure the following settings were used:

- BPMs 1 and 4 were not used;
- quadrupoles 6 and 19 were not used;
- 20 eigenvalues were retained for use in the SVD process (this is the maximum

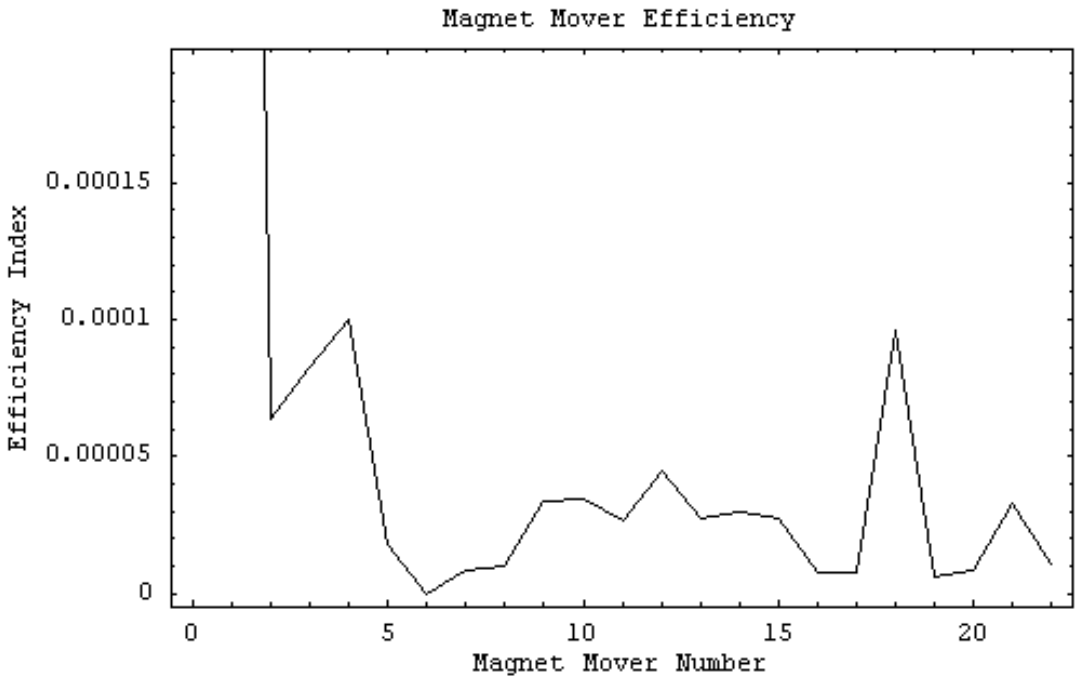

Figure 3.5: An evaluation of the orbit correcting efficiency of the ATF2 final focus magnet movers resulting from the SVD formalism. Arbitrary units are used. The horizontal values start with value 1 being the first quadrupole magnet mover in the final focus and following the quadrupole magnet movers in sequence along the beam line.

permissible value).

This resulted in an average orbit reduction of 90.5% in the horizontal plane and 94.1% in the vertical plane.

Horizontal and Vertical Orbit Correction Comparison

A simulation was performed in which a full range of errors were applied to a simulation of the final focus section of ATF2. The optimised settings shown above were used to correct the horizontal (Fig. 3.6) and vertical (Fig. 3.7) orbits. The orbit corrections are imperfect, which results in residual orbit perturbations. Subsequent iterations of orbit correction can further improve the orbit, however complete correction is improbable due to the limitations caused by the BPM resolution and magnet mover step size.

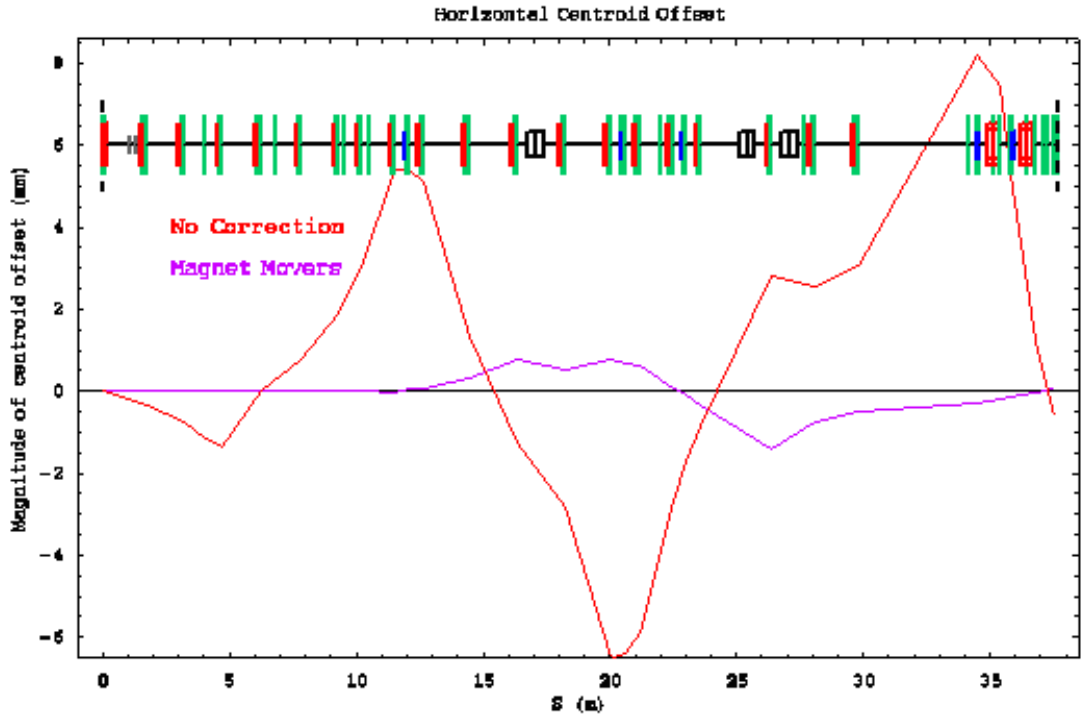

Figure 3.6: The horizontal beam orbit along the final focus section of ATF2 before and after the application of the optimised magnet mover based orbit correction method when a full range of errors has been applied. The value of S starts at the beginning of the final focus.

Post-optimisation Analysis

With the optimisation of the orbit correction method complete, tests were performed to gauge the effectiveness of the orbit correction method. The tests were focused on the vertical plane, as this is the direction with the tightest performance targets and the plane of most importance in later tuning and alignment phases for the preparation of ATF2 for ultra-low emittance beam preservation.

To achieve the goals of ATF2 it is necessary to not only have the orbit as close to the design orbit as possible but also to have an exceptionally low IP beamsize. The post-orbit correction phases of the tuning and alignment process have the responsi-

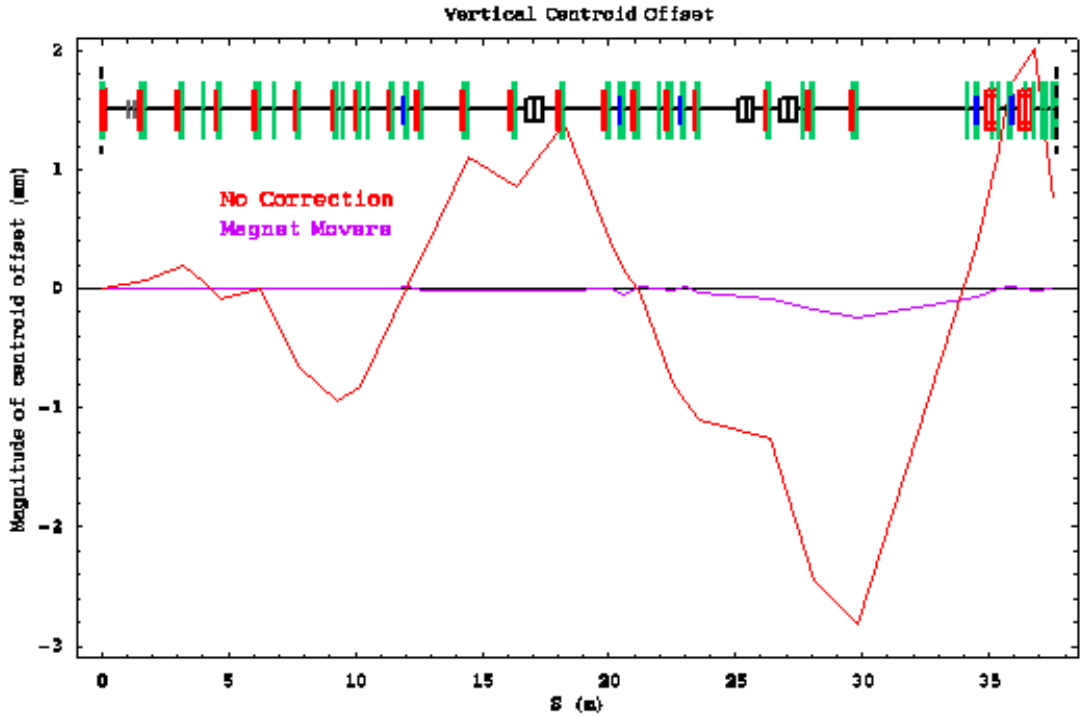

Figure 3.7: The vertical beam orbit along the final focus section of ATF2 before and after the application of the optimised magnet mover based orbit correction method when a full range of errors has been applied. The value of S starts at the beginning of the final focus.

bility of reducing the IP beamsize to the required levels, however the orbit correction set-up should not exacerbate the IP beamsize growth that results from the machine errors present. It is therefore necessary to measure the effect the orbit correction set-up has on the IP beamsize. The 'horizontal and vertical beamsize changes' test was designed to measure the horizontal and vertical IP beamsizes before and after orbit correction was performed when a selection of errors were applied. To do this it was necessary to track a beam of 5000 particles along the simulated beamline, calculate the IP beamsizes, perform the orbit correction procedure, re-track the same beam through the orbit-corrected beamline and calculate the new IP beamsizes. This was performed over several seeded errors. The number of particles used in the tracked beam and the number of seeds used was limited by the amount of CPU-time available. This test was performed for 100 seeds of errors.

It was found that the orbit correction procedure did not always reduce the IP beamsize growth caused by the orbit perturbations. The average post-correction IP beamsize growth in the vertical plane ($\sim$ 92 sigma) is much higher than the average value for the horizontal plane ($\sim$ 7 sigma) due largely to the relative difference in the nominal sigmas (2.82 microns horizontally, 36.81 nm vertically). These results indicate that the corrected orbit may not always be the ideal orbit for ATF2's low IP beamsize goals, however the IP beamsize tuning methods created for ATF2 are expected to be able to deal with such orders of magnitude of IP beamsize growth.

Algorithm Performance Tests

The generation of the response matrix for the magnet mover based orbit correction method was made using a simulated lattice devoid of errors. The errors on the real machine may alter the responses between some mover-BPM pairs, which may impact the effectiveness of the optimised magnet mover based orbit correction method and give rise to an imperfect orbit correction of the real machine. As a result the orbit correction method was tested with errors applied during the response matrix calculation section to determine the impact such errors would have on the orbit correction procedure. Misalignments were not applied at this stage because the response matrix measures the relative change in orbit caused by each magnet mover movement. This means that the orbit generated by the misalignments is the reference orbit from which the response matrix is generated and can be considered to be zero without impacting significantly on the response matrix.

The magnet movers have been treated as perfect in previous simulations. This is not the case on the real machine. As a result the effects of initial mover position errors and mover step-size limitations were also investigated.
Initial magnet mover position error: 1 micron

Mover step-size limitation: 300 nm

Additional error sources were added to the optimised magnet movers method of orbit correction. These errors were included to give a more accurate simulation of how the orbit correction procedure would perform on the real machine. On the real machine the response matrices can be generated experimentally by moving each magnet mover in turn and measuring the change in the orbit. In such a case the response matrices must be robust enough to be applicable when under the influence of the errors that are expected on the real machine. The BPM and magnet strength errors were included in the simulations that were used to generate the response matrices. The errors associated with the magnet movers were also included and the effects on the orbit correction process were compared (Table. 3.1).

Table 3.1: Orbit Corrected Efficiency Comparison.

Additional Error Source	**Horizontal FoM**	**Vertical FoM**
None	0.132	0.088
R-matrix BPM offsets	0.130	0.100
R-matrix BPM resolution	0.132	0.092
R-matrix magnet strengths	0.132	0.088
Mover step-sizes	0.132	0.088
Initial mover positions	0.131	0.088

It is possible to test the relationship between the orbit correction efficiency and the magnitude of the errors used. It is also possible to test the relationship between IP beamsize and the magnitude of the errors used. The magnitude of each error was varied and the orbit correction figures of merit (Fig. 3.8) and the IP beamsize growth values (Fig. 3.9) were averaged over 20 seeds for each magnitude of each error.

The magnet strength errors dominate the IP beamsize growth but have a minor impact on the orbit correction efficiency. As has been shown previously the sextupole

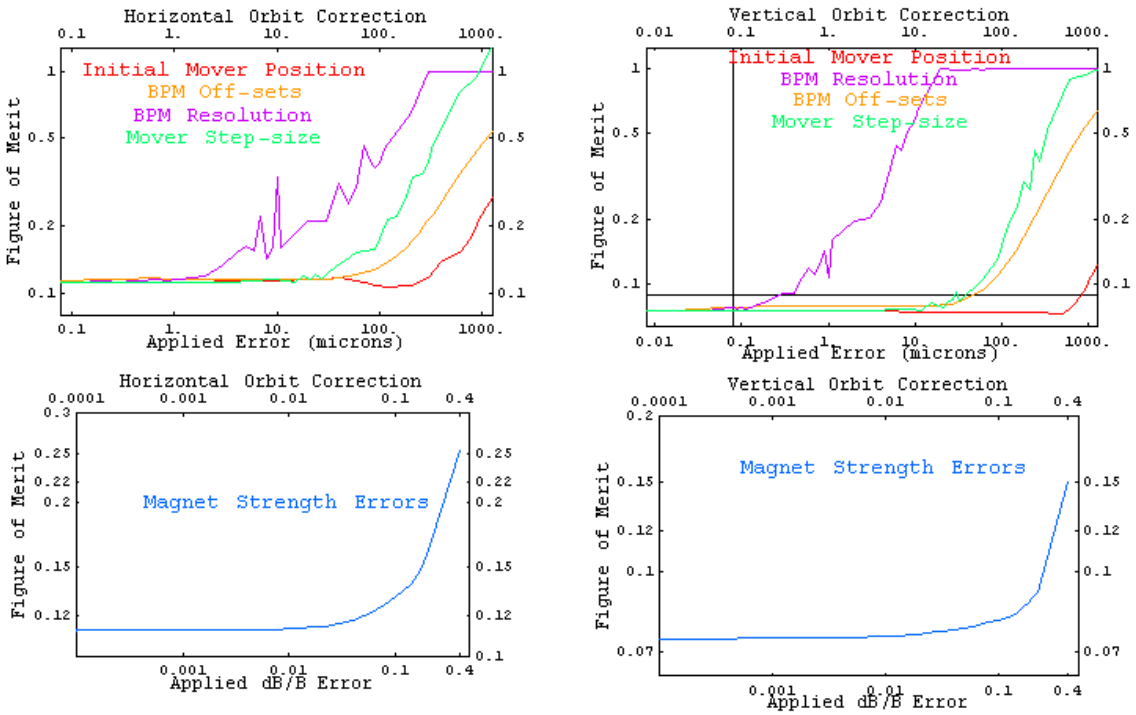

Figure 3.8: Correlation plots between various error magnitudes and orbit correction efficiency

component of a magnet can lead to a strong correlation between magnet strength errors and IP beamsizes with the sextupole magnets having the greatest effect on the beamsize. The initial mover position and BPM offset errors both appear as extra orbit perturbations when the initial orbit is analysed, however the initial mover positions cause actual orbit perturbation and at large error magnitudes can dominate the ordinary magnet misalignments while remaining insignificant at small error magnitudes. The BPM resolution and mover step-size control the efficiency of the orbit correction procedure. At small magnitudes both errors do not dominate the procedure and the orbit is corrected to the smallest orbit possible within one iteration of orbit correction. At large magnitudes the BPM resolution and mover step-size make it impossible for the orbit correction procedure to work. If the resolution is too high the BPM readings are meaningless. If the step-size is too large the magnet cannot move to the required location and the orbit correction fails.

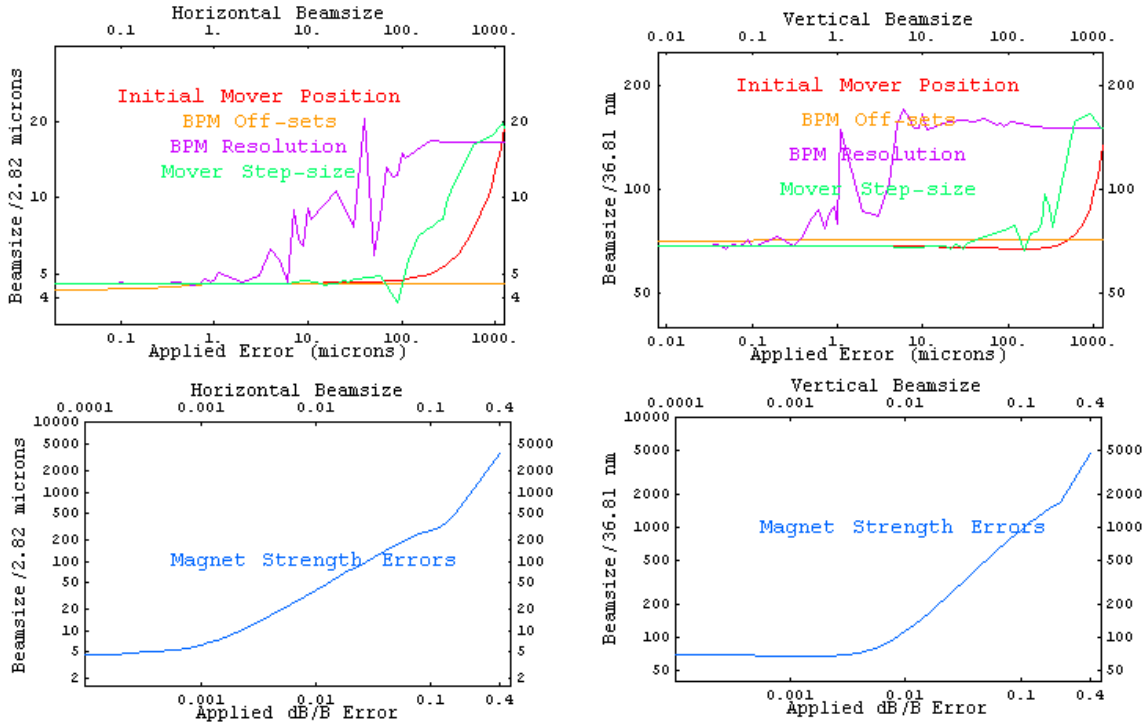

Figure 3.9: Correlation plots between various error magnitudes and IP beamsizes.

Conclusion

The magnet mover system has been shown to be an effective means of controlling the orbit through the ATF2 final focus. The optimised global orbit correction methods shown above can achieve significant orbit correction within one iteration of the procedure. A truly flat orbit is impossible to achieve due to hardware limitations.

3.3.3 Extraction Line Section

The global orbit correction method was optimised for use with the extraction line section of ATF2. The extraction line uses a set of horizontal and vertical correctors placed along the length of the extraction line. In addition to this the horizontal bending magnets used for extracting the beam from the damping ring and steering the beam along the beam line were enhanced with the addition of 'trim windings'. The trim windings are additional coils placed around the exit of the bending magnets in order to allow for the magnetic field upon exit of the bending magnet to be changed. These allow for the possibility of controlling the path of the beam as it exits the bending magnet. These can be treated as extra horizontal correctors during the orbit correction procedure. In v3.8 of the ATF2 extraction line lattice, there were effectively 16 horizontal correctors and 11 vertical correctors. The vertical response matrix demonstrates the ideal diagonal response expected from a good response matrix, however the horizontal response matrix does not clearly show this due to the first correctors having very large responses to all BPM, which overshadows the downstream corrector-BPM pair responses.

The method used for the optimisation of the extraction line orbit correction procedure was very similar to that used for the optimisation of the final focus orbit correction procedure. Since the number of retained eigenvalues for the horizontal and vertical planes had differing maximum values, they were set independently of each other. The number of retained eigenvalues was also optimised before the optimisation of the BPMs and correctors in order to limit the number of optimisation scenarios to be considered. The optimised number of horizontally and vertically retained eigenvalues was determined to be 12 and 8 respectively. The optimised settings resulted in an average orbit reduction of 53.9% in the horizontal plane and 47.7% in the vertical plane.

A short-list of possible low-efficiency correctors (Fig. 3.10) and BPMs (Fig. 3.11) was made. Every possible combination of BPMs and correctors from the short-list

was considered for removal from the orbit correction procedure. Each scenario was tested for 25 unique seeds of full errors. It was found that the 16th horizontal corrector (ZH10X) and the 6th BPM (MQF6X) are the most detrimental to the orbit correction efficiency and should be removed from the orbit correction procedure.

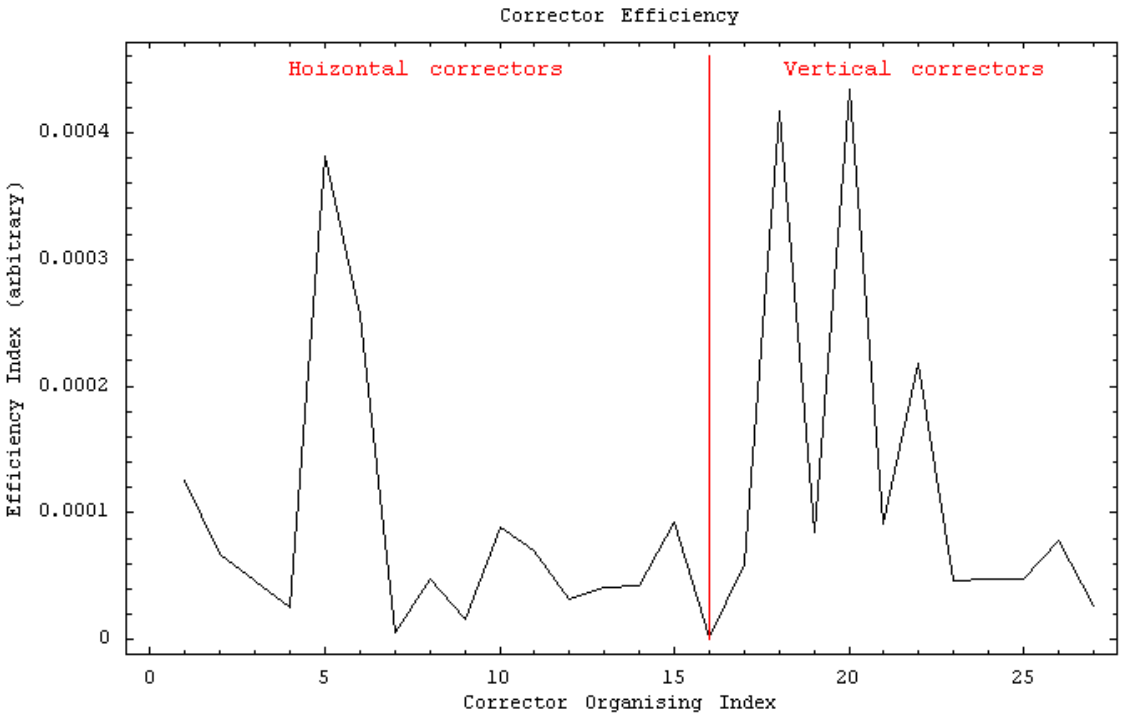

Figure 3.10: An evaluation of the orbit correcting efficiency of the ATF2 extraction line horizontal and vertical correctors resulting from the SVD formalism. Arbitrary units are used. The horizontal axis values start with the first horizontal corrector in the extraction line and follows the horizontal correctors sequentially along the beam line before doing the same for the vertical correctors.

The optimised settings were used to correct a full set of simulated errors. In order to fully correct the orbit as far as possible with the orbit correction procedure, 100 iterations of orbit correction were applied. The horizontal (Fig. 3.12) and vertical (Fig. 3.13) orbits have both been significantly corrected.

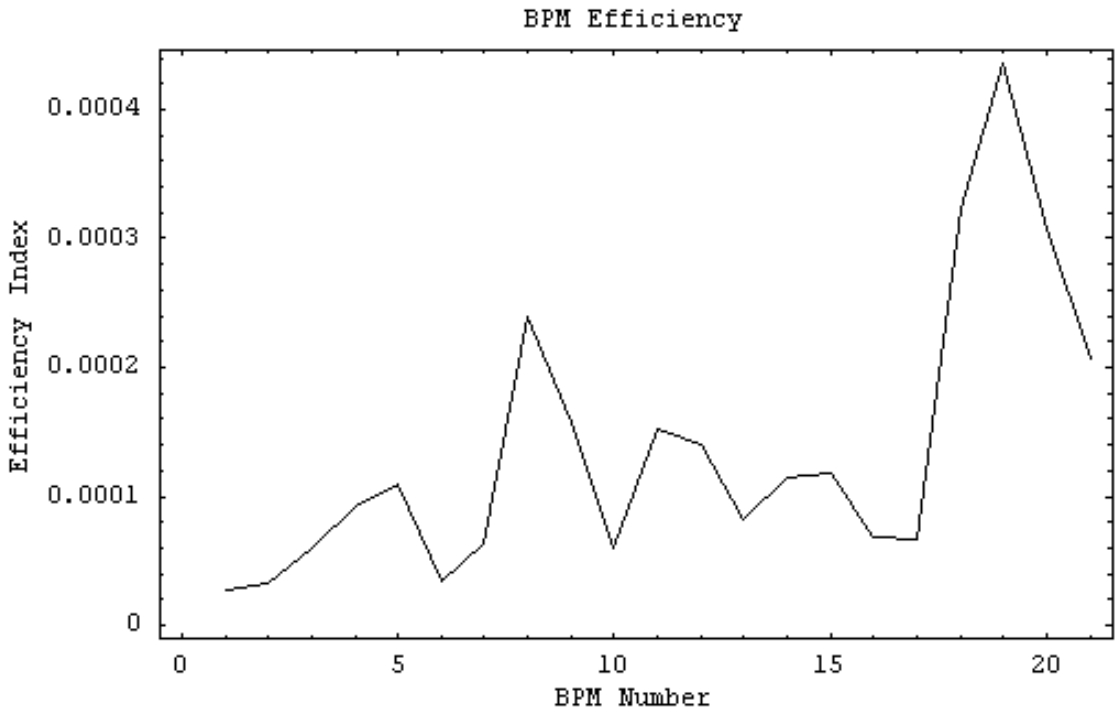

Figure 3.11: An evaluation of the orbit correcting efficiency of the ATF2 extraction line BPMs resulting from the SVD formalism. Arbitrary units are used. The horizontal axis starts with value 1 being the first BPM in the extraction line and increasing for each BPM along the length of the beam line.

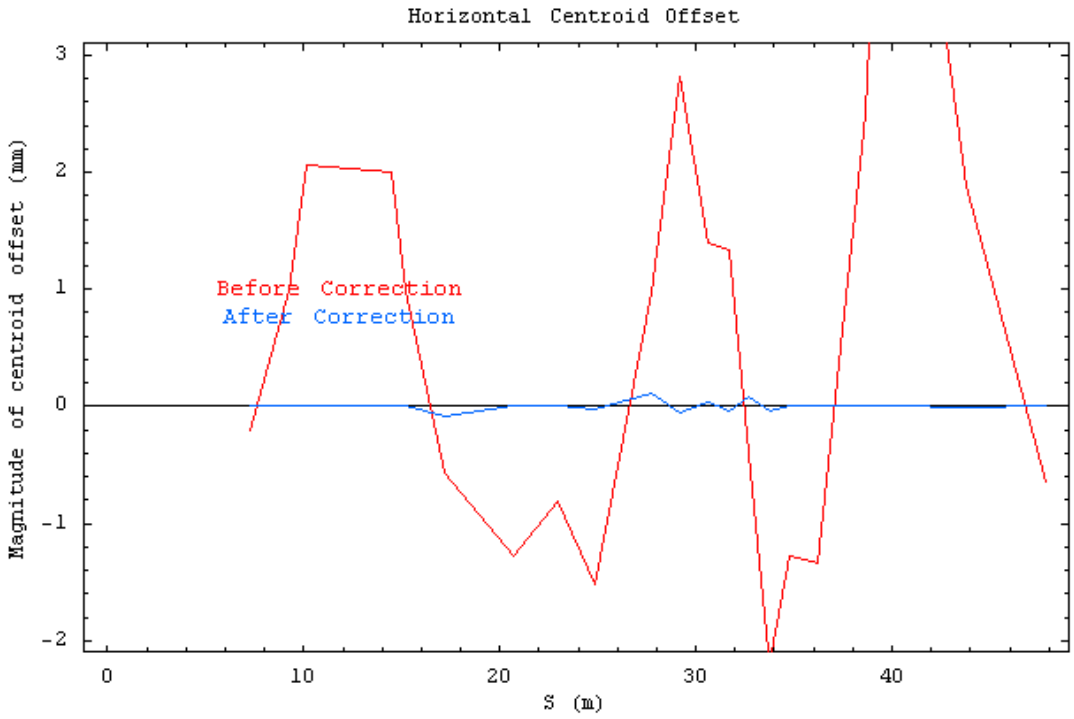

Figure 3.12: The horizontal extraction line orbit before and after 100 iterations of optimised orbit correction have been applied. The value of S starts at the beginning of the extraction line.

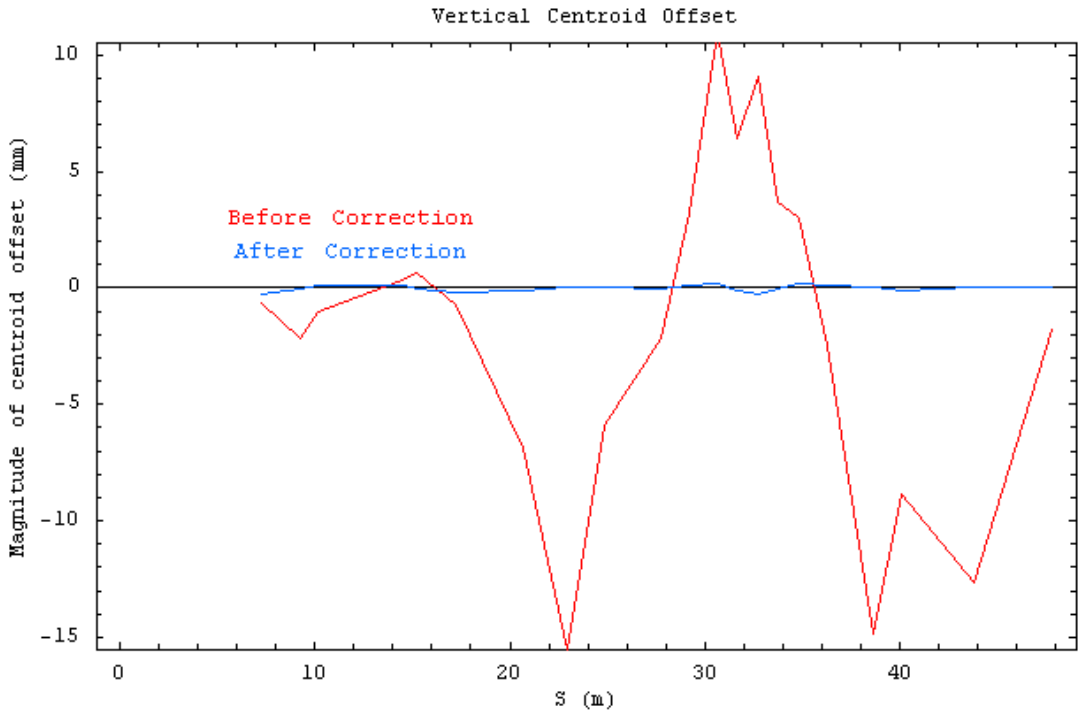

Figure 3.13: The vertical extraction line orbit before and after 100 iterations of optimised orbit correction have been applied. The value of S starts at the beginning of the extraction line.

3.3.4 Orbit Correction Algorithms

There are many different orbit correction methods that can be used on ATF2. Each one may require a different amount of time or have different compromises which can lead to different results and different possible sources of error. This allows for a comparison to be made between different methods and allows for the development and subsequent improvement of the methods.

ATF2 Modularised Global Orbit Correction

The modular global orbit correction method is the method that was chosen for development and testing during this investigation. The optimised extraction line and final focus global orbit correction algorithms may be combined to correct the full length of ATF2. Since ATF2 has been split into two sections, or modules, for the orbit correction purposes the combined process is referred to as 'modular global orbit correction'. The extraction line orbit correction algorithm is used first and then followed by the final focus orbit correction algorithm. The ATF2 was simulated with a full set of errors and each optimised orbit correction algorithm was applied for 100 iterations. The horizontal (Fig. 3.14) and vertical (Fig. 3.15) orbits of ATF2 have both been significantly corrected.

Full ATF2 Global Orbit Correction

It is possible to treat ATF2 as a whole during the orbit correction procedures. This would require simultaneous correction of the extraction line and final focus. In such a scenario the set of horizontal orbit correcting magnets used are all of the horizontal correctors in the extraction line as well as all of the final focus magnet movers. The same principle is applied to the vertical plane as well. All of the BPMs in the extraction line and final focus are also used for the orbit correction. This is referred to as 'full

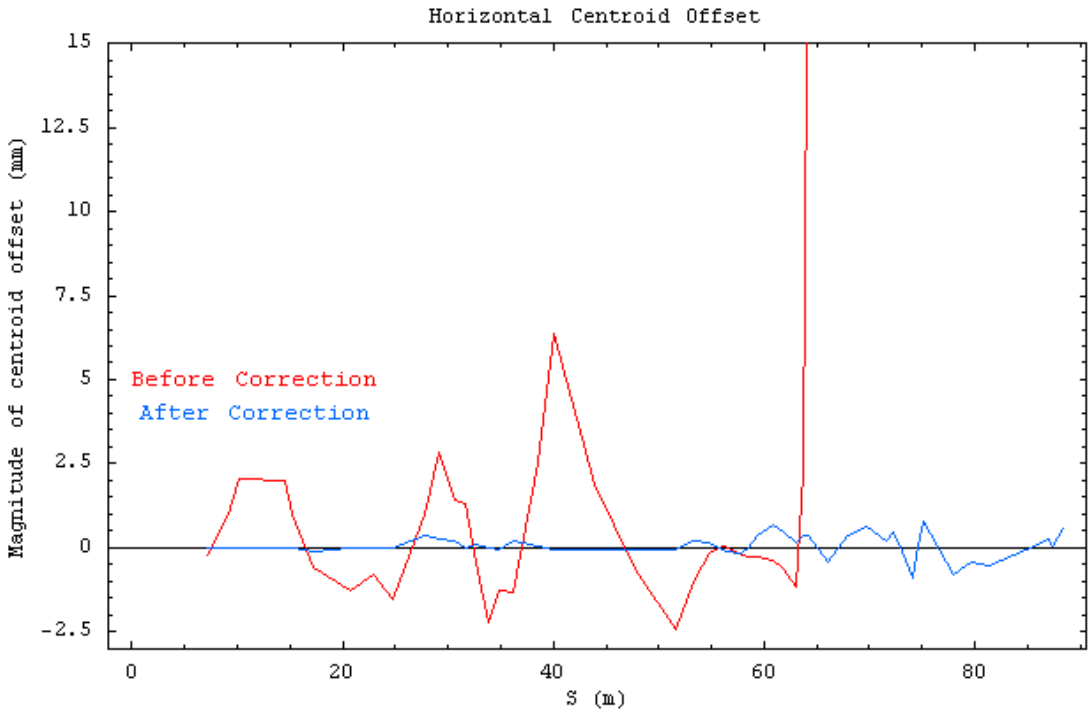

Figure 3.14: The horizontal ATF2 orbit before and after 100 iterations of optimised extraction line orbit correction and 100 iterations of optimised final focus orbit correction have been applied. The value of S starts at the beginning of the extraction line.

ATF2 global orbit correction'.

The number of horizontally and vertically retained eigenvalues were optimised by comparing the orbit correction figure of merit for all combinations of the number of retained eigenvalues for 25 unique seeds of errors. The results indicate that the majority of correcting magnets are detrimental to the orbit correction efficiency. The first correctors tend to have very high responses to all the BPMs and the final focus has very high BPM readings when errors are applied. This resulted in the first correctors trying to correct for the majority of the orbit perturbation. This caused the first correctors to be set to levels that were unrealistic and which would cause beam loss. The optimum number of horizontally and vertically retained eigenvalues are both 2. This results in an average orbit reduction of 60.9% in the horizontal plane and 64.8% in the vertical plane.

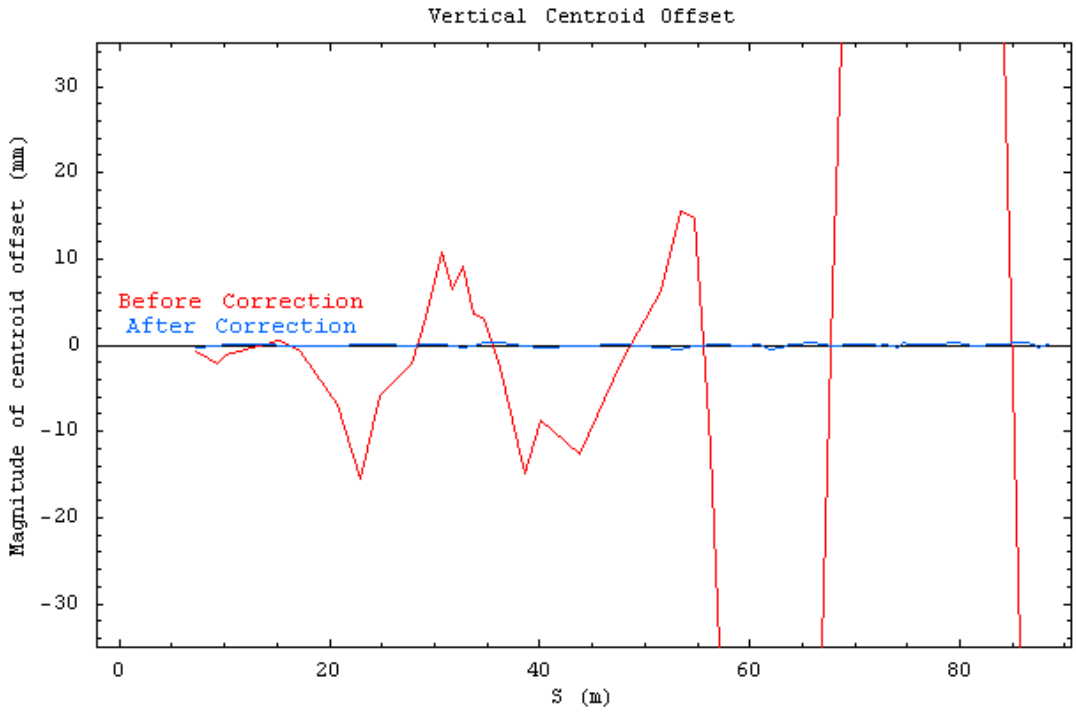

Figure 3.15: The vertical ATF2 orbit before and after 100 iterations of optimised extraction line orbit correction and 100 iterations of optimised final focus orbit correction have been applied. The orbit before correction goes out of the range of the graph due to a need for a clearer visual of the results. The value of S starts at the beginning of the extraction line.

The efficiency ratings of all the correcting magnets (Fig. 3.16) and BPMs (Fig. 3.17) for the full ATF2 global orbit correction procedure were compared. It was found that due to the very low number of retained eigenvalues no improvement could be made by not using the lowest efficiency BPMs or correcting magnets.

The optimised full ATF2 global orbit correction method was tested in simulation with the presence of a full set of errors. The vertical orbit is significantly corrected, however the horizontal orbit received ~ 200% of the desired correction.

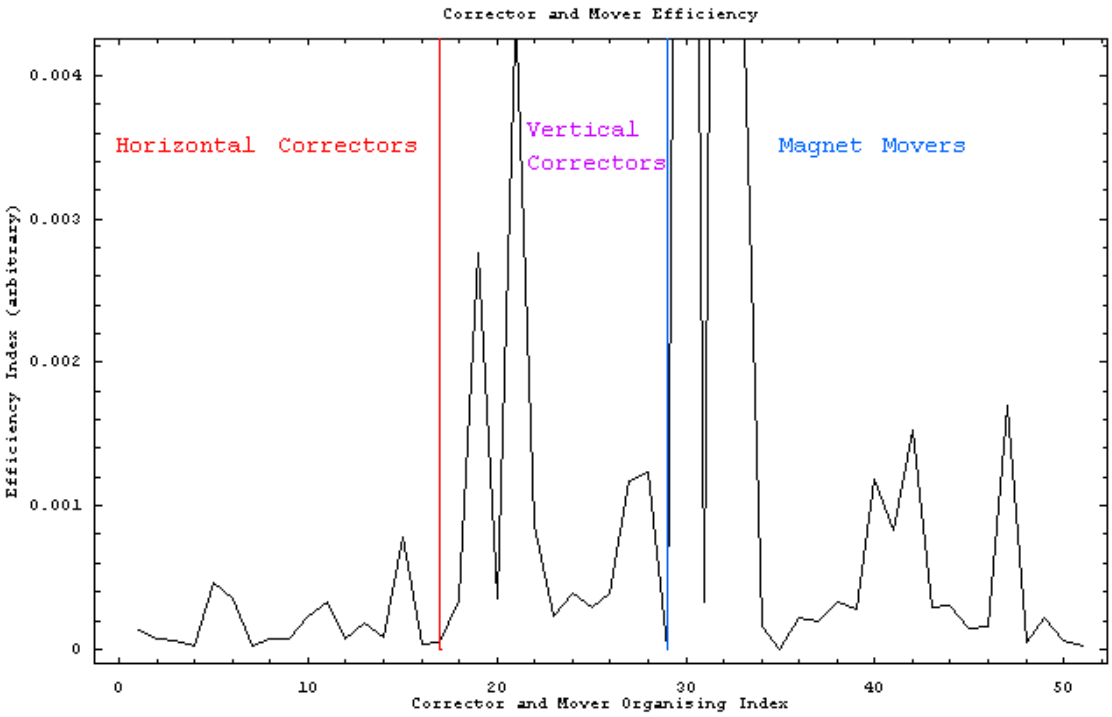

Figure 3.16: An evaluation of the orbit correcting efficiency of all of the ATF2 horizontally and vertically correcting magnets resulting from the SVD formalism. Arbitrary units are used. The horizontal axis starts with the first horizontal extraction line corrector as number 1 and follows the horizontal correctors in sequence, then starting with the first vertical extraction line corrector and following the vertical correctors in sequence before starting with the first final focus quadrupole magnet mover and following the quadrupole magnet movers in sequence along the beam line.

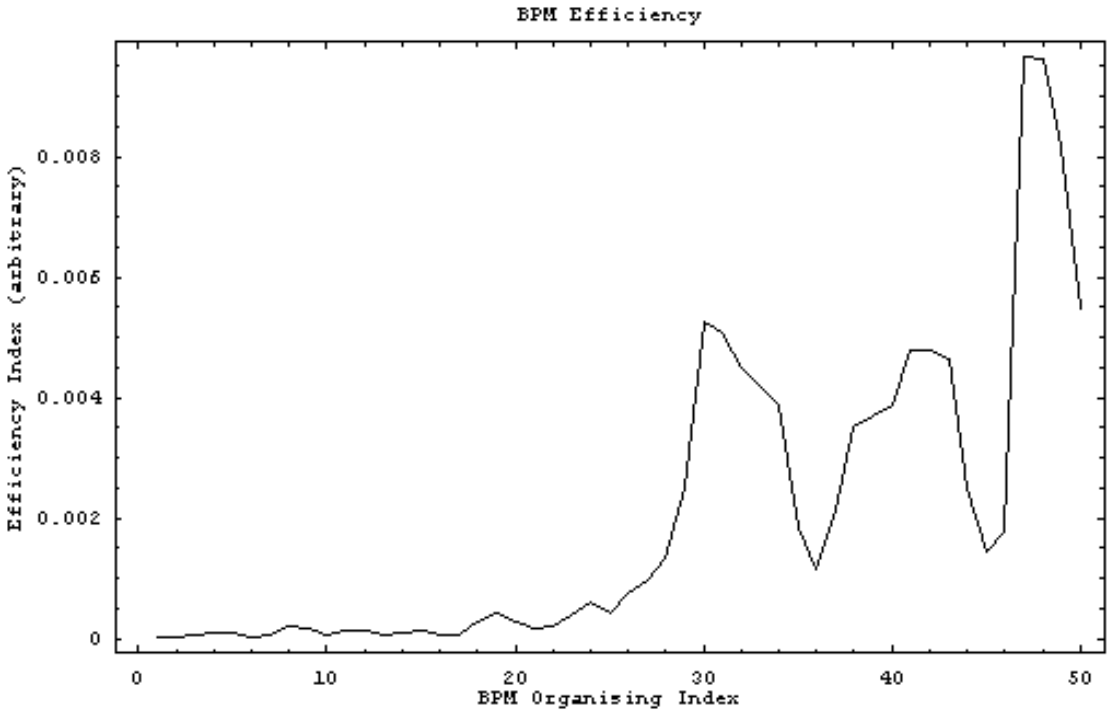

Figure 3.17: An evaluation of the orbit correcting efficiency of all of the ATF2 BPMs resulting from the SVD formalism. Arbitrary units are used. BPM 1 is the first BPM in the extraction line and continues in sequence for all the extraction line and final focus BPMs.

1-to-1 Orbit Correction

A 1-to-1 orbit correction method was investigated for use on ATF2. Each corrector and magnet mover in the extraction line and final focus sections were used for orbit correction. The strength of each corrector and position of each mover was set in turn so that the difference between the current and design orbit at the 3 closest downstream BPMs could be minimised. A Nelder-Mead simplex minimiser (see Appendix B) was used in order to minimise the total position offset from the design values in the 3 BPMs. The ordering of the correctors and magnet movers was based on their positions along the beamline. A full seed of errors was applied and significant levels of orbit correction were achieved in both planes.

Dispersion Free Orbit Correction

A dispersion free orbit correction method was developed for use on ATF2. It is a modified version of the 1-to-1 orbit correction method shown above that also helps to reduce the levels of spurious dispersion in the extraction line and final focus. The levels of dispersion at the 3 downstream BPMs that are closest to each corrector and magnet mover were measured along with the difference from the design beam position at the BPMs. The horizontal dispersion (D_x) at each BPM was measured by recording the beam position at the BPM for a beam with a momentum offset ($\frac{\delta p}{p}$) of 10^{-5} (x_p) and a beam with a momentum offset ($\frac{\delta p}{p}$) of -10^{-5} (x_m). This results in

$$D_x = \frac{x_p - x_m}{2 \cdot 10^{-5}} \tag{3.19}$$

The same equation holds true for the vertical plane. The total dispersion at all three BPMs was multiplied by a weighting factor which was a free parameter that would be set along with the corrector strength or mover position through the use of a Nelder-Mead simplex minimiser. The weighted total dispersion was combined with the beam position offsets at each BPM in order to form the figure of merit that was minimised

in order to set the corrector strength or mover position. This was performed for all correctors and movers in turn. A full set of errors was applied to the extraction line as well as to the final focus and the dispersion free orbit correction procedure was applied.

3.3.5 Comparison of Algorithms

Comparative plots of the vertical orbit (Fig. 3.18) and level of dispersion (Fig. 3.19) along the ATF2 before and after the use of all of the above orbit correction procedures have been made for the same seed of errors.

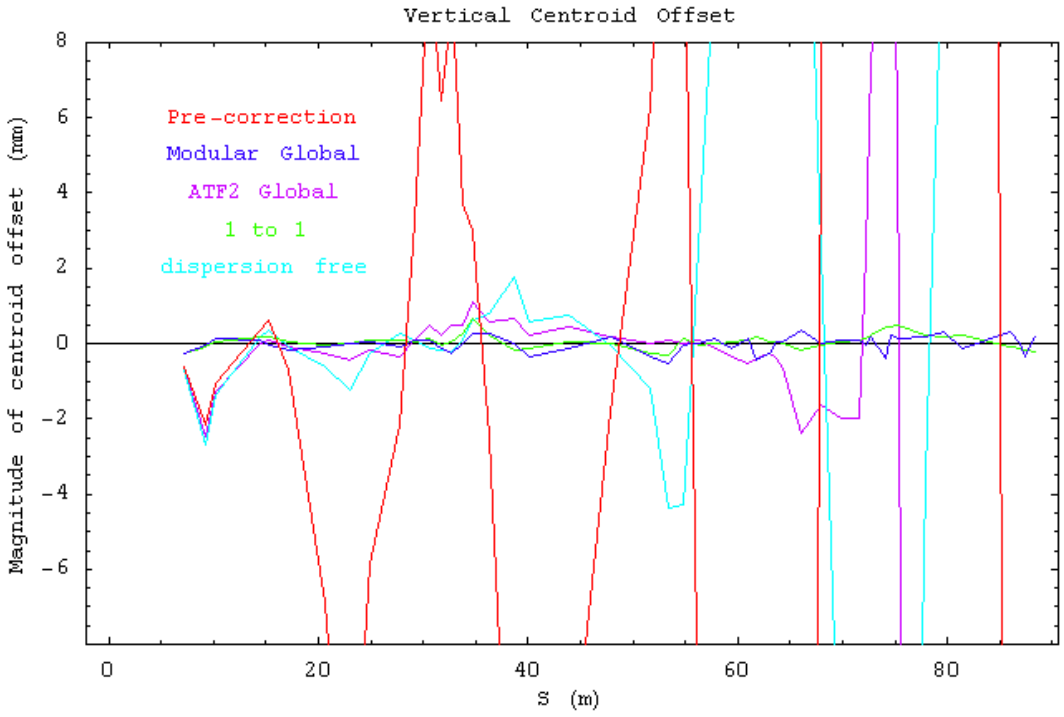

Figure 3.18: A comparison of the change in the vertical orbit along the ATF2 beamline caused by a range of orbit correction procedures. The value of S starts at the beginning of the extraction line.

The modular global orbit correction method and 1-to-1 orbit correction method are comparatively similar in orbit correction efficiency and the resultant levels of dispersion. Both methods are significantly more successful than the other methods shown above, however the 1-to-1 orbit correction method will require multiple sets of BPM

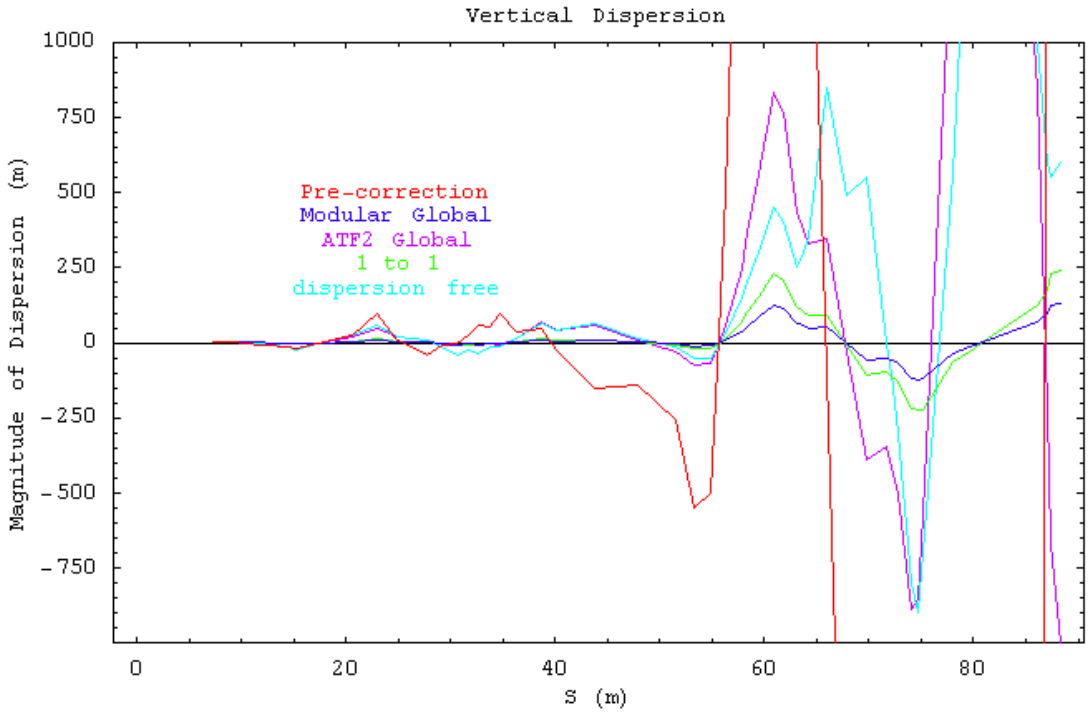

Figure 3.19: A comparison of the change in the vertical dispersion along the ATF2 beamline caused by a range of orbit correction procedures. The value of S starts at the beginning of the extraction line.

readings to be taken for each corrector and magnet mover. This makes the 1-to-1 method significantly slower than the modular global method, which only requires one set of BPM readings for each section of the ATF2 beamline. As a result the modular global orbit correction method has been developed for direct use on the real machine.

The resultant vertical beamsizes (Fig. 3.20) and levels of vertical position jitter (Fig. 3.21) at the beamsize monitor were calculated after the modular global orbit correction method had been applied to 100 seeds of errors. This knowledge was required for use as reference information during the development of the beamsize tuning method discussed in later chapters, which would use the post-orbit correction final focus lattice as the starting point for the beamsize tuning.

The previously presented orbit correction procedures were developed and tested

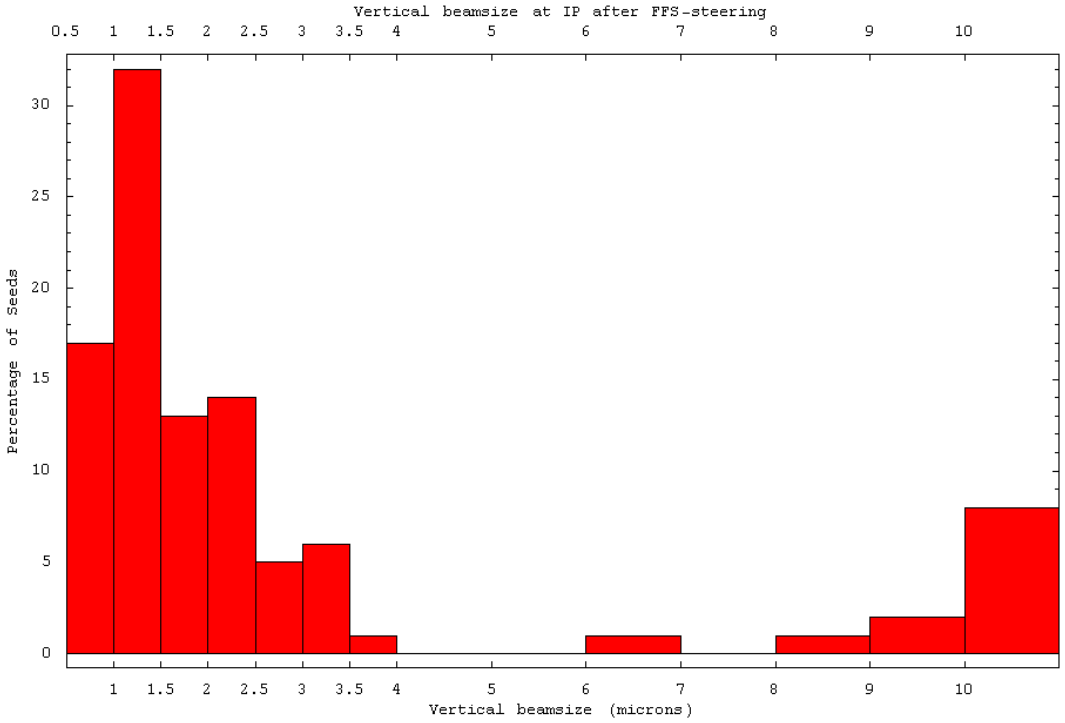

Figure 3.20: The RMS vertical beamsize at the beamsize monitor averaged over 10 beam bunches after the use of modular global orbit correction option 1. The results are for 100 seeds of errors.

using the DIMAD beam dynamics code and Mathematica [17]. The ATF2 software, however, has been modified for use with the ATF2 Flight Simulator control software package [25]. The Flight Simulator software uses the Lucretia beam dynamics package [29] developed for use with MATLAB [18]. As a result the modular global orbit correction procedure shown above was converted for use with Lucretia and MATLAB to allow for it to be integrated into the ATF2 control software and subsequently tested on ATF2.

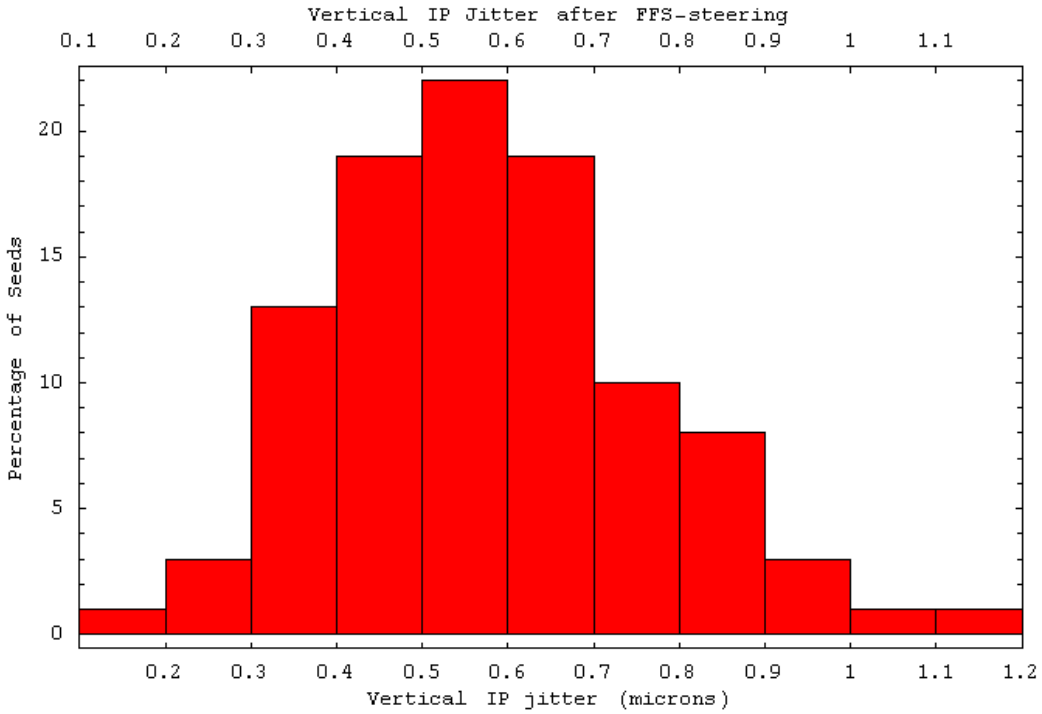

Figure 3.21: The magnitude of variation of the vertical beam position at the beamsize monitor averaged over 10 beam bunches after the use of modular global orbit correction option 1. The results are for 100 seeds of errors.

3.4 Implementation on ATF2

3.4.1 Section Overview

In Part 2 of this section the ATF2 orbit correction algorithms developed by another research team are presented and compared to the orbit correction algorithm shown above using results from 100 random simulations.

In Part 3 the development of the orbit correction algorithms as a usable software package for ATF2 is discussed.

In Part 4 the simulation results of a comparison of the two sets of algorithms using a simplified scenario are presented along with simulation results using a full range of realistic errors. The real-life results from a comparison of the performance of the codes on ATF2 using the simplified scenario is also presented. Results from a study into the impact the intensity dependence of the ATF2 stripline BPMs have on the orbit correction algorithms is also shown.

3.4.2 Code Comparison

A competing set of orbit correction algorithms have been developed by Yves Renier [22]. These algorithms are also of the modular global orbit correction design, however the response matrices are calculated directly from the transfer matrices taken from the theoretical lattice and not from direct response measurements. The resultant response matrices have been designed to include coupling effects by using all the correctors in the extraction line, irrespective of the plane in which a correction is generated by the correctors, to correct for both the horizontal and vertical orbits. When no coupling is present there should be minimal difference in the response matrices developed by the two competing methods. The two competing sets of codes were each used to correct 100 seeds of errors. These were not identical, however the scale of the errors in all cases were taken from the official error statistics. The optimised modular global orbit

correction procedure demonstrated above will be referred to as 'Option 1'. The orbit correction procedure developed by Yves Renier will be referred to as 'Option 2'. The extraction line orbit correction procedures were implemented first. Both orbit correction procedures were iteratively run until no more orbit correction could be achieved (Fig. 3.22 & Fig. 3.23).

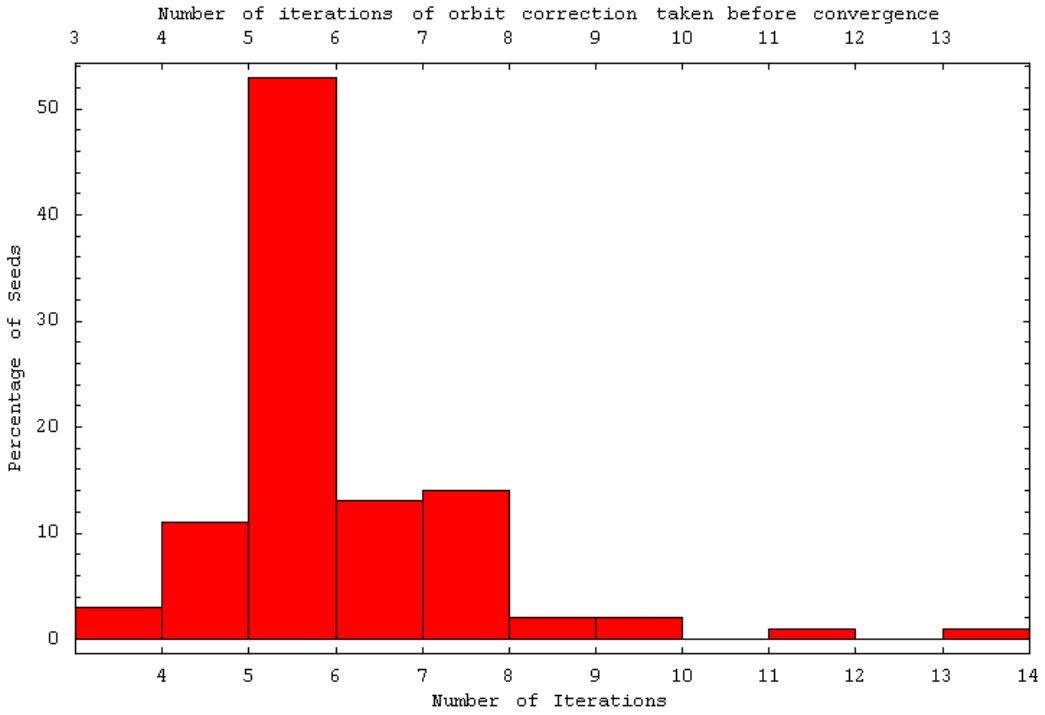

Figure 3.22: The number of iterations required by extraction line orbit correction option 1 in order to converge to the best possible orbit. The results are for 100 seeds of errors.

The average number of iterations required for option 1 ($\sim$ 6, as seen in Fig. 3.22) is 20 times less than the amount needed for option 2 ($\sim$ 120, as seen in Fig. 3.23) which indicates that option 1 should be $\sim$ 20 times faster than option 2 in correcting the extraction line orbit. The resultant average root mean square (RMS) values of the horizontal ($\sim$ 4 mm for option 1 and $\sim$ 1 mm for option 2) and vertical ($\sim$ 0.75 mm for option 1 and $\sim$ 0.6 mm for option 2) beam positions at each of the BPMs in the extraction line were calculated for 100 seeds of errors. The results show a significant advantage in the horizontal plane when option 2 is used but there is no significant ad-

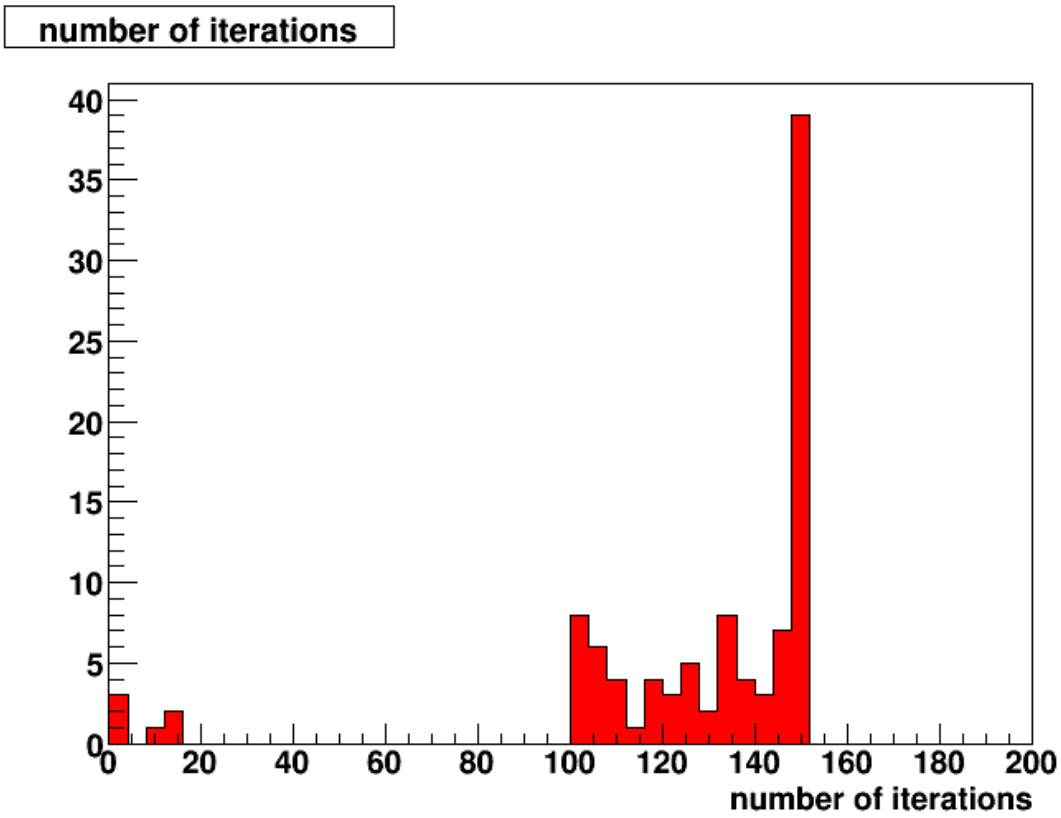

Figure 3.23: The number of iterations required by extraction line orbit correction option 2 in order to converge to the best possible orbit. The results are for 100 seeds of errors.

vantage shown in the vertical plane. The final focus orbit correction procedures were then applied. The procedures were iteratively applied until no more orbit correction could be achieved (Fig. 3.24).

The resultant average root mean square (RMS) values of the horizontal ($\sim$ 200 microns for option 1 and $\sim$ 150 microns for option 2) and vertical ($\sim$ 150 microns for option 1 and $\sim$ 150 microns for option 2) beam positions at each of the BPMs in the final focus were calculated for 100 seeds of errors. The results show a slight advantage in the horizontal plane when option 2 is used but there is no advantage shown in the vertical plane. Due to the similarities in performance, both orbit correction options were chosen for development and implementation on ATF2.

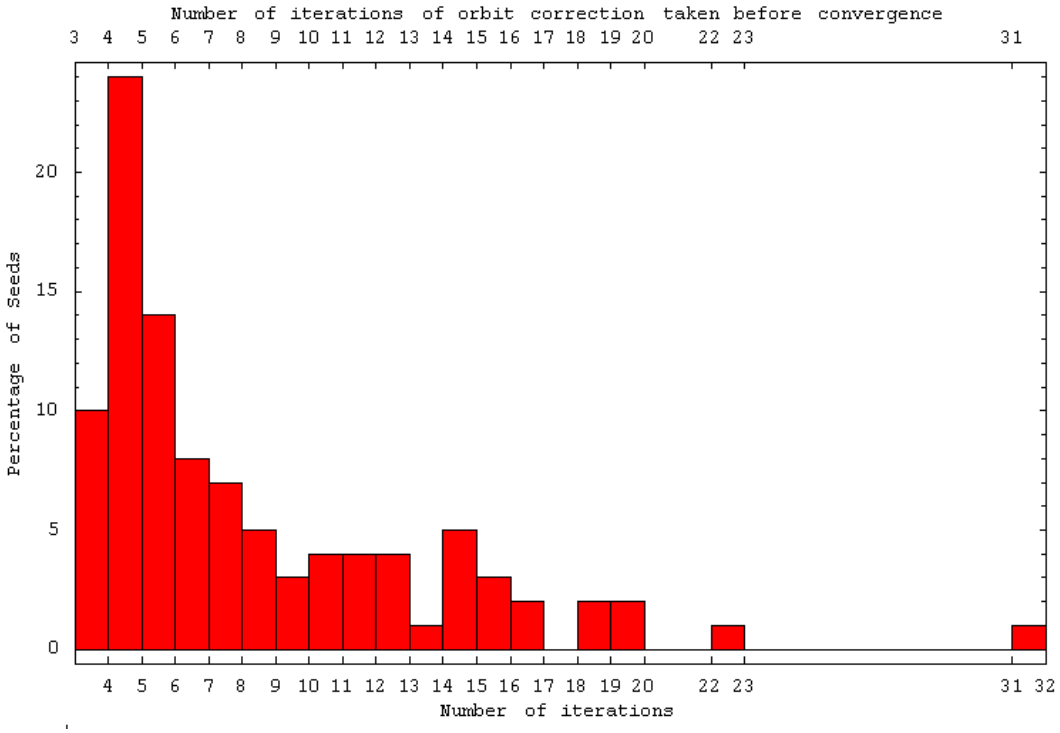

Figure 3.24: The number of iterations required by final focus orbit correction option 1 in order to converge to the best possible orbit. The results are for 100 seeds of errors.

3.4.3 Software Development

As the ATF2 facility incorporates many R & D projects, the hardware used for the orbit correction procedures may not always be available and significant changes to the beam optics are possible. As a result the optimised settings for the orbit correction procedures may not always be valid. Instead of using 'hard coded' values for the number of retained eigenvalues, or for which correcting magnets or BPMs to use, the final program allowed for each BPM and correcting magnet to be weighted for how much emphasis should be placed on them when performing orbit correction. This allows for unreliable or inefficient correcting magnets and BPMs to be effectively ignored (zero weighted) during the orbit correction process while allowing for greater orbit correction at the most important sections of the beamline. The ability to specify a target orbit was also given, whereby the orbit correction procedure would attempt to minimise the offset between the current orbit and the target orbit. Due to the possibility of erroneous

measurements or poor hardware performance as well as many other unexpected complications which may impact the reliability of the orbit correction, a 'half correction' capability was also included. The half correction algorithm would apply half of the correction calculated by the normal orbit correction algorithm. This allows for a slow iterative correction to be performed even if the original orbit correction algorithm had overestimated the correction needed by 100%.

3.4.4 Software Tests

'Proof of Concept' Simulation Tests

A simple test was devised to demonstrate the orbit correction capabilities of the modular global orbit correction procedure. The Flight Simulator versions of both the extraction line and final focus orbit correction algorithms were individually tested to show that they could correct the orbit perturbation generated by a single error source.

ATF2 was simulated without offsets. A 0.3 amp current supply error was applied to the horizontal corrector ZH2X and all other correctors were zero weighted. Extraction line orbit correction was applied (Fig. 3.25). The resultant current supplied to ZH2X was near the design value and the orbit was corrected.

The same scenario was tested again while using all horizontal correctors (Fig. 3.26). The resultant orbit has been corrected, however the use of multiple correctors has led to a non-ideal correction due to the 'best fit' nature of the orbit correction algorithm.

An error-free simulation of ATF2 was created. A 0.2 mm horizontal offset was applied to the final focus quadrupole QM14FF. The final focus orbit correction algorithm was used to correct the horizontal orbit only using QM14FF (Fig. 3.27). The resultant correction was half of the desired correction.

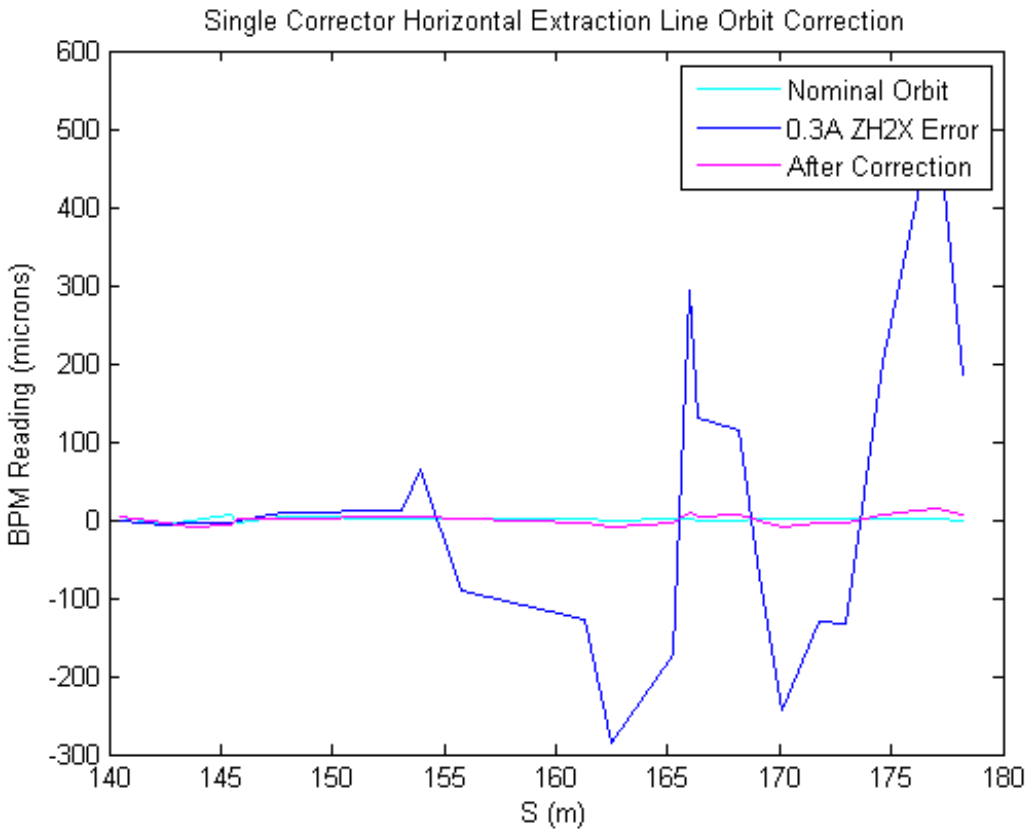

Figure 3.25: A single 0.3 amp current supply error was applied to ZH2X in an error-free simulation of ATF2. The extraction line orbit correction algorithm was applied only using corrector ZH2X. The value of S starts at the beginning of ATF2.

The same scenario was tested when all magnet movers were used to correct the horizontal orbit (Fig. 3.28). The resultant orbit is well corrected, however the 'best fit' nature of the algorithm has led to the remainder of some orbit perturbation.

Realistic Error Simulation Tests

The codes were tested in the most accurate simulations of ATF2 possible. A complete range of errors [20] were applied to the current ATF2 lattice. The extraction line orbit correction procedure was applied first (Fig. 3.29 & Fig. 3.30). Both planes were well corrected.

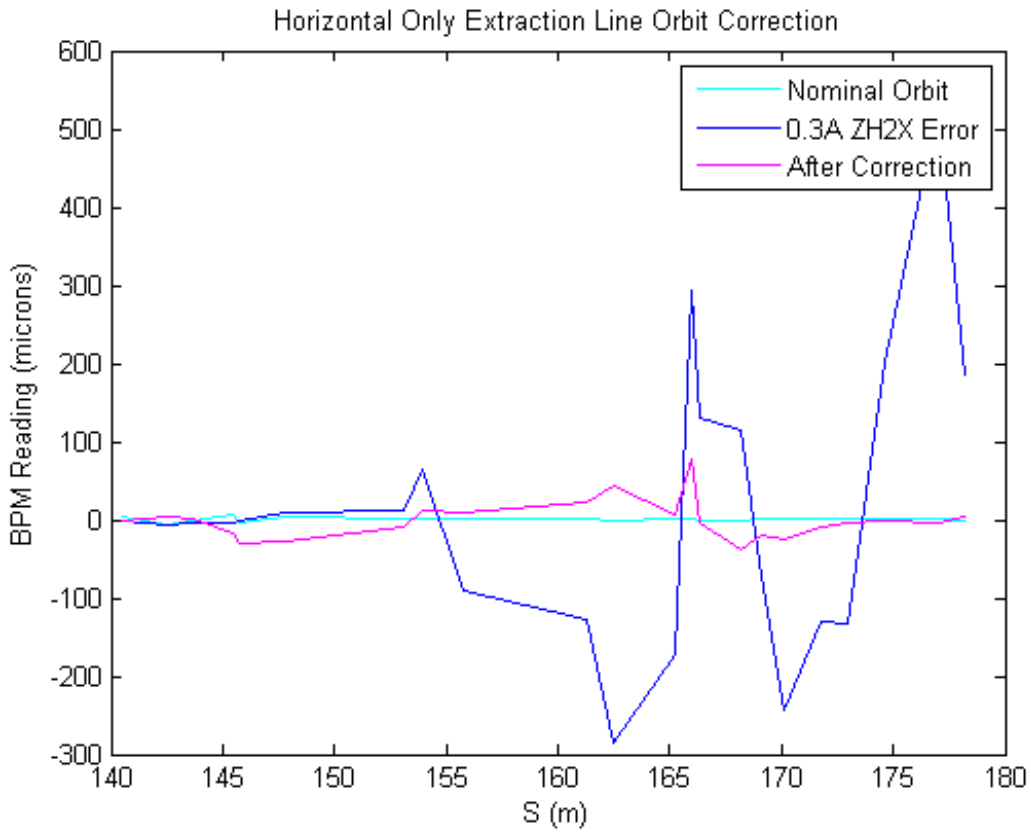

Figure 3.26: A single 0.3 amp current supply error was applied to ZH2X in an error-free simulation of ATF2. The extraction line orbit correction algorithm was applied using all horizontal correctors. The value of S starts at the beginning of ATF2.

The final focus orbit correction procedure was then applied (Fig. 3.31 & Fig. 3.32). The vertical orbit is well corrected, however the horizontal orbit was over-corrected by 100% in the first iteration and was well corrected after the second iteration. This is a result of the 'best fit' nature of the orbit correction algorithm and indicates an importance for the use of multiple iterations of orbit correction.

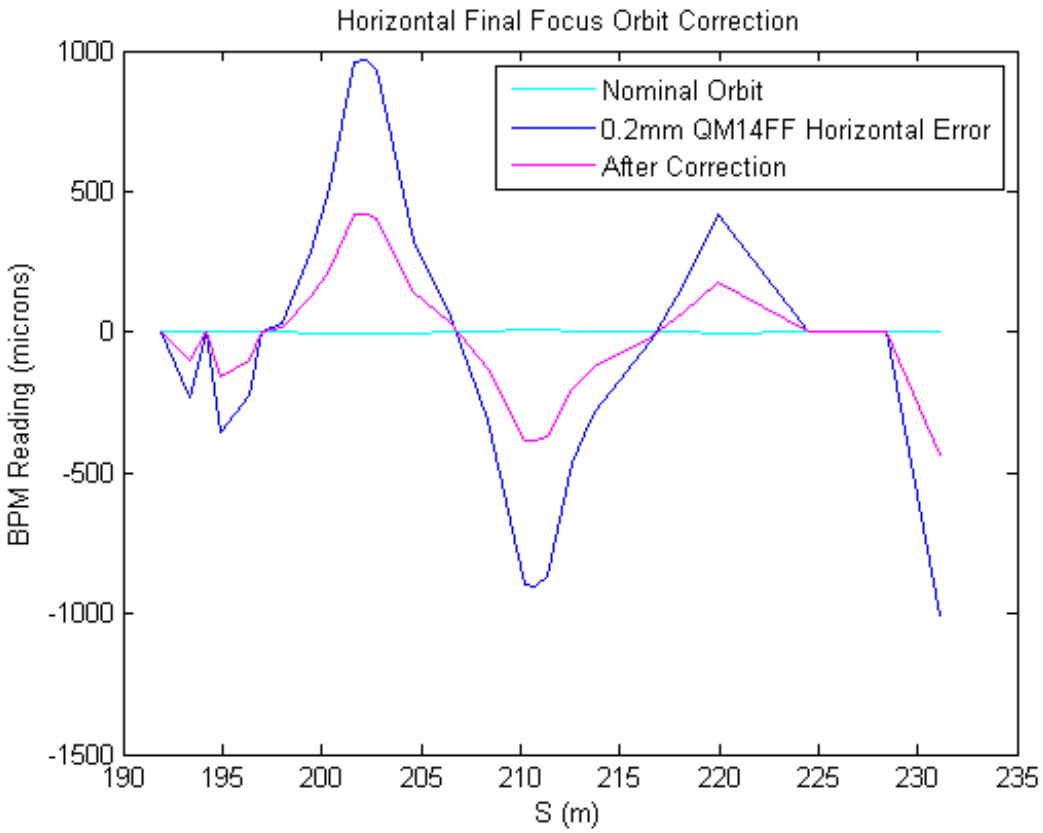

Figure 3.27: A single 0.2 mm horizontal offset error was applied to QM14FF in an error-free simulation of ATF2. The final focus orbit correction algorithm was applied only using QM14FF. The value of S starts at the beginning of ATF2.

Experimental Tests

The modular global orbit correction procedure was tested on the real machine in May 2009. The simple 'proof of concept' tests shown above were recreated on the real machine.

The extraction line orbit correction algorithm was tested first. The ATF2 orbit at the start of the test was set as the target orbit. A 0.3 amp current supply change was made to ZH2X. The extraction line orbit correction algorithm was used to calculate a correction to the current supplied to ZH2X. A correction of -0.44 amp was calculated. This corresponds to an over-correction of 47%. The calculated correction was not ap-

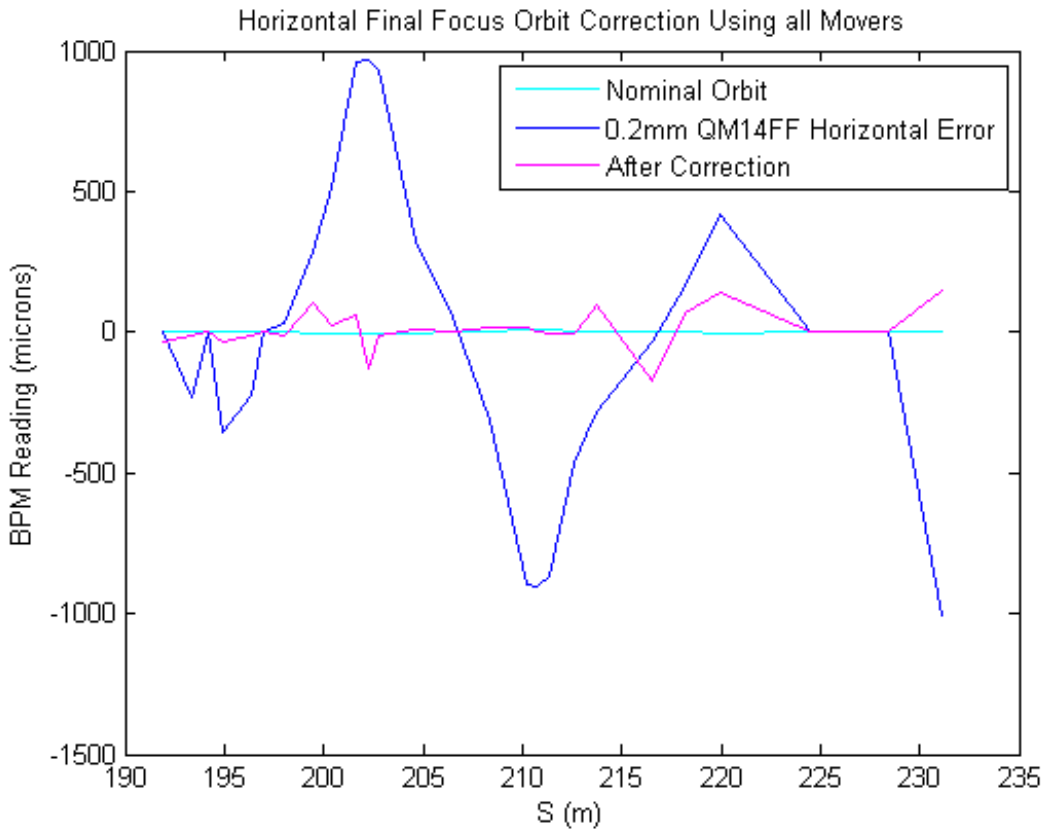

Figure 3.28: A single 0.2 mm horizontal offset error was applied to QM14FF in an error-free simulation of ATF2. The final focus orbit correction algorithm was applied to the horizontal orbit only using all magnet movers. The value of S starts at the beginning of ATF2.

plied and a correction using all horizontal correctors was calculated. The calculated correction resulted in significant over-correction of the order of 50 - 100% (Fig. 3.33). A half-correction was also attempted, which resulted in a significantly improved orbit correction.

Tests performed on ATF2 using the orbit correction code developed by Yves Renier also show an over-correction of the order of 50 - 100% (Fig. 3.34).

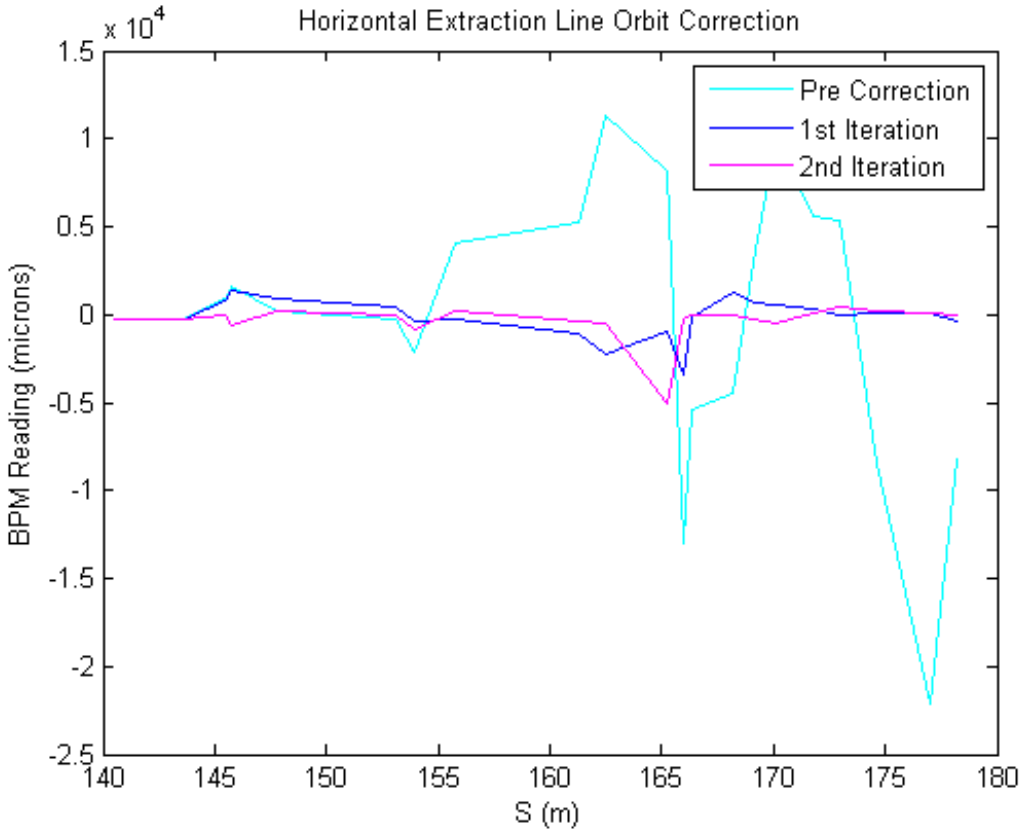

Figure 3.29: The ATF2 horizontal orbit before and after the application of the extraction line orbit correction procedure. The value of S starts at the beginning of ATF2.

BPM Intensity Dependence

The cause of this over-correction has been attributed to an intensity dependence in the extraction line stripline BPMs [24]. A stripline BPM consists of 4 longitudinal electrodes (Fig. 3.35).

The electrodes are electromagnetically excited by the presence of the charged beam. The proximity of the beam to the electrode governs the intensity of the current, or signal, along the electrode. The signal from each electrode is passed through a diode and then through an amplifier in order to correct and intensify the signal generated at the electrode. The horizontal and vertical beam centroid positions (x and y respectively)

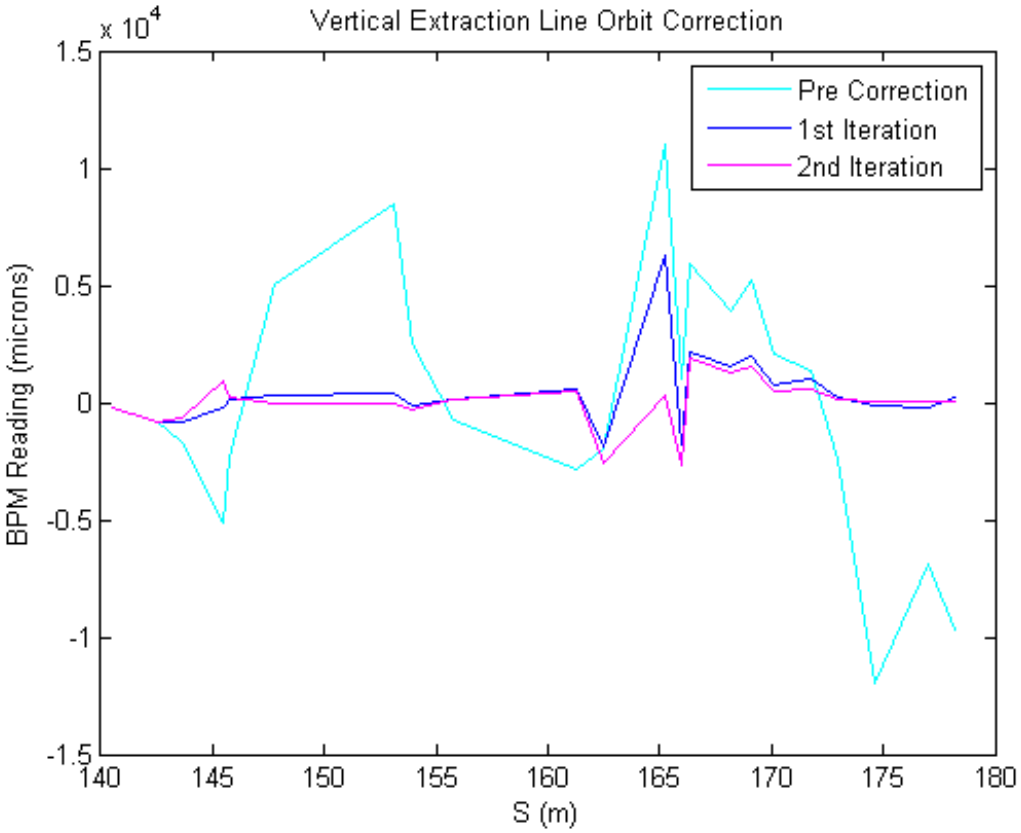

Figure 3.30: The ATF2 vertical orbit before and after the application of the extraction line orbit correction procedure. The value of S starts at the beginning of ATF2.

are given by

$$x = \alpha \frac{(I_1 + I_3) - (I_2 + I_4)}{I_1 + I_2 + I_3 + I_4} \tag{3.20}$$

$$y = \alpha \frac{(I_1 + I_2) - (I_3 + I_4)}{I_1 + I_2 + I_3 + I_4} \tag{3.21}$$

where I_1 to I_4 are the signal intensities at electrode 1 to 4 respectively. At ATF2 these amplifiers have a non-linear relationship to the intensity of the beam and the non-linearity of each amplifier is different.

On ATF2 the intensity of the beam was varied while the beam orbit was kept constant. The beam position calculated by each stripline BPM at varying levels of beam intensity was recorded and the intensity dependence was noted (Fig. 3.36 & Fig. 3.37).

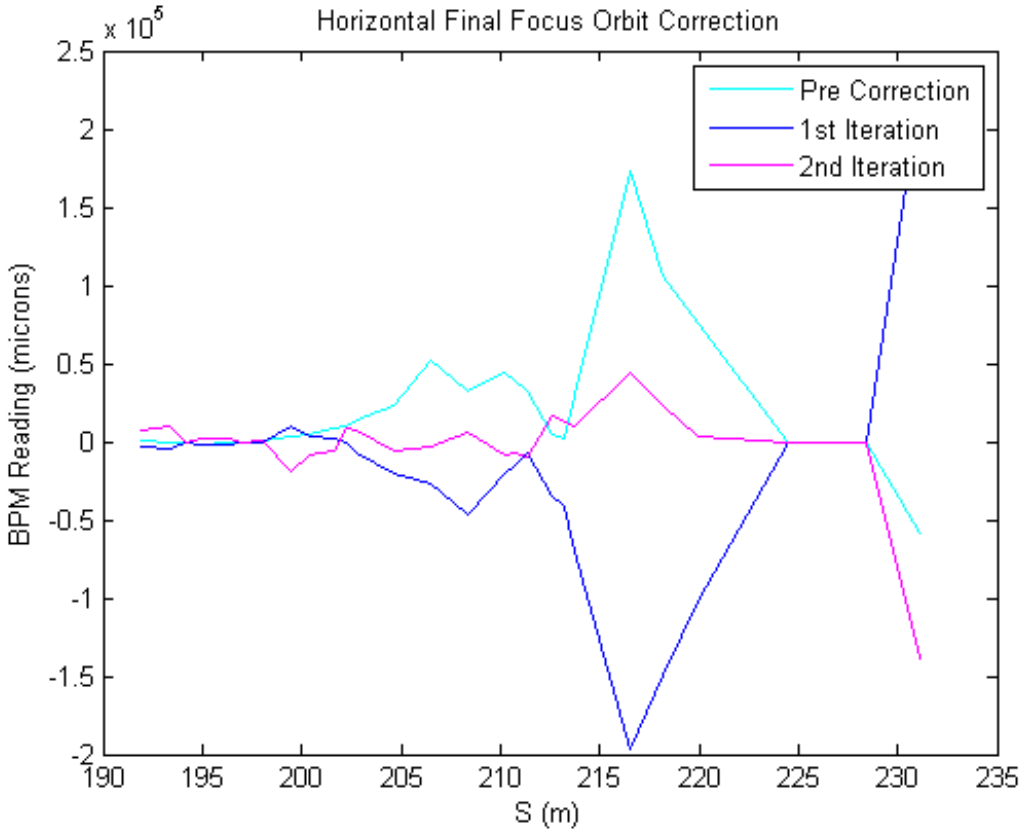

Figure 3.31: The ATF2 horizontal orbit before and after the application of the final focus orbit correction procedure. The value of S starts at the beginning of ATF2.

Most of the stripline BPMs show a large intensity dependence with beam position reading error factors of between 0.5 and 3.

As a test of this theory ATF2 was simulated without errors. The nominal orbit was taken. Each extraction line stripline BPM was randomly assigned a beam position reading error factor of between 0.5 and 3. These factors were applied to all orbit readings. The nominal orbit with stripline BPM reading errors was used as the target orbit. ZH2X was given a 0.3 amp current supply error and the orbit with stripline BPM reading errors was taken. Extraction line orbit correction was applied to correct this orbit. The resultant orbit with stripline BPM reading errors shows an over-correction

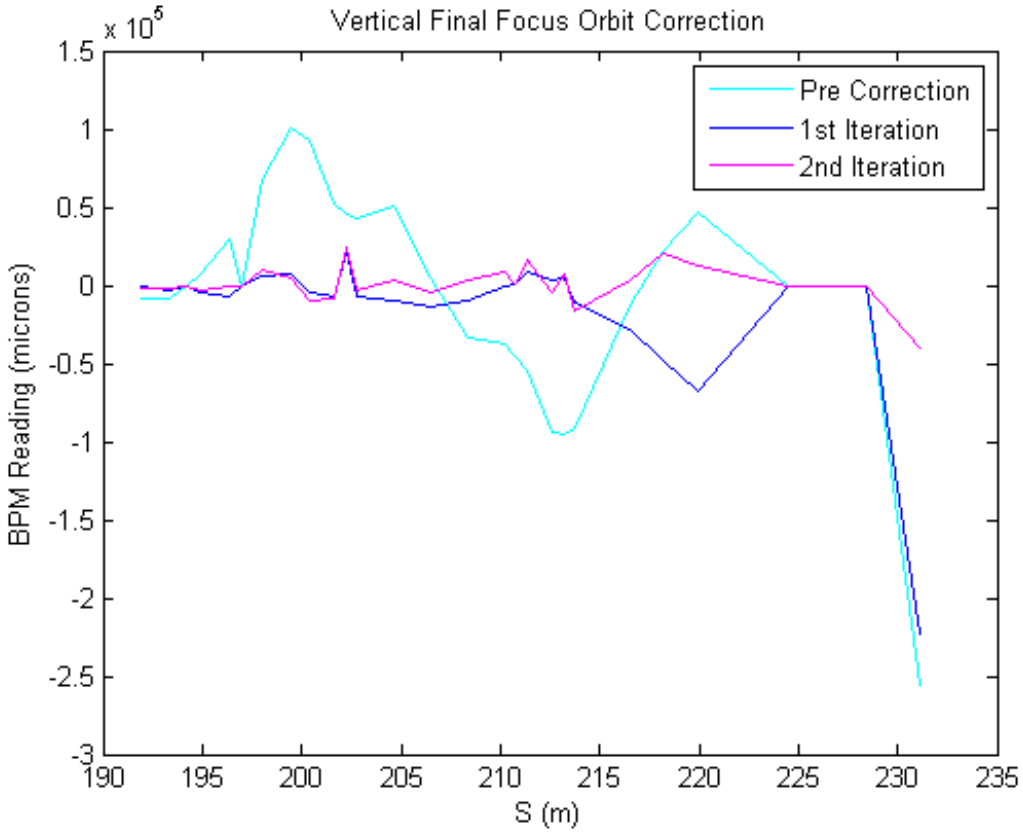

Figure 3.32: The ATF2 vertical orbit before and after the application of the final focus orbit correction procedure. The value of S starts at the beginning of ATF2.

(Fig. 3.38). Half-correction results have also been produced.

The effects of the stripline BPM reading errors were removed from the orbits given in Fig. 3.38. Some of the BPM readings clearly show that the stripline BPM reading errors have lead to more than a factor of 2 increase in the BPM readings (Fig. 3.39).

The RMS of the target orbit when stripline BPM reading errors are present was 63.6% higher than the RMS of the target orbit when the stripline BPM reading errors were removed. The effects of the stripline BPM reading errors on the RMS of the difference between the beam orbit and the target orbit at all stages of the orbit correction procedure were calculated (Table 3.2). The stripline BPM reading errors have had a

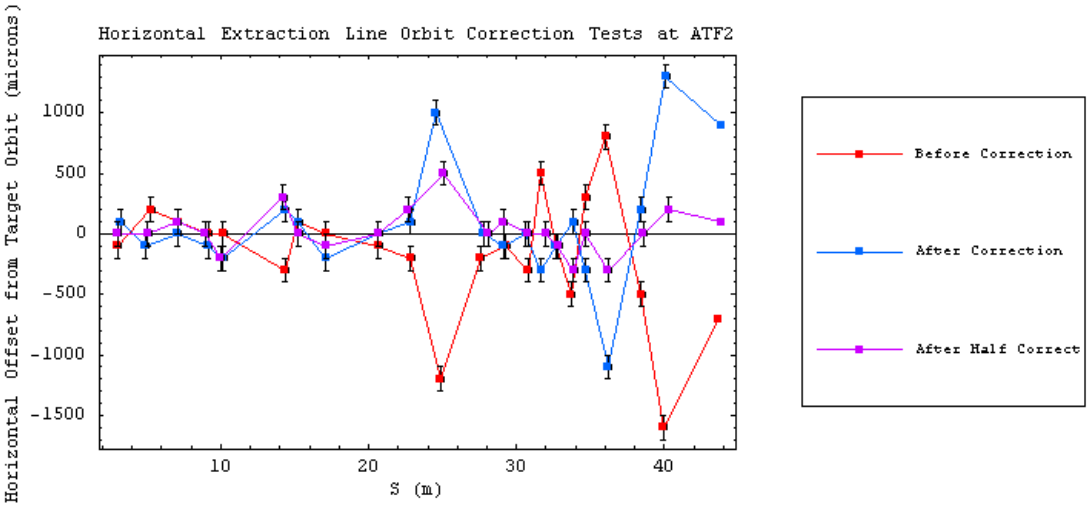

Figure 3.33: The ATF2 horizontal orbit measured from the real machine before and after the application of extraction line orbit correction on the horizontal orbit. The half-correction results are also shown. The value of S starts at the beginning of the extraction line.

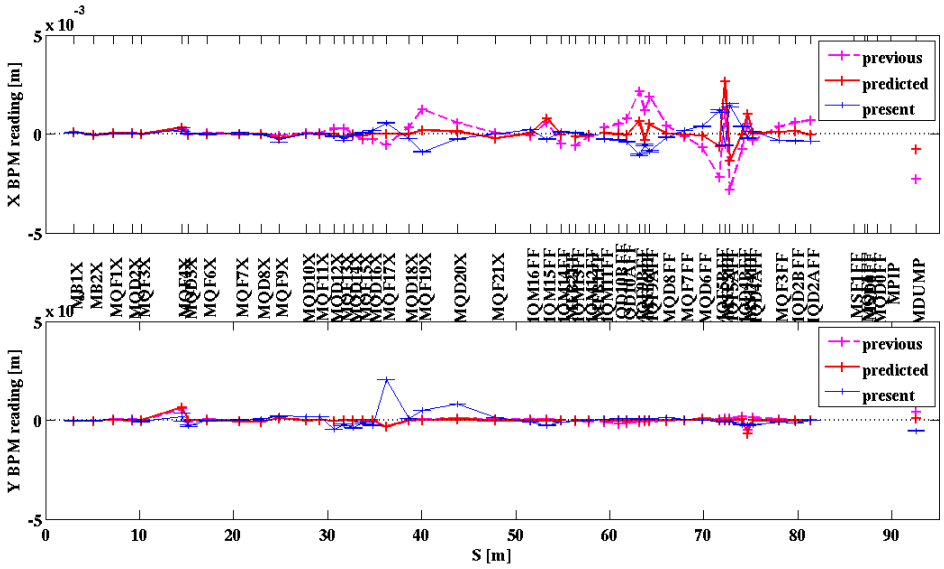

Figure 3.34: The ATF2 orbit measured from the real machine before and after the application of the extraction line horizontal orbit correction method developed by Yves Renier [23]. The results predicted by simulations made using the 'online model' are also shown. The value of S starts at the beginning of the extraction line.

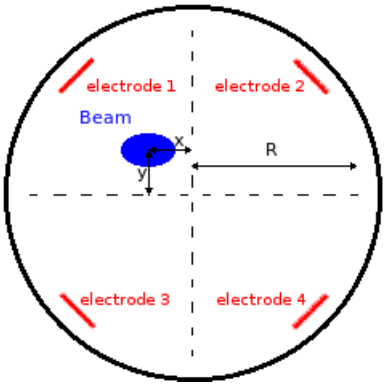

Figure 3.35: A diagram showing the relative position of the longitudinal electrodes used in a stripline BPM within the beam pipe.

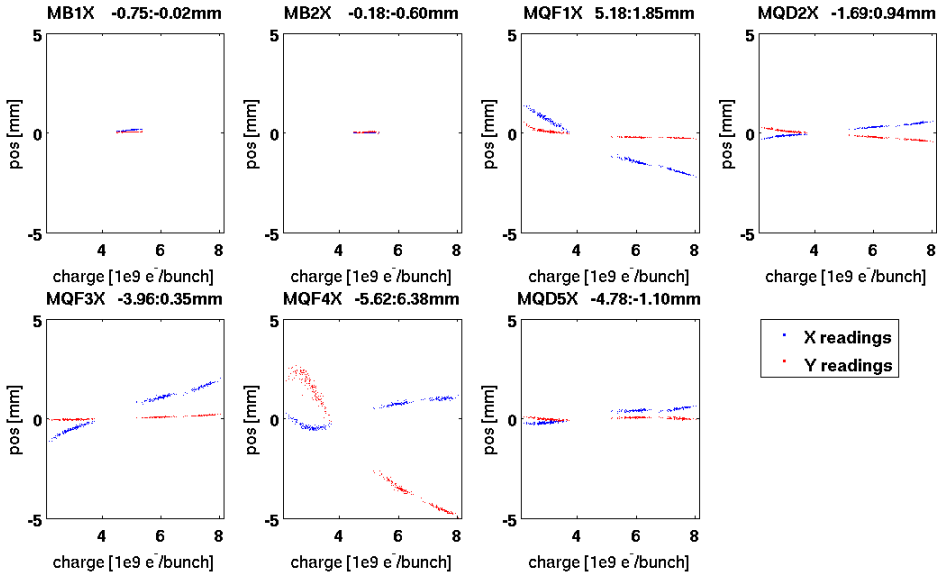

Figure 3.36: The calculated beam position at the first 7 stripline BPMs in the extraction line as a function of beam intensity.

significant impact on the orbit readings taken as part of the extraction line orbit correction procedure.

At the time of writing the final focus orbit correction code developed for this report and the code developed by Yves Renier have both been unable to successfully correct the beam orbit.

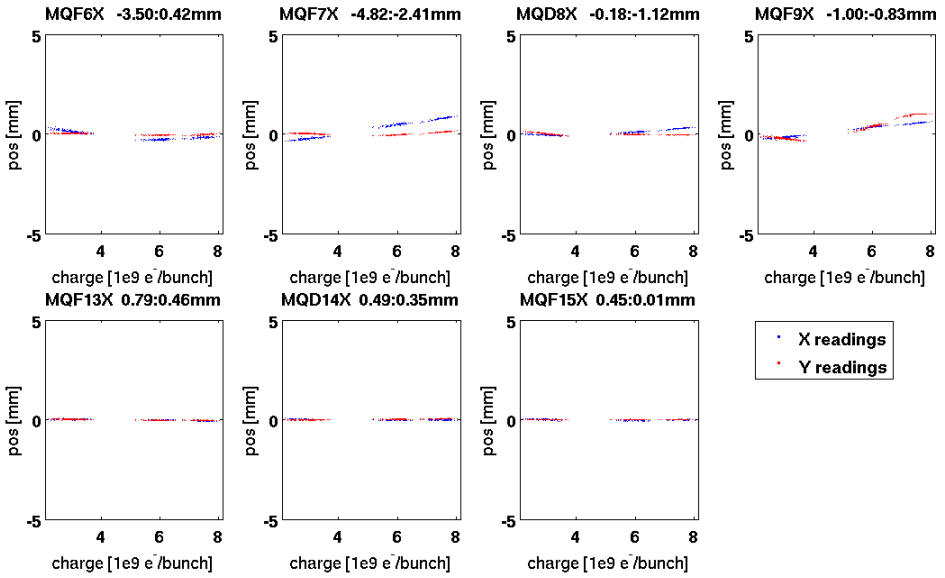

Figure 3.37: The calculated beam position at the last 7 stripline BPMs in the extraction line as a function of beam intensity.

Table 3.2: The effects of stripline BPM reading errors on the RMS difference between the beam orbit and the target orbit.

Correction Phase	**With Errors** (μm)	**w/o Errors** (μm)	**Increase** (%)
Before	238.86	178.83	33.57
After	259.10	107.36	141.34
After 1/2	97.44	86.23	13.00

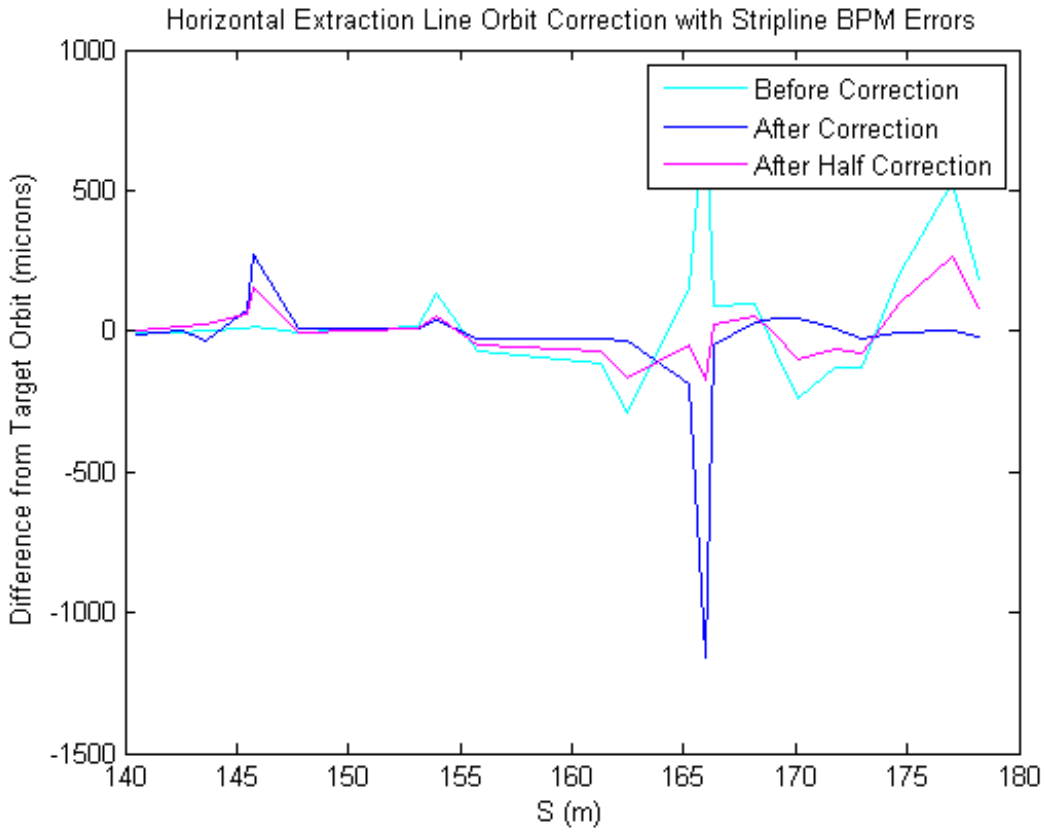

Figure 3.38: The ATF2 horizontal orbit as measured when stripline BPM reading errors have been simulated before and after the application of extraction line orbit correction on the horizontal orbit. The half-correction results are also shown. The value of S starts at the beginning of ATF2.

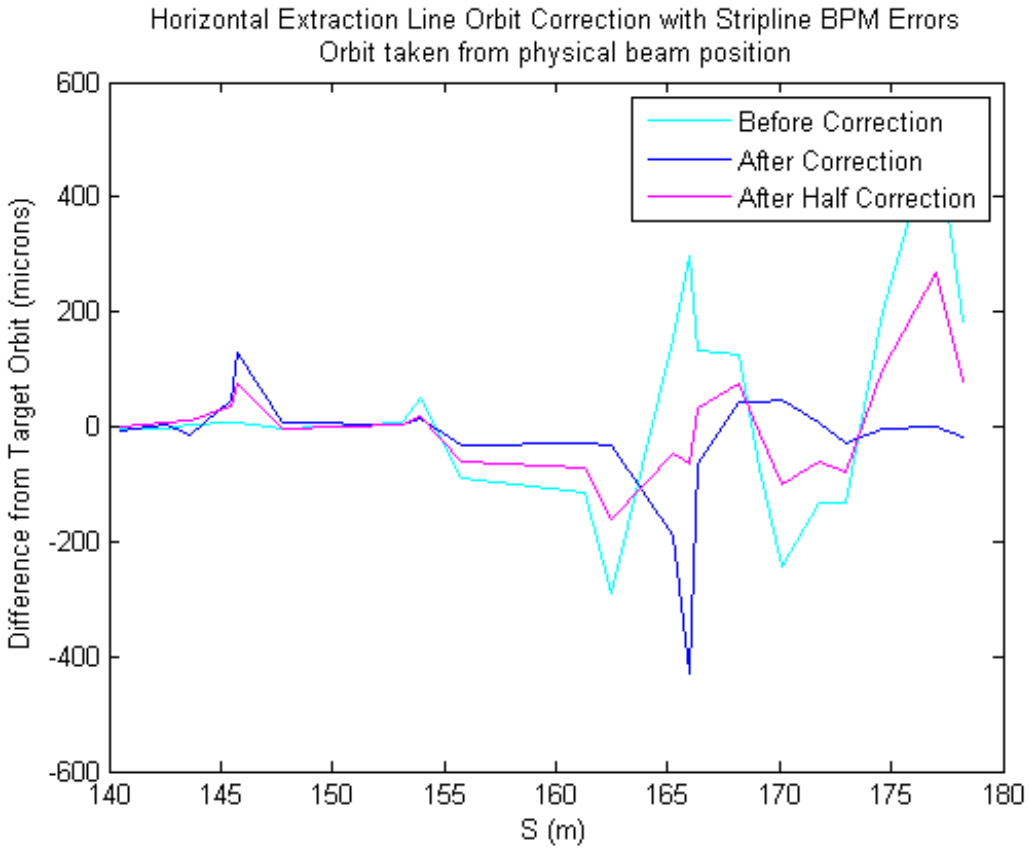

Figure 3.39: The ATF2 horizontal orbit as measured when stripline BPM reading errors have been simulated and subsequently removed before and after the application of extraction line orbit correction on the horizontal orbit. The half-correction results are also shown. The value of S starts at the beginning of ATF2.

3.5 Conclusion

A range of orbit correction algorithms have been developed and optimised for use on ATF2 and it was found that a modular global orbit correction approach was the most efficient method in all comparative tests. The optimised orbit correction method can achieve orbit reductions of 1 order of magnitude in the first iteration and can achieve orbits with micron-level orbit perturbations. The levels of dispersion along the ATF2 beam line after the orbit correction are significantly less than the starting values, which shows that the orbit correction method developed can be used to help correct other important parameters as well as the beam orbit. This should improve the chances of achieving the 37 nm vertical 'IP' beamsize goals of ATF2.

The orbit correction method developed has been favourably compared to competing orbit correction methods in simulations and on ATF2. The orbit correction method developed is on average 20 times faster than the competing methods while offering a comparable range of residual orbit perturbations. The final orbit correction software package is currently available for use on ATF2.

While developing, testing and comparing the orbit correction algorithms with other research teams the stripline BPMs were found to have an intensity dependence that was strong enough to greatly influence the orbit correction algorithms.

4

Sextupole-Based Beamsize Tuning Knobs for ATF2

4.1 Chapter Overview

The final task for ATF2 commissioning is to record a 37 nm vertical beamsize at the beamsize monitor, known as the Shintake Monitor [26], located at the IP [27], which is expected to have a resolution of 2 nm. This is achieved through the use of a set of beamsize tuning knobs. The term tuning knob is used to describe an algorithm which makes measurable changes to the parameters of the beam by changing the parameters of the accelerator components in such a way as to allow the value of the beam parameter to be optimised by varying the magnitude of the component parameter changes. A tuning knob can be thought of as analogous to the dials found on many electrical appliances. A tuning knob is created by theoretically calculating what value of a chosen beam parameter is achieved when a theoretical beam with a predetermined value of a chosen beam parameter is subjected to a predetermined set of magnet parameter changes. This results in a relationship between the chosen beam parameters and the magnet parameters, which when inverted gives a set of magnet changes needed to achieve a desired beam parameter value when the beam has a given beam parameter

value.

In the final focus section of ATF2 there are 5 sextupole magnets designed for the correction of beamsize errors arising due to chromatic and geometric aberrations. Each magnet has 4 variable parameters. These are the horizontal and vertical offset for each magnet through the use of magnet movers, the angle of rotation of each magnet with respect to the path of motion of the beam and the strength of each of the magnets. As a result there are a total of 20 variable sextupole magnet parameters within the final focus of ATF2 that can be used to alter the beamsize at the beamsize monitor. This chapter compares two competing sextupole-based beamsize correction techniques, the 'traditional' method and the novel 'rotation matrix' method.

4.2 Traditional Method

The traditional method is the method that is most commonly used in accelerators today. The optimisation of this method for use on ATF2 has been performed by the SLAC ATF2 research group [28] and is currently in use on ATF2.

The 20 variable sextupole magnet parameters are used to form a series of tuning knobs. These tuning knobs are sub-divided into three groups: linear tuning knobs, coupling knobs and second-order knobs. Each group of knobs is designed to correct for certain aberrations within the beam. The 4 major linear tuning knobs relate to the 4 most important Twiss parameters, β_x, β_y, η_x and η_y. The first three tuning knobs use the horizontal displacement of the sextupoles with each knob having a high orthogonality to the other tuning knobs. A high orthogonality means that the tuning knob has little or no effect on the other parameters that should not be changed by the tuning knob being used. The final linear tuning knob uses the vertical displacement of the sextupoles but suffers from a non-linear dependence on the other three linear knobs. Vertical displace-

ment of the sextupole magnets also causes linear coupling in the beam. As a result of these problems a genetic algorithm is used to optimise the orthogonality of the final linear tuning knob, which can result in reasonable values of orthogonality. There are also several linear coupling knobs. The 4 major linear coupling knobs are for the y'x, yx, y'x' and yx' aberrations. These tuning knobs make use of the vertical displacement of the sextupoles. These tuning knobs suffer from poor orthogonality with respect to the other linear tuning knobs due to non-linear dependencies. This is compensated for via the use of genetic algorithms. The required degree of orthogonality is achievable through the use of genetic algorithms. The final group of sextupole-based beamsize tuning knobs is designed to correct for second-order aberrations. There are 12 relevant second-order tuning knobs. Half of these tuning knobs use the rotation of the sextupoles around the path of motion of the beam while the other half of the tuning knobs use changes in the strengths of the sextupole magnets. Since there are only 5 sextupole magnets and only one variable parameter per magnet is used for the development of both groups of 6 second-order tuning knobs the problem is over-constrained. Half of the tuning knobs cannot be made orthogonal with the matrix inversion technique and the orthogonality of the other knobs is not good. As a result the knobs that are not orthogonal are not used for tuning purposes.

The traditional method was tested on a simulation of ATF2 with a full set of dynamic and static errors [20]. The simulation was run using a beam of 10,000 macroparticles and for 100 seeds of errors. In 90% of the simulations a vertical beamsize of less than 41 nm to 42 nm was achieved with 50% of the simulations resulting in beamsizes of less than 37 nm to 39 nm. When the speed of the magnet movers is taken into account 90% of the simulations took less than 30 hours to tune to within 10% of the design vertical beamsize (See Fig. 4.1) [28].

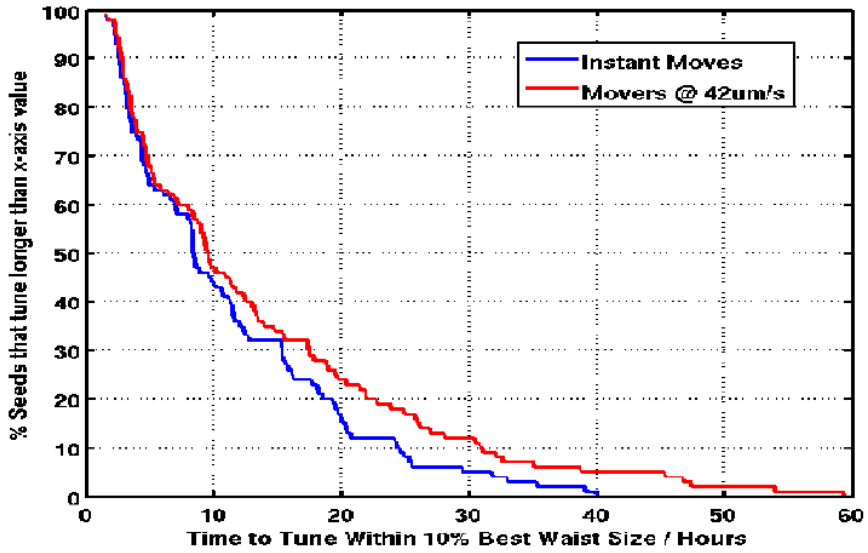

Figure 4.1: Expected beam time to perform ATF2 tuning (100 simulated seeds).

4.3 Rotation Matrix Method

A novel sextupole-based tuning knob method has been developed as part of the research presented in this report. This novel method is known as the 'rotation matrix' method and has been designed as an alternative to the traditional method of beamsize correction. The difference between these two methods is what set of beam parameters are used for the creation of the tuning knobs. The traditional method uses the Twiss parameters and the average position and angle of the particles of the beam, whereas the rotation matrix method uses the 6-dimensional coordinates of the beam. The traditional method can be thought of as simply morphing the beam with errors into the desired beam and the rotation matrix method can be thought of as compressing and rotating the beam with errors into the desired beam.

4.3.1 Theory

The rotation matrix method relies upon the use of a beam response matrix, R, which is conceptually visualised as rotating/compressing a disturbed beam, $beam_{err}$, into the

ideal beam, $beam_0$ (See Fig. 4.2).

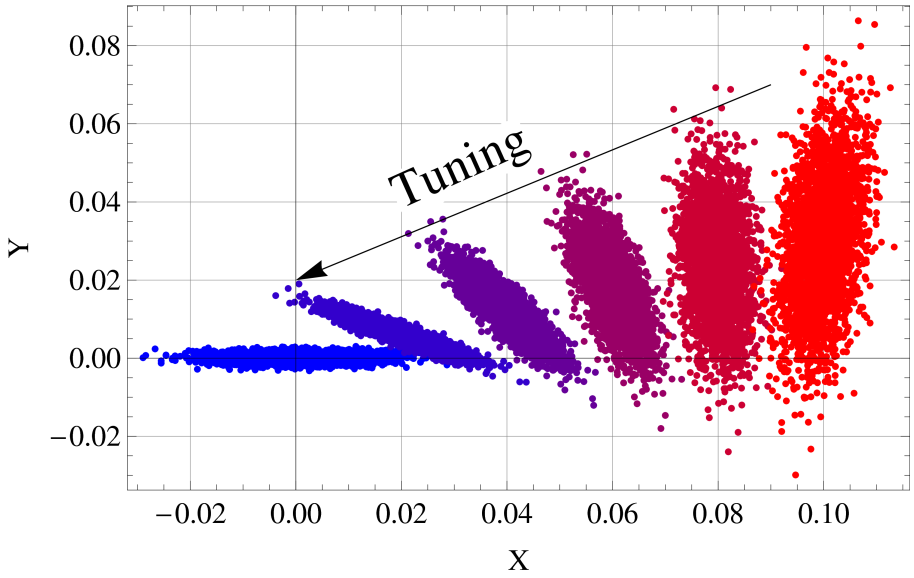

Figure 4.2: Beam response matrix tuning from the error beam (red) to the nominal beam (blue). The X and Y values are at the IP.

The response matrix is defined as

$$R = beam_0^{-1} \cdot beam_{err} - I \tag{4.1}$$

where I is the 6x6 identity matrix and $beam_0$ & $beam_{err}$ are matrices containing the 6-dimensional coordinates (x, x', y, y', l, δ) of the same initial set of particles with and without errors respectively. This results in a 6x6 R matrix. Response matrices are calculated when all 4 parameter changes for all 5 sextupoles are independently set to predetermined values when no other errors are present. This generates 20 unique response matrices, which are normalised with respect to one of the response matrices. The matrix to be used for the normalisation process was arbitrarily chosen to be the horizontal motion-based response matrix that contains the largest numerical value. Following the normalisation Singular Value Decomposition (SVD) is used to invert the combined response matrix. This results in 36 tuning knobs which contain the nor-

malised values for all available sextupole parameters.

The knobs are applied one at a time in a predetermined sequence. By repeating this process several times for all of the tuning knobs the beamsize at the beamsize monitor can theoretically be reduced to the design value. A Nelder-Mead simplex minimiser is used in order to determine the strength of the knob applied. The 'figure of merit' that is to be minimised is a combination of the horizontal and vertical beamsizes measured at the beamsize monitor. The relative weighting applied to the horizontal and vertical beamsizes in order to calculate the figure of merit is a parameter which needed to be optimised in order to increase the efficiency of the minimiser.

Due to the under-constrained nature of the rotation matrix method the orthogonality of all 36 tuning knobs is very poor. As a result a sub-set of tuning knobs was chosen and optimisation was performed on the orthogonality of the chosen tuning knobs.

4.3.2 Single Error Seed Optimisation

The rotation matrix method was optimised for one seed of static and dynamic errors. Static errors are errors that are consistent throughout the period the machine is in use, e.g. displacement or rotation of magnets and other machine components, whereas dynamic errors are continuously changing errors, e.g. initial beam parameter errors and ground motion. Other sources of errors are machine limitations, e.g. the beamsize monitor resolution and the movement limit of the magnet movers, also there is the speed of motion of the magnet movers. The optimised method for one seed of errors may not be the optimised method for all possible seeds of errors however optimising the method for multiple seeds of errors would significantly increase the CPU time required for the optimisation process.

In order to avoid the possibility of the simplex minimiser spending a long period of time attempting to find a minimum for a poorly performing tuning knob a limit of 20 iterations was set on the minimiser before the tuning knob would be assumed to have reached a minimum. This could lead to a situation where the minimum of a tuning knob is missed but will increase the overall efficiency of the CPU time of the method. The limit on the number of iterations, as well as decisions on what tuning knobs are used and how the tuning knobs are created, can also be construed as a form of errors.

Tuning Knob Optimisation

The ATF2 extraction line and final focus were simulated using DIMAD. A range of magnet misalignments [20] were applied and the orbit was corrected. Each theoretically optimal tuning knob was analytically applied to the resultant $beam_{err}$ and the change in the horizontal and vertical beamsizes were calculated by fitting a Gaussian to the beam distribution. It was determined that 5 tuning knobs had a significant effect on the horizontal beam size and 5 tuning knobs had a significant effect on the vertical beam size. The 10 chosen tuning knobs were (xx, xy, x'x, x'y, yx, yy, y'x, y'y, δx, δy). These 10 tuning knobs had very poor orthogonality to each other initially. A systematic approach was taken to improve the orthogonality of these tuning knobs. The order of magnitude of the 4 magnet parameter values used during the initial response matrix generation phase were optimised by comparing all possible combinations within a predetermined range. The magnet parameter values were fine-tuned using a simplex minimiser. The number of eigenvalues retained during the SVD process was also optimised with respect to the orthogonality of the tuning knobs. Finally the weightings applied to each of the 4 magnet parameters when applying the tuning knobs were optimised following the same routine used during the response matrix generation phase. After the optimisation was completed 2 of the tuning knobs were considered fully orthogonal with the rest of the tuning knobs showing a wide range of orthogonality levels.

Although the tuning knobs must be built using simulations the tuning knobs can be

generated with or without error contributions. As a result the tuning knobs were built with and without initial beam jitter and static errors. Since Lucretia [29] is the 'code of choice' for ATF2 software development a decision was made to switch to Lucretia at this point in the optimisation process. When initial beam jitter was simulated the resultant tuning knobs were averaged over 10 bunches. It was found after all 10 tuning knobs had been set that using the ideal lattice with the inclusion of initial beam jitter was the most efficient correction technique (see Table 4.1). This is due to the fact that the initial beam parameters have a large effect on the effects of the tuning knobs which is cancelled by using a statistically large group of initial conditions. Machine time (Time) is a summation of the time taken for each set of averaged BPM readings and the maximum time taken for mover moves during each application of a tuning knob.

Table 4.1: A comparison of the effects of error sources (static and dynamic) on the efficiency of the tuning knob generation procedure.

Static	**Dynamic**	**Vertical Beam size (nm)**
No	No	652.6
No	Yes	145.0
Yes	No	216.9
Yes	Yes	223.2

The figure of merit used by the minimiser in order to determine the strength of each tuning knob is given by $\sqrt{(\frac{\sigma_x}{\sigma_{x_0}})^2 + \alpha(\frac{\sigma_y}{\sigma_{y_0}})^2}$ where σ_x and σ_y are the horizontal and vertical beamsizes respectively, σ_{x_0} and σ_{y_0} are the design horizontal and vertical beamsizes respectively and α is the weighting factor. A range of weighting factors were tested in Lucretia using the same error seed (Fig. 4.3). A resolution of 2 nm was applied to the beamsize readings. A 10,000 particle beam was used during simulations which results in beamsize jitter of the order of 1 nm. For all weighting factors the first tuning knob decreases the beam size by about 90% before the resolution of the beamsize monitor and the beamsize jitter begin to dominate the effects of the tuning knobs. In order to correct the horizontal beamsize while never allowing it to dominate

the figure of merit a weighting factor of 500 was chosen for future simulations.

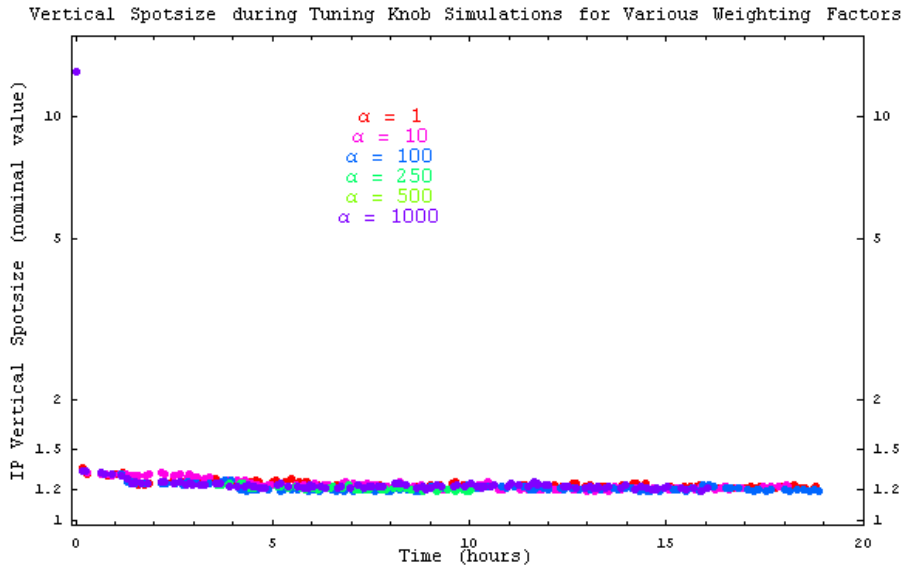

Figure 4.3: The vertical spotsize of ATF2 as a function of machine time during tuning knob simulations using a range of weighting factors.

Simulation Results

The tuning knobs were tested in the presence of individual errors on the final sextupole (SD0FF) and final quadrupole (QD0FF). No beam jitter was included and the beamsize monitor was assumed to have perfect measuring ability.

A sextupole strength error of $\frac{\Delta B}{B} = 10^{-2}$ was applied to SD0FF. The orthogonally optimised tuning knobs were tested along with a range of other scenarios (Fig. 4.4). The tested scenarios were:

- tuning knobs without orthogonality optimisation;
- tuning knobs generated with a reduced contribution from roll effects;
- tuning knobs generated with a stronger contribution from sextupole strength effects.

The tuning knobs that had reduced orthogonality had larger starting tuning knob strengths than the orthogonally optimised tuning knobs which resulted in each tuning knob taking more machine time to optimise its strength. An increased contribution from sextupole strength effects quickly compensates for the original error and reaches the design vertical beamsize in roughly 1 hour. The orthogonally optimum tuning knobs quickly reach a state where any application of the tuning knobs creates beamsize growth effects.

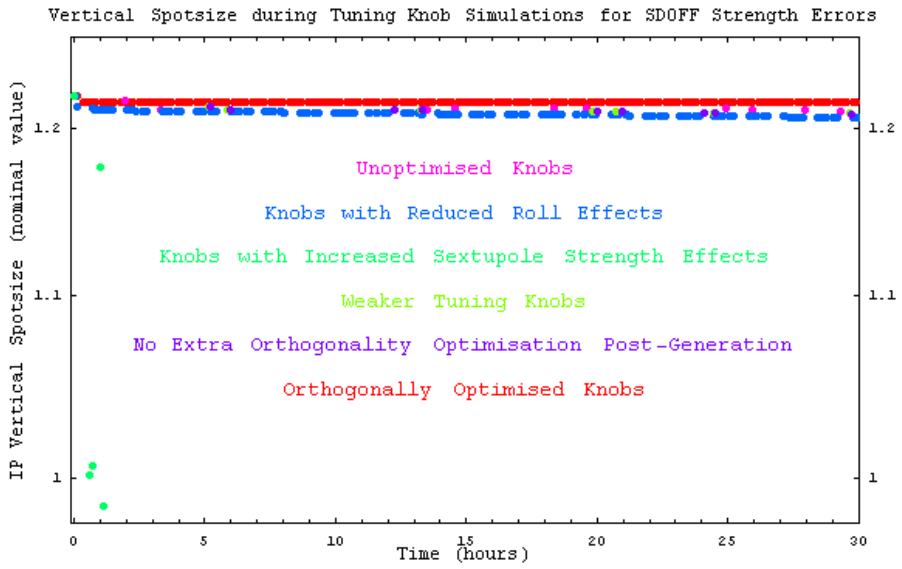

Figure 4.4: The vertical spotsize of ATF2 as a function of machine time during tuning knob simulations when a sextupole strength error is applied to SD0FF.

A quadrupole strength error of $\frac{\Delta B}{B} = 10^{-3}$ was applied to QD0FF. The orthogonally optimised tuning knobs were tested along with the most successful scenario from the previous test and a set of unoptimised tuning knobs (Fig. 4.5). As with the previous test an increased contribution from sextupole strength effects quickly compensated for the original error. The orthogonally optimum tuning knobs quickly reach a state where any application of the tuning knobs creates beamsize growth effects which indicates that the orthogonality of the optimised tuning knobs is not ideal. The unoptimised tuning knobs slowly correct for the original error due to coincidence rather than design.

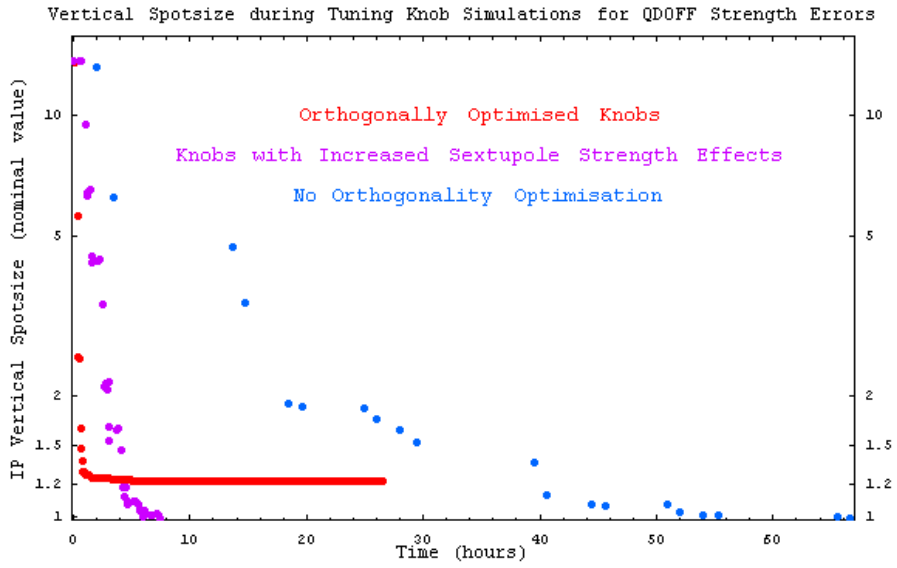

Figure 4.5: The vertical spotsize of ATF2 as a function of machine time during tuning knob simulations when a quadrupole strength error is applied to QD0FF.

A quadrupole roll error of 1 mrad was applied to QD0FF. The orthogonally optimised tuning knobs were tested along with the scenarios from the previous test (Fig. 4.6). An increased contribution from sextupole strength effects results in a decrease in the vertical beamsize followed by an increase in the vertical beamsize. This is likely due to a strong inverse coupling between the horizontal and vertical beamsizes. As the vertical beamsize decreases, the horizontal beamsize increases until the horizontal beamsize dominates the figure of merit, at which point the process is reversed. The orthogonally optimum tuning knobs slowly decrease the vertical beamsize, however after 24 hours of machine time the vertical beamsize is still around 10 times larger than the design value. The unoptimised tuning knobs slowly decrease the beamsize down to twice the nominal value within 3 days of machine time.

A full range of static and dynamic errors were applied to a simulation of ATF2. The same scenarios used in the previous tests were used along with a special case (Fig. 4.7). If the beamsize did not decrease by 2 nm over a full set of 10 tuning knobs,

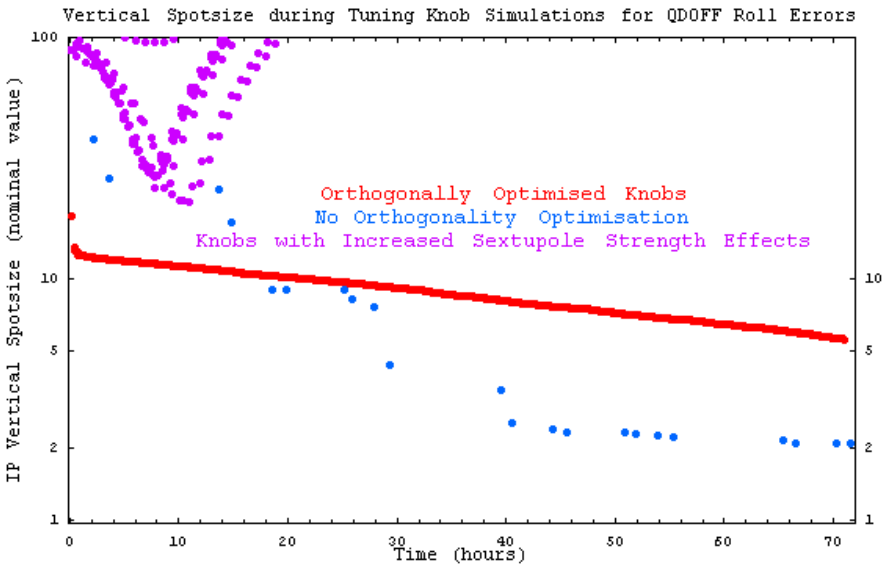

Figure 4.6: The vertical spotsize of ATF2 as a function of machine time during tuning knob simulations when a 1 mrad roll error is applied to QD0FF.

the tuning knobs would be re-generated using the current simulated beamline complete with errors. This should indicate if the machine has changed so much as to make the tuning knobs no longer applicable. The results indicate that the tuning knobs are always applicable and that the lack of change in the vertical beamsize is due to the beamsize monitor resolution and the beamsize jitter, caused by dynamic errors. The unoptimised tuning knobs fail to converge quickly, as such they are not suitable for use on the real machine. Results from the use of tuning knobs with increased sextupole strength effects show no improvement over the orthogonally optimised tuning knobs. These results indicate that the orthogonally optimised tuning knobs are the most efficient rotation matrix method tuning knobs for use on ATF2.

For this one seed the optimised rotation matrix method tunes to within 20% of the design vertical beamsize and completes the tuning process in less than 3 hours.

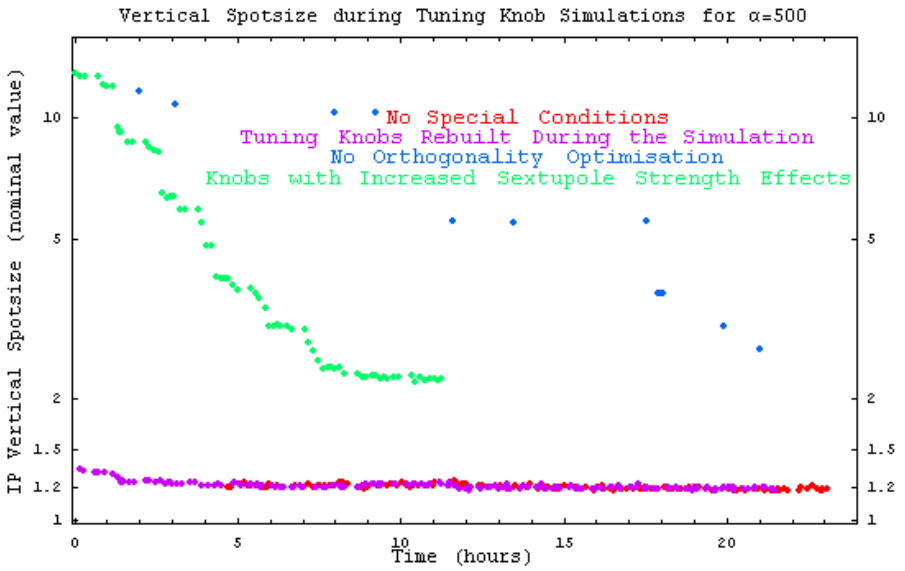

Figure 4.7: The vertical spotsize of ATF2 as a function of machine time during tuning knob simulations when a weighting factor of 500 is used.

4.3.3 Multiple Error Seeds Optimisation

The findings were taken from the single error seed optimisation and were tested for multiple error seeds so that an optimised version of the rotation matrix method could be applied to a set of 50 error seeds. This number of seeds was chosen due to CPU time limitations.

The choices that were tested were the use of 10 tuning knobs instead of all 36 tuning knobs, the limiting of the number of iterations of the simplex minimiser that can be used per tuning knob, the use of a weighting factor of 500, the use of the orthogonally optimised tuning knobs and the use of the ideal lattice when forming the tuning knobs.

Table 4.2 indicates that the use of only the 10 best tuning knobs results in a smaller beamsize than using all 36 tuning knobs.

Table 4.3 indicates that the optimisation method performs better when the number of minimiser iterations is limited, however these results used a limit of 20 iterations

Table 4.2: A comparison of the final vertical beamsizes for two error seeds when the 10 best tuning knobs are used and all 36 tuning knobs are used.

Seed Number	Number of Tuning Knobs	Vertical Beamsize (nm)
1	10	44.6
1	36	290
2	10	141
2	36	155

Table 4.3: A comparison of the final vertical beamsizes for three error seeds when the number of iterations of the minimiser is either limited or unlimited.

Seed Number	Limited Iterations	Vertical Beamsize (nm)
1	Yes	78.2
1	No	215
2	Yes	309
2	No	516
3	Yes	138
3	No	143

which would consistently cause the minimiser to finish before the tuning knob strength could converge on a minimum. As a result the final limit was increased to 40 to allow for a greater chance of the minimiser reaching a minimum while also keeping the CPU time to a minimum.

Table 4.4 indicates that the optimal weighting factor for use in the minimiser is in the region of 250. As a result a weighting factor of 250 was chosen for the optimised beamsize tuning method.

Table 4.5 clearly indicates that using orthogonal tuning knobs results in the optimal beamsize tuning method.

Table 4.6 does not give a consistent or clear indication of whether tuning knobs built from the ideal lattice or from a lattice with real errors will result in a more optimal beamsize tuning method. Since only one of the results had a beamsize that was

Table 4.4: A comparison of the final vertical beamsizes for 2 error seeds when the weighting factor used during the minimiser is altered.

Seed Number	Weighting Factor	Vertical Beamsize (nm)
1	1	44.4
1	10	44.4
1	100	43.6
1	250	44.2
1	500	44.2
1	1000	44.2
2	1	135
2	10	131
2	100	136
2	250	44
2	500	138
2	1000	133

Table 4.5: A comparison of the final vertical beamsizes for 2 error seeds when the tuning knobs used are orthogonal and when not orthogonal.

Seed Number	Orthogonality	Vertical Beamsize (nm)
1	Yes	44.2
1	No	246582
2	Yes	138
2	No	21742.5

Table 4.6: A comparison of the final vertical beamsizes for 5 error seeds when the tuning knobs are built using the ideal lattice and using the lattice with real errors.

Seed Number	Lattice Type	Vertical Beamsize (nm)
1	Ideal	40.4
1	Real	38.4
2	Ideal	126
2	Real	159
3	Ideal	104
3	Real	147
4	Ideal	230
4	Real	324
5	Ideal	55
5	Real	65.4

close to the design vertical beamsize, which used tuning knobs built from a lattice with real errors, this situation was chosen for the optimised beamsize tuning method.

The settings chosen for the optimised beamsize tuning method were: the use of the best 10 tuning knobs; the minimiser limited to 40 iterations per tuning knob; the weighting factor set to 250; the tuning knobs built using a lattice with real errors and made as orthogonal as possible.

4.3.4 Full Error Testing

The optimised rotation matrix method was intended to be tested on a full range of static and dynamic errors using the same 100 seeds as used for the testing of the traditional method. The test was to be conducted using the 10 best tuning knobs scenario and the all 36 tuning knobs scenario. A limit of up to 3 days of simulated machine time would be placed on each tuning attempt. Only a subset of the 36 tuning knob scenario seeds were eventually tested, with some not being allowed to run for the full 3 days of simulated machine time. Only one seed could be tested for the 10 best tuning knobs scenario. The results from these tests were collected (Fig. 4.8). The vertical beamsize at multiple times during the test of the 10 best tuning knobs scenario is also presented.

The final vertical beamsize results from the 36 tuning knobs and the 10 best tuning knobs results were added together with all the relevant results from Tables 4.2 - 4.6. This gives a thorough view of the range of the potential vertical beamsizes achievable by the rotation matrix method if it is applied to ATF2 when a full range of errors is present (Fig. 4.9). The results show that the rotation matrix method can achieve a vertical IP beamsize of 5 sigma or less a third of the time, and 8 sigma or less half of the time. It can also be seen that 10% of results are 2 sigma or less and 10% are 15 sigma and higher. The highest result was 27.9 sigma and the lowest was 1.04 sigma. These

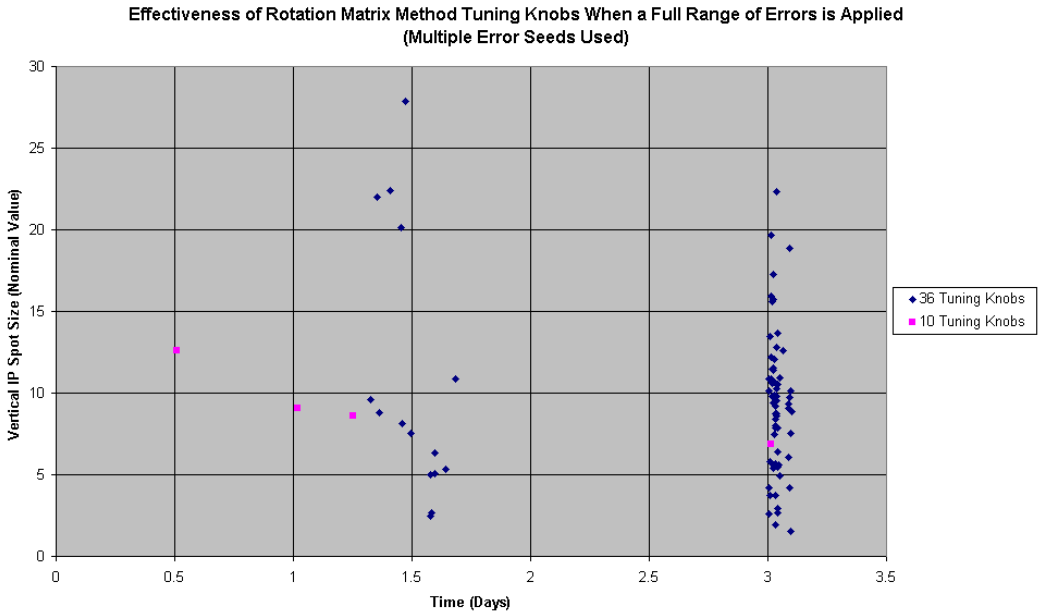

Figure 4.8: The vertical IP beamsize results from tests of the rotation matrix method in the presence of a full range of errors.

results suggest that the effectiveness of the rotation matrix method is highly dependant on the errors within the machine.

4.4 Conclusion

The traditional method has been shown in simulations to be capable of tuning to within 10% to 14% of the design vertical beamsize (40.7 nm to 42.2 nm) whereas the rotation matrix method is highly error dependent and unreliable at the time of writing. As a result the rotation matrix method cannot be used as an alternative to the traditional method on ATF2 at the moment.

The unreliability of the rotation matrix method is believed to be due to it only working well when the region of the lattice it is applied to is mostly linear, hence this work shows that ATF2 is too non-linear for the method to work in most situations tested.

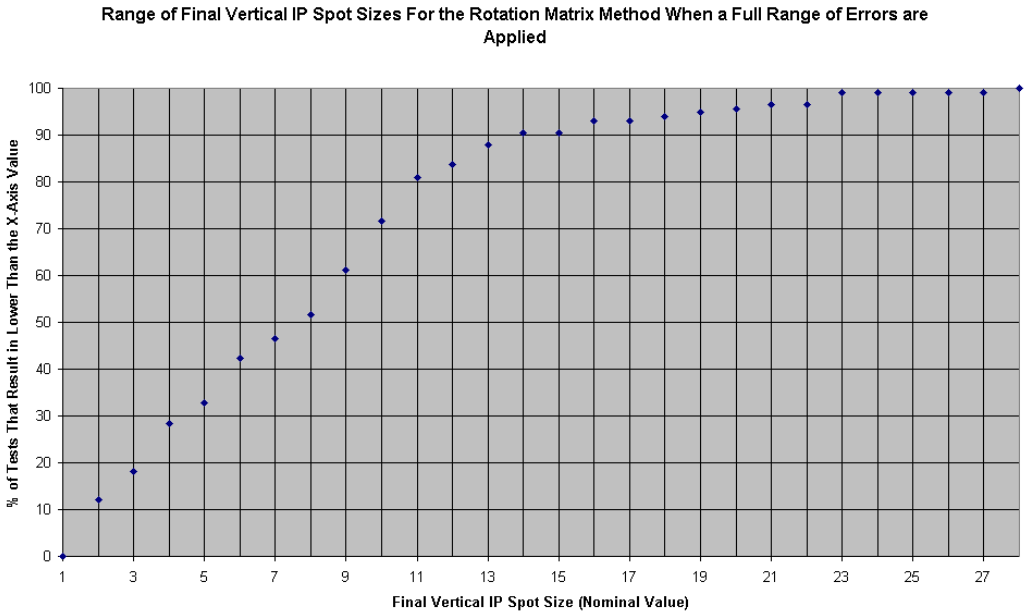

Figure 4.9: The range of final vertical IP beamsizes when the rotation matrix method is applied to a full range of errors.

These problems were believed to have been compensated for in the optimisation of the method, however this could be a fundamental limitation in the method that may not be correctable or a problem unique to the ATF2 design. Also the poor orthogonality issues that were believed to have been corrected in the optimisation process may still persist and be another fundamental limitation of the method or ATF2. This would mean that the method is only usable in some linear, highly orthogonal situations, one or more of which may have been chanced upon during the orthogonality process, thereby giving the positive results from the optimisation process. As has been previously stated, the traditional method also had linearity and optimisation problems, however this method has had more research and development to reduce the limitations caused by these problems, which suggests that more research may reduce the limitations of the rotation matrix method with regards to its use on ATF2.

At present, the traditional method is already available for use on ATF2 while the rotation matrix method has yet to be implemented on ATF2. As a result, the commission-

ing of ATF2 is presently using the traditional method. Due to the current limitations of the rotation matrix method and ATF2, the rotation matrix cannot be successfully used as an independent method for beamsize reduction at ATF2.

5

Conclusion

5.1 Chapter Overview

The Accelerator Test Facility (ATF) in KEK, Japan was a low emittance, electron-based, damping ring and extraction region. It was upgraded to ATF2 when the extraction line was redesigned and a final focus section was added. The primary goal of ATF2 was to achieve and maintain a 37 nm vertical IP beamsize. The work presented was intended to help achieve this goal. Three major problems were chosen for investigation: elimination of a source of unwanted emittance grown in the extraction region of ATF; optimisation of the orbit correction procedures in ATF2 and optimisation of the vertical beamsize tuning in the ATF2 final focus region. It was believed that failure to find a solution to any one of these 3 problems would lead to an inability to achieve the primary goal of ATF2.

5.2 Emittance Growth Studies at ATF

5.2.1 Overview

The following is a quote from the ATF2 proposal vol. 1 [7] which details the main reason for the beam studies at ATF:

> The observed intensity dependence of the vertical emittance is also much stronger in the extraction line than in the damping ring. This dependence is also larger than the intensity dependence of the longitudinal and horizontal emittances. This strong intensity dependence cannot be explained by linear coupling between the vertical and either of the other two axes. We suspect that unknown nonlinear fields in the extraction kicker and the septum magnets cause higher-order x-y and/or energy-y coupling. The normalised vertical emittance (at $N = 5\times10^9$) is about 48 nm, which is larger than in the damping ring (about 15 nm) by a factor of three, while the nominal ATF2 goal emittance is 30 nm. If the vertical emittance cannot be reduced to the nominal value, it would make the vertical beam spot size larger than nominal size by about 30%, for an intensity of 5×10^9. For 2×10^{10} the blow up would be even larger.

The possible source chosen was the non-linear fields in the damping ring quadrupoles that are situated between the extraction kicker magnet and the extraction septa magnets (QM6R and QM7R). An international team of physicists was formed to study the magnets in the extraction region and identify the reason for the emittance growth.

5.2.2 Summary of Results

The quadrupoles and septum magnets were modelled using a finite element code and the multipole coefficients were measured [10]. When the beam is extracted through QM7R it is of the order of 2.25 cm off-centre in the horizontal direction and has a non-negligible sextupole component for the extracted beam, which is strongly dependent on the horizontal and vertical position of the extracted beam. The emittance growth from the multipole fields was also estimated using particle tracking codes [12] and shows a dependency between the emittance growth and the vertical position of the beam in QM7R. This suggested that QM7R was the main reason for the emittance growth.

This theory was tested by creating vertical bumps in the beam position through QM7R using both simulations and real world tests and measuring the vertical emittance after QM7R. The multipoles of QM7R could not fully explain the emittance growth effects seen at ATF, however further extended simulation work using the multipoles of QM7R and the extraction septum magnets managed to find a good agreement between the simulations and the measurements taken at ATF.

5.2.3 Conclusion

The conclusion that QM7R was the major cause of the emittance growth led to the replacement of QM7R with a bigger bore magnet called 'TOKIN 3581'. Using a bigger bore magnet will mean that the non-linear fields at the same location will be smaller.

5.3 Orbit Correction Optimisation for ATF2

5.3.1 Overview

Orbit correction is an important part of the operation of an accelerator. The machine was designed with magnets and instruments where the beam passes through the exact centre of all the components unless the path of the beam is being altered. When the beam passes off-centre through the magnets it is affected by the magnets' multipole fields. These fields cause alterations to the path of the beam and the parameters of the beam, including beamsize growth. Orbit correction techniques for the ATF2 extraction line and final focus were developed during the course of these studies and compared in simulations and real world tests with alternative techniques.

5.3.2 Summary of Results

Of the several methods of orbit correction that were investigated for use on ATF2 a method known as 'modular global orbit correction' was found to give the best results in simulation tests. The modular global orbit correction method treats the extraction and final focus regions as separate sections and corrects the orbit of each one in turn. This method was adapted into a working orbit correction program for use on ATF2.

The modular global orbit correction method was tested and compared in simulations and real world tests with a method developed by another team. The modular global orbit correction method was shown to be significantly faster than the alternative method while offering comparatively similar results. Both methods were shown to suffer from 50 - 100% over-correction in the final focus section. This was found to be a result of an intensity dependence with the stripline BPMs. At the time of writing neither method was shown to fully correct the orbit of ATF2 in real world tests.

5.3.3 Conclusion

The modular global orbit correction method that was optimised as part of this report has joined the selection of orbit correction software packages available on ATF2 and can be used on the machine for orbit correction if needed. It has also been shown to be comparatively better than other competing orbit correction methods.

5.4 Sextupole-Based Beamsize Tuning Knobs for ATF2

5.4.1 Overview

Since the goal of ATF2 is to maintain an ultra-low vertical beamsize of 37 nm, the most important tool for ATF2 is a reliable, versatile and preferably quick beamsize tuning method. The traditional method of beamsize tuning has been optimised for

use on ATF2 by a team from SLAC and is in use on ATF2, however a novel method of beamsize tuning known as the rotation matrix method has been invented and suggested for use on ATF2. The rotation matrix method was researched, optimised and tested for use on ATF2 as part of the work presented with the aim to see if it could replace or work with the traditional method currently in use on ATF2.

5.4.2 Summary of Results

The rotation matrix method was optimised for ATF2 using single error simulations as well as simulations that made use of a full range of errors. In several of these tests, a vertical beamsize between 1 and 2 times the 37 nm goal could be achieved. During tests intended to compare the rotation matrix method with the traditional method it was impossible to achieve consistent beamsizes and the range in vertical beamsizes was between 1 and 28 times the 37 nm goal. The traditional method has previously been shown to achieve vertical beamsizes between 1.1 and 1.4 times the 37 nm goal in 90% of cases.

5.4.3 Conclusion

Not all options available for the rotation matrix method were completely explored and no real world tests could be performed due to unforeseen consequences, hence while the rotation matrix method cannot be shown to be a viable alternative to the traditional method it cannot be fully ruled out as a viable method for use in future studies.

5.5 Final Conclusion

The work presented helped identify the QM7R's non-linear fields due to the small bore radius as the main contributor to the extraction region emittance growth that plagued ATF and would potentially have made the 37 nm vertical beamsize of ATF2 impossible to achieve. As a result the larger bore radius TOKIN 3581 magnet has replaced the

QM7R magnet.

An orbit correction software package based on the modular global method has been created for ATF2 and can be used for orbit correction. It has been shown to be significantly faster, while offering similar results, to the alternative methods available at ATF2.

The novel rotation matrix method of beamsize tuning could not be proven a viable alternative to the traditional method currently in use on ATF2.

At the time of writing a vertical beamsize of about 300 nm has been achieved on two separate occasions at ATF2 using the traditional method of beamsize tuning [30].

Appendices

Appendix A

Accelerator Physics Software

A number of computer software tools exist to assist in the development and operation of accelerators. These range from simple codes intended as a tool for solving beam dynamics equations to codes that attempt to accurately simulate the activities of specific accelerators.

The work performed in this report was intended to build upon the tuning and alignment work performed by J. K. Jones (ASTeC) [31]. The code used in previous tuning work was MAD 8.23DL, a Daresbury Laboratory and ASTeC version of the MAD code developed by CERN as a way of simulating the passage of particles along a beamline. MAD has the ability to simulate any device that can affect the dynamics of the beam. This allows for the whole of the ILC BDS or ATF2 final focus to be simulated and have a bunch of charged particles tracked along the full length of the beamline. The code also allows for the simulation of magnet misalignments and strength errors [32].

A sample MAD bump generating subroutine is included, where 4 vertical correctors (ZV8R, ZV9R, ZV10R and ZV11R) are used to create a closed bump of a desired value at QM7R.1:

```
MRBUMP : SUBROUTINE
    SET, ZV8R[KICK],   1.E-6
    SET, ZV9R[KICK],   1.E-6
    SET, ZV10R[KICK],  1.E-6
    SET, ZV11R[KICK],  1.E-6
    USE, ATFDRx
    CELL, ORBIT
      VARY, ZV8R[KICK],   STEP=1.E-5
      VARY, ZV9R[KICK],   STEP=1.E-5
      VARY, ZV10R[KICK],  STEP=1.E-5
      VARY, ZV11R[KICK],  STEP=1.E-5
      CONSTR, "QM7R.1"[1], Y=bump(m)
      CONSTR, "QM7R.1"[1], PY=0
```

MAD suffers from some limitations that were considered significant for the tuning and alignment project. These limitations required the use of an alternative code. The code chosen as the replacement is called DIMAD [33]. DIMAD is a code developed at SLAC that is very similar to MAD in the format of the code yet overcomes many of the relevant limitations of MAD. DIMAD also allows for the inclusion of an 'aperture' value for all the beamline elements which tracks when a particle strays outside the confines of the beampipe and is lost. Furthermore DIMAD simulates the effects of synchrotron radiation on the beam, which adds to the 'real world' compatibility of the code.

A comparison of the two codes is made for a simple F0D0 cell beamline when a misalignment is placed on the focusing quadrupole (QF1):

MAD

```
D1: DRIFT, L=10, Type=D1;
QF1: QUADRUPOLE, L=2, K1=0.01
QD1: QUADRUPOLE, L=2, K1=-0.01
Ring: Line=(QF1, D1, QD1, D1);
Use, Ring;
INITIAL:BETA0,BETX=50,&
ALFX=-2,BETY=9,ALFY=0.5;
SELECT,FLAG=ERROR,RANGE=QF1;
EALIGN,DX=10e-6;
EFIELD,DKL(1)=0.005
track,onepass;
start,x=0.0000510405,px=0.00000274034,&
y=0.0000000674732,&
py=0.000000115889,deltap=0.000365737;
Run,Table=ttrack,method=transport,Turns=1;
Archive,table=ttrack,filename=trackht.dat;
endtrack;
```

DIMAD

```
D1: DRIFT, L=10, Type=D1;
QF1: QUADRUPOLE, L=2, K1=0.01,& APERTURE=10e-3;
QD1: QUADRUPOLE, L=2, K1=-0.01,& APERTURE=10e-3;
Ring: Line=(QF1, D1, QD1, D1);
Use, Ring;
SELECT,FLAG=ERROR,RANGE=QF1;
EALIGN,DX=10e-6;
DIMAT
```

```
ERRORS DATA
QF1 K1 0.005;
99,
SET ERRORS
0 1 QF1,
BEAM matrix tracking
0 50 -2 0.0 0.0 1.96e-11
9 0.5 0.0 0.0 8.18e-14
0.0003 0.001 -1,
SEED
42,
GENERATION OF PARTICLES
3 5 5 5 5 5 5 1 1 0 0 0 0 0 0,
TRACKING OF PARTICLES
-1 -1 0 1 0 3,
PARTICLE DISTRIBUTION TRACKING
3;
```

The tuning and alignment work performed prior to the start of this project used the MADInput [34] package developed by J. K. Jones, which is a code that allows the mathematics software called Mathematica [17] to generate and run MAD codes. MADInput offers an easier and more convenient way of developing, testing and implementing the tuning and alignment techniques investigated in this project, as such a DIMAD compatible version called DIMADInput was developed for this project.

A comparison between the tracking results generated using the MADInput and DIMADInput packages when a 1 micron horizontal misalignment was applied to the quadrupole QD6 in the ILC BDS revealed no significant differences between the codes (Fig. A.1).

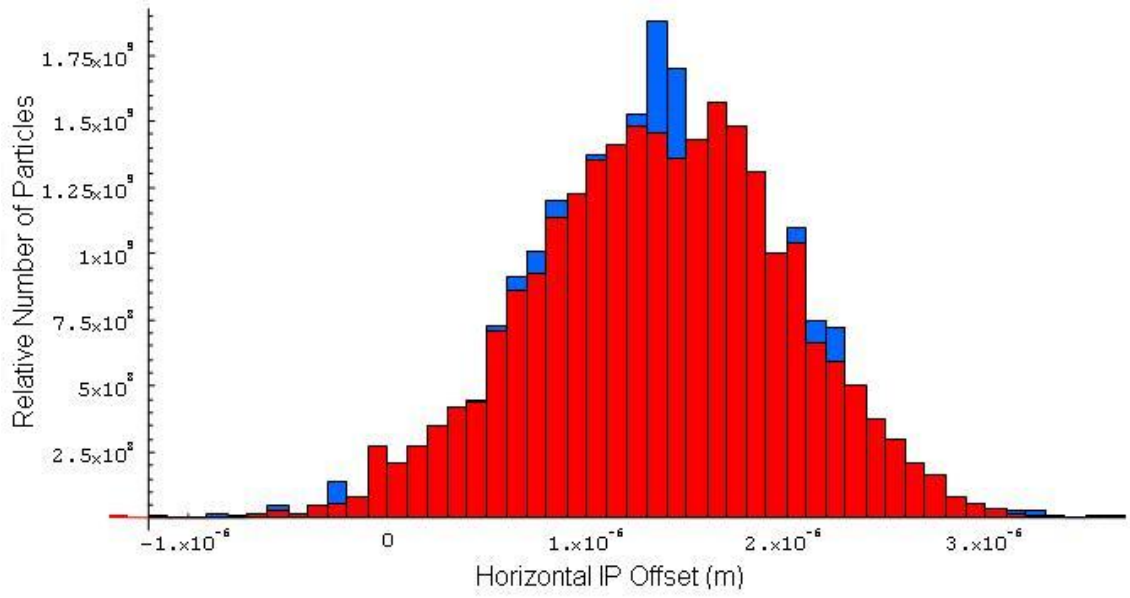

Figure A.1: A histogram showing the horizontal positions of the particles in the bunch when compared to the position of the reference particle at the end of the ILC BDS when a one micron horizontal misalignment is applied to QD6. The MADInput results are in blue and the DIMADInput results are in red.

Appendix B

Nelder-Mead Simplex Minimiser

One of the mathematical techniques used regularly during the work presented in this report is called the Nelder-Mead simplex minimiser method. The term simplex refers to a generalised triangle in n-dimensional space. By sequentially replacing the highest valued vertex with a newly generated lower valued vertex it is possible to reduce the area of, and reposition, the simplex so that it comes to rest at a minimum within the n-dimensional space. The minimum at which the simplex comes to rest may not be the global minimum and may not be the minimum that is closest to the initial starting position of the simplex.

If the function to be minimised is defined as $f(x_1, x_2, ..., x_n)$ and the 3 vertices of the simplex are ordered so that $\mathbf{B} = f(x_{1b}, x_{2b}, ..., x_{nb}) \leq \mathbf{G} = f(x_{1g}, x_{2g}, ..., x_{ng}) < \mathbf{W} = f(x_{1w}, x_{2w}, ..., x_{nw})$ then the worst vertex, **W**, will be replaced with a new vertex. First the midpoint, **M**, between the points **B** and **G** is found:

$$\mathbf{M} = \frac{1}{2}(\mathbf{B} + \mathbf{G}) = \left(\frac{f(x_{1b}, x_{2b}, ..., x_{nb})}{2}, \frac{f(x_{1g}, x_{2g}, ..., x_{ng})}{2} \right) \tag{B.1}$$

Now a test point, **R**, is found that reflects from the worst point through the mid-point:

$$\mathbf{R} = \mathbf{M} + (\mathbf{M} - \mathbf{W}) = 2\,\mathbf{M} - \mathbf{W} \tag{B.2}$$

If $\mathbf{R} < \mathbf{W}$ then the simplex is approaching a minimum and the point **R** replaces the point **W**, however the minimum may be at a point that extends beyond the reflected point. Another test point, **E**, is found that is double the distance from point **M** as **R** is from point **M**:

$$\mathbf{E} = \mathbf{R} + (\mathbf{R} - \mathbf{M}) = 2\,\mathbf{R} - \mathbf{M} \tag{B.3}$$

If $\mathbf{E} < \mathbf{R}$ then the point **E** replaces the point **W**, however if $\mathbf{R} \geq \mathbf{W}$ an alternative replacement point must be found. The midpoints, $\mathbf{C_1}$ and $\mathbf{C_2}$, between the two points **W** and **M** and the two points **M** and **R**, respectively, are found. The smaller of the two midpoints is then redefined as **C**. If $\mathbf{C} < \mathbf{W}$ then the point **C** replaces the point **W**, however if $\mathbf{C} \geq \mathbf{W}$ then the points **W** and **G** must be 'shrunk' towards the point **B**. The point **M** replaces the point **G** and the midpoint, **S**, between the points **B** and **W** replaces the point **W**.

Finally the points **B**, **G** and **W** are reorganised by their respective values and the minimisation of the simplex is repeated until a reasonably low level of difference between the values of the three points is achieved, at which point the simplex is considered minimised and the coordinates, $(x_{1b}, x_{2b}, ..., x_{nb})$, of the point **B** are taken as the optimum coordinates for the current local minimum value for the function that was minimised.

List of Figures

List of Tables

References

[1] Introduction to CLIC, R. Corsini, ICAP'06, October, 2006

[2] ILC Reference Design Report, http://www.linearcollider.org/about/Publications/Reference-Design-Report, 2007

[3] , Introduction of ATF, http://www-atf.kek.jp/atf/introduction.html

[4] The Physics of Particle Accelerators an introduction, K. Wille, Oxford University Press, ISBN 0-19-850549-3

[5] Evaluation of TOKIN 3581 quadrupole as proposed replacement for QM7, P. Bambade et al., ATF2 weekly meeting, KEK, December, 2008

[6] Non-destructive emittance measurement of a beam transport line, K. EBIHARA et al, Nuclear instuments and methods, No. 202, p. 403-409, 1982

[7] ATF2 Proposal vol. 1, ATF2 group, KEK Report 2005-2, August, 2005

[8] Proposed replacement of QM7 by TOKIN 3581, P. Bambade et al., 7th ATF2 Project Meeting, KEK, December, 2008

[9] Introduction to Transverse Beam Optics, B. Holzer, Introduction to Accelerator Physics, CERN accelerator school, October, 2006

[10] Polynomial fits for the magnets BHEX1 and QM7, F. Touze & G. Le Meur, LAL, April, 2008

[11] Extraction bumps and emittance studies for the ATF using pulsed magnets, R. Appleby, ATF2 meeting, LAPP, October, 2007

[12] Study of abnormal vertical emittance growth in ATF extraction line, M. Alabau Pons & A. Scarfe et al., MOPP003, EPAC'08, June, 2008

[13] Measurement and control of charged particle beams, M. G. Minty & F. Zimmermann, Springer, 2003

[14] The ATF control system, R. B. Appleby & M. Woodley, ATF report, ATF0802, May, 2008

[15] PRIAM/ANTIGONE : a 2D/3D Package for Accelerator Design, G. Le Meur & F. Touze, Proceedings of EPAC'94, June - July, 1994.

[16] Alignment Results of Magnets in the ATF2 Beam Line, R. Sugahara, 8th ATF2 Project Meeting, KEK, June, 2009

[17] *Mathematica*^{TM}, Wolfram Research Inc., p. 454, 1988

[18] *MATLAB*^{TM} User's Guide, The Mathsworks Inc., p. 3-178, 1990

[19] Closed Orbit Correction Using Singular Value Decomposition of the Response Matrix, Y. Chung et al, PAC'93, p. 2263, May, 1993

[20] "Beam-based alignment, tuning and beam dynamics studies for the atf2 extraction line and final focus system", G. White et al, MOPP039, EPAC08, 2008

[21] ATF2 Layout v3.8, M. Woodley et al, http://www.slac.stanford.edu/mdw/ATF2/v3.8/

[22] "Orbit reconstruction, correction, stabilization and monitoring in the ATF2 Extraction line", Y. Renier et al, FR5PFP004, PAC09, 2009

[23] Steering in the ATF2 Extraction Line, Y. Renier et al, 8th ATF2 Project Meeting, KEK, June, 2009

[24] Stripline BPM status, Y. Renier et al, 8th ATF2 Project Meeting, KEK, June, 2009

[25] A Flight Simulator for ATF2 - A Mechanism for International Collaboration in the Writing and Deployment of Online Beam Dynamics Algorithms, G. White et al, TUPP016, EPAC08, 2008

[26] Shintake Monitor in ATF2 : Present Status, T. Yamanaka, LCWS, 2010

[27] Status of the First Commissioning of the Shintake Monitor for ATF2, T. Yamanaka et al, TH6REP062, PAC'09, May, 2009

[28] Plans and Progress towards Tuning the ATF2 Final Focus System to Obtain a 35nm IP Waist , G. White & A. Scarfe et al, FR5PFP021, PAC'09, May, 2009

[29] Lucretia: A Matlab-Based Toolbox for the Modellingand Simulation of Single-Pass Electron Beam Transport Systems, P. Tenenbaum, SLAC-PUB-11215, May, 2005

[30] ATF2 SUMMARY AND STATUS, G. White & A. Scarfe et al., Beam Dynamics Newsletter, No. 54, 2011

[31] Tuning Algorithms for the ILC Beam Delivery System, J. K. Jones, EPAC'06, 2006

[32] MAD 8.21 Reference Manual, H. Grote & F. C. Iselin, http://hansg.web.cern.ch/hansg/mad/mad8/user/mad.html, 1997

[33] Users Guide to the Program DIMAD, P. G. Tenenbaum et al, http://www-project.slac.stanford.edu/lc/local/accelphysics/dimad.pdf, 2001

[34] Mathematica Interface to MAD, J. K. Jones & H. L.Owen, DPG-XX-rpt-008, 2002